Dissertation

Titel der Dissertation

Numerical Modelling of Pulsation and Convection in Cepheids

Verfasser

Mag. rer. nat. Eva Mundprecht

angestrebter akademischer Grad

Doktor der Naturwissenschaften (Dr.rer.nat.)

Wien, im Jänner 2011

Studienkennzahl lt. Studienblatt:	A 091 405
Studienrichtung lt. Studienblatt:	Mathematik
Betreuer:	Univ. Prof. Dr. Herbert J. Muthsam

Abstract

In order to simulate the pulsation convection coupling in a Cepheid the ANTARES-code was equipped with a polar and moving grid. The numerical cost of a fully parallelized, sufficiently large, and fully resolved section would be immense. Thus it was not only necessary to find a suitable model, but also save to costs for parallelisation and grid refinement.

The equations governing the hydrodynamics were derived for this particular grid and implemented in the code. The grey short characteristics method for the radiative transfer equation was also adjusted. Different methods of parallelisation for the radiative transfer were tested.

Within ANTARES shocks are treated with an essentially non oscillatory (ENO) scheme with Marquina flux splitting. As this method is only valid for grids that are equidistant or uniformly stretched in all directions two differnt sets of ENO-coefficients were implemented and tested. It was found that the traditional approach is indeed no longer valid and the system is not conservative when the original set of coefficients is used.

In the upper or hydrogen ionisation zone the gradient of density, temperature etc. is very steep, therefore a finer resolution with a minimum of additional time steps is needed. In order to resolve these few points a co-moving grid refinement was developed.

Simulations in one and two dimensions were performed, a comparison between them helps to better understand the effects of convection on the e.c. light curve. Analysis of the fluxes and the work integral was done for the helium ionisation zone. The effects of subgrid modelling were tested on the hydrogen convection zone and compared with a resolved simulation of this zone.

Zusammenfassung

Um mit Hilfe des ANTARES-Codes eine Simulation von Pulsation und Konvektion in einem Cepheiden durchführen zu können wurde dieser mit einem polaren, beweglichen Gitter ausgestattet. Der numerische Aufwand für einen voll parallelisierten, ausreichend großen und ausreichend aufgelösten Ausschnitt des Sterns ist enorm. Daher war es nicht nur notwendig ein geeignetes Model zu finden, es musste auch bei der Parallelisierung und bei der Gitterverfeinerung der Aufwand im Vergleich zum bisherigen Programm reduziert werden.

Die hydrodynamischen Gleichungen wurden für dieses spezielle Gitter hergeleitet und in den Code implementiert. Die Methode der kurzen Charakteristiken für den Strahlungstransport wurde an dieses Gitter angepasst. Verschiedene Parallelisierungsvarianten wurden dafür untersucht.

Innerhalb von ANTARES werden Schocks mit Hilfe von ENO mit „Marquina flux splitting" behandelt. Diese Methode ist aber nur für equidistante oder gleichförmig gestreckte Gitter zulässig. Es wurden zwei verschiedene Familien von Koeffizienten getestet. Es hat sich gezeigt, dass der herkömmliche Zugang tatsächlich ungeeignet ist und zu einer Änderung der Erhaltungsgrößen führt.

In der oberen Konvektionszone, in der die Ionisation von Wasserstoff statt findet, sind die Gradienten von Dichte, Temperatur usw. sehr steil, hier wurde eine bessere Auflösung mit möglichst wenigen zusätzlichen Zeitschritten benötigt. Um diese sehr dünne Schicht aufzulösen wurde eine sich mitbewegende Gitterverfeinerung entwickelt.

Es wurden Simulationen in ein und zwei Dimensionen durchgeführt. In zwei Dimensionen wurden die Flüsse und das Arbeitsintegral in der Helium-Ionisationszone analysiert. Die Auswirkngen von „subgrid modelling" wurden an der Wasserstoff-Ionisationszone getestet und mit einer besser aufgelösten Simulation verglichen.

Contents

Chapter 1

Cepheid Modelling

1.1 Why we care

For the set of partial differential equations that govern the hydrodynamics inside a star (Chapter 2) no analytic solutions are possible so that one depends on numerical solutions. Consequently the activity and the number of results in this field has increased with the numerical capabilities.[1] For a long time one dimensional models have been the only option available for stellar modellers, the classical example is Local Mixing Length theory [BV 1958]. For the Sun detailed 3D-models which are in many respects superior to 1D-models have been around for three decades [NS 1999]. When comparing these models a number of discrepancies arise, the problems originate mainly in the surface layers where horizontal fluctuations become particularly large. On the other hand in 3D the agreement of synthetic and observed solar granulation is very good [Mut et al 2010a].

In order to better understand the processes in other stars, far less accessible to direct observation than the Sun, numerical models are necessary, but there arise new mathematical and numerical problems as pointed out in 3.7.3 , 3.8.3 and Section 4.3.

1.1.1 Cepheids as Variables

Cepheids are a subset of pulsating stars, which in turn comprise only a subset of the wider class of *intrinsic variable* stars. These are stars whose variability arises from causes entirely within themselves, and not from geometric effects such as eclipses in binary stars; or to some external agent such as interaction with the interstellar medium or with circumstellar matter. Pulsating stars are stars in which large-scale dynamical motions, usually including the entire star, and usually more or less rhythmic, are present. The simplest kind of such motion is a purely radial pulsation, in which the star maintains a spherical shape at all times, but changes its volume, as if it were breathing.

---

[1]Schwarzschild remarked in 1958: "A person can perform more than twenty integration steps per day", so that, "for a single integration consisting of, say, forty steps, less than two days are needed"

In 1900 Karl Schwarzschild [Schw 1900] compared the optical and the photographic light-curves of both ηAquilae and βLyrae, where the photographic plate was particularly sensit-ive to blue light. Both lightcurves of βLyrae are identical as to phase, form and amplitude and show the same fluctuation of ~ 0.8 magnitudes. This star's variability is clearly caused by obstruction, it is an eclipsing binary. But, when comparing the lightcurves of ηAquilae Schwarzschild found a difference in the amplitudes: 1.29 magnitudes in the photographic curve and 0.67 in the optical. He suggested two explanations: a variation in temperature or the tide of an absorbing atmosphere, that absorbs twice as much blue than yellow, as does the atmosphere of the Earth.

The idea that certain types of variable stars e.c. βLyrae owe their variability to periodic expansions and contractions dates from the work of Shapley (1914) and was given a firm mathematical foundation by Eddington [Edd 1917].

In this section we present two results derived by stellar modelling: The reason why Cepheids pulsate and the fact that the period must be linked to the mass of the star.

The kappa-mechanism.[LD 1982, BK 1962, HKT 1994]
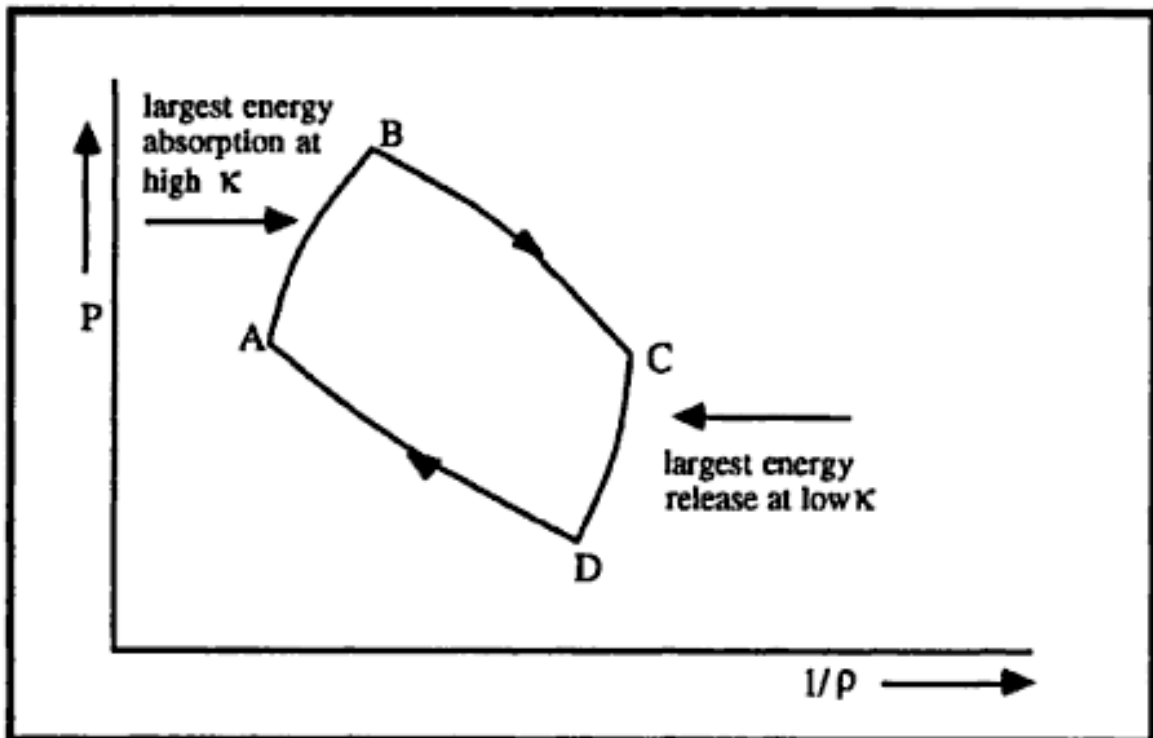
Figure 1.1.1:   the κ- mechanism

How the κ-mechanism works. Let us start the cycle in Figure 1.1.1 on page 10 at C where the star contracts, meaning that r decreases. Along CD energy is released at a growing rate (the absorption coefficient κ is small since T is low). In D maximum luminosity is attained together with maximum contraction velocity. Along the curve DA adiabatic

compression occurs, the inward velocity decreases. In the part AB of the cycle energy is absorbed due to larger κ which leads to increasing pressure P and accordingly the star expands (ρ decreases). This is the driving force of the pulsation. Between A and B, as ρ is already decreasing the pressure P still grows. This drives the layers outwards. This is the phase retardation between P and ρ which keeps the motor going.

The pulsation is driven by the opacity, modified by changing ionisation states. To start consider a completely ionised gas

$$\frac{dT}{T} = (\Gamma_3 - 1)\frac{d\rho}{\rho} \tag{1.1.1}$$

with Γ_3 the third adiabatic coefficient, defined by $\Gamma_3 - 1 = \frac{\rho}{T}\frac{dT}{d\rho}$. The opacity of stellar matter can in some approximation be written as $\kappa = C\rho^n T^{-s}$ with constant C and $n, s > 0$. We now consider a region where Kramers-opacity operates with $n = 1$ and $s = 3.5$, thus $\kappa = C\rho T^{-3.5}$. There ionisation is taking place but not as vigorously as it does near the half-ionisation points[2]. Thus set $\Gamma_3 = \frac{5}{3}$ assuming a non-ionising ideal gas. Equation (1.1.1) now yields $T \approx \rho^{2/3}$ and therefore $\kappa = C\rho^{-4/3}$. So with compression as ρ increases κ decreases and with expansion as ρ decreases κ increases. This means that in a completely ionised gas the κ-mechanism does not work.

We consider now an ionisation zone, like the H-, He- and He+ ionisation; there the situation is completely different. When in an ionisation zone the gas is compressed the mechanical energy of the compression will be used to increase the degree of ionisation and the temperature will rise only very slowly. Hence Γ_3 is only slightly larger than 1. Substituting $\Gamma_3 - 1$ by λ equation (1.1.1)gives $T \approx \rho^\lambda$ with $\lambda \approx 0$. The equation form Kramers' absorption reduces to

$$\kappa \approx \rho\rho^{-3.5\lambda} = \rho^{1-3.5\lambda} \tag{1.1.2}$$

for $(1 - 3.5\lambda) > 0$, κ will increase for compression and decrease for expansion, hence in the ionisation zones the κ-mechanism can proceed. The condition for pulsation is $(1 - 3.5\lambda) > 0$ or $\lambda < 2/7 \approx 0.28$.

This is in good agreement with $\Gamma_3 < \frac{4}{3}$ the condition for the limit of convective stability. In ionisation zones of an abundant element this condition is easily satisfied. However if the ionisation zones are situated too far inside the star, damping by the outer layers is very large and a starting pulsation is rapidly suppressed. Only when the H, He and He+ layers are at an optimum depth a persistent pulsation can be started, i.e. when these layers have a good heat capacity and do not have too much difficulty to retain the upper layers. In the instability strip these conditions are satisfied. A star of sufficient mass can cross the strip three or more times during its evolution.

---

[2]there the degree of ionisation $y = n^+/n = n_e/n = 1/2$ for hydrogen. The Saha equation yields that for hydrogen ionisation from the ground state, the transition from $y = 0$ to $y = 1$ takes place very rapidly. [HKT 1994] p 157, p217 and p398

The period-mean density relation.[3] Pulsations (at least those of low modes) can be regarded, approximately, as a kind of "long wave" acoustics, i.e wavelength of the "sound wave" is of the order of or larger than the dimension of the system. The pulsation period then ought to be of the order of the time required for a sound wave to propagate through the mean or equilibrium diameter of the star $\Pi \sim \frac{R}{c_s}$. A crude method of obtaining an expression for the mean sound speed is the following. The equation of hydrostatic equilibrium is used and all quantities therein are replaced by their averaged values throughout the star, thus $\bar{p} \sim \bar{\rho}^2 R^2$. Substituting the values into the expression for the sound speed yields $c_s \sim \sqrt{\bar{p}/\bar{\rho}}$ and therefore the length of a period is $\Pi \sim \frac{R}{c_s} \sim \frac{R}{\sqrt{\bar{\rho}R^2}} = \frac{1}{\sqrt{\bar{\rho}}}$ or

$$\Pi \left(\bar{\rho}\right)^{1/2} = constant \tag{1.1.3}$$

This is the famous period-mean density relation which seems to be satisfied approximately by most radially pulsating stars. To obtain the correct constant let's suppose that the entire mass M of the star is concentrated in a point at the centre and that the stellar surface lying at a mean distance R from the centre is represented by a thin spherical shell of this radius, having a mass m small compared with M and offering no resistance, other than inertia, to changing this radius. The entire volume within the shell is filled with a uniform, mass-less gas whose only function is to supply pressure to support the shell against gravity, and the shell is surrounded by vacuum (pressure $P = 0$). If r is the instantaneous radius of the membrane, its equation of motion is

$$m\ddot{r} = 4\pi r^2 P - \frac{GMm}{r^2} \tag{1.1.4}$$

Now assume small adiabatic oscillation about the hydrostatic equilibrium state $(\ddot{r} = 0)$; that is $\frac{\partial P}{P} = \Gamma_1 \frac{\partial \rho}{P}$, where ∂P denotes the departure of the pressure from its equilibrium value. Linearising equation (1.1.4) and assuming a time dependence of the form $e^{i\sigma t}$, it is a simple matter to show that the angular pulsation frequency σ is given by the relation

$$\sigma^2 = (3\Gamma_1 - 4)\frac{GM}{R^3} = (3\Gamma_1 - 4)\frac{4\pi}{3}G\bar{\rho} \tag{1.1.5}$$

which defines the mean density $\bar{\rho}$. For the pulsation period $\Pi = \frac{2\pi}{\sigma}$ this yields the following expression

$$\Pi = 2\pi \left[(3\Gamma_1 - 4)\frac{4\pi}{3}G\bar{\rho}\right]^{-1/2} \tag{1.1.6}$$

Interestingly enough, this is precisely the expression for the fundamental pulsation period of purely radial pulsations of the constant density model of given Γ_1 and $\bar{\rho}$.

1.1.2   The Mass-Luminosity Relation

For the astronomer the importance of classical Cepheids lies in their use as distance indicators. They are the most important tool for establishing the basic distance scale of

---

[3]See e.g. [Cox 1980]

the universe. This use is based on the well known period-luminosity relation, which was discovered by Leavitt of Harvard on the basis of Cepheids in the Small Magellanic Cloud. She noticed a remarkable relation between the brightness of these variables and the length of their periods [Lea 1912].

(a)   (b)
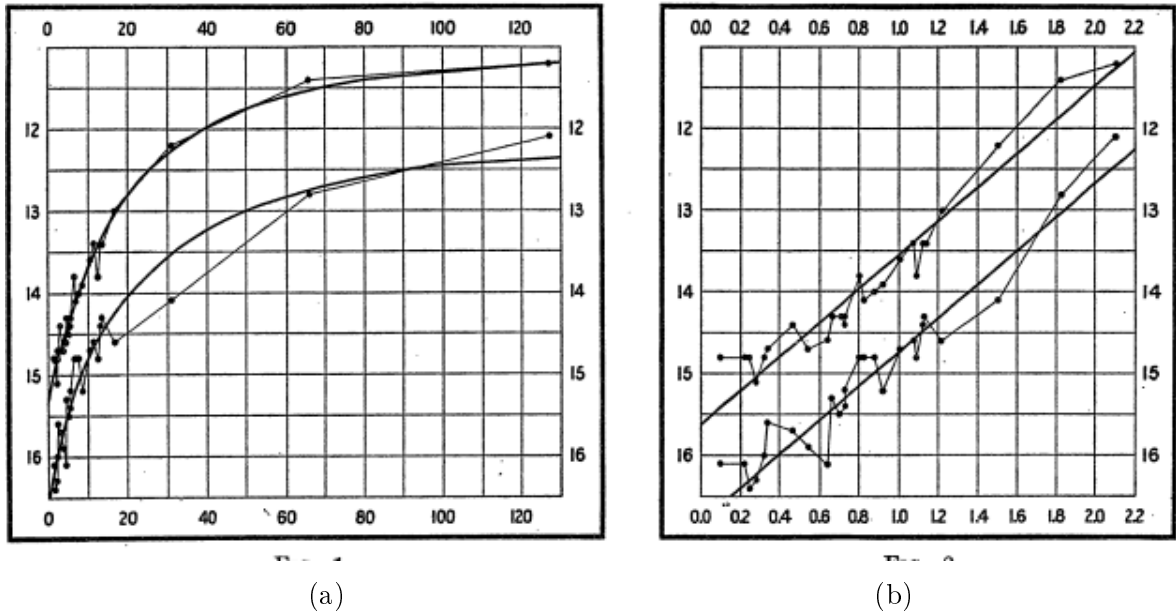
Figure 1.1.2:   period luminosity relation

The relation is shown graphically in Figure 1.1.2 on page 13 where in (a) the abscissas are equal to the periods, expressed in days, and the ordinates are equal to the corresponding absolute magnitudes at maxima and minima, in (b) the abscissas are equal to the logarithms of the periods. She stated therefore that the logarithm of the period increases by about 0.48 for each increase of one magnitude in brightness. So one may say [Cox 1980], that she found that the mean luminosity increases monotonically with increasing period, but she was unable to specify the zero point of the relation. The history of the determination of this zero point makes a fascinating chapter in the history of astronomy and has been described by Baade (1956, 1963) and Fernie (1969). Suffice it to say that the doubling of the distance scale of the universe in the early 1950's was the result of the discovery of an error in the earlier determinations of the zero point: this error had gone undetected for approximately forty years till its detection by Baade who used the then newly operative 200 inch Palomar telescope.

The period luminosity relation and the period-mean density relation together yield the mass-luminosity relation

$$log \left(\frac{L}{L_{\odot}} \right) = 1.15 log \Pi_d + 2.47 \qquad (1.1.7)$$

where $L_{\odot}$ denotes the solar luminosity. It is assumed that this relation holds true for all

Cepheids[4].

The cosmic distance ladder is the succession of methods by which astronomers determine the distances to celestial objects. A real direct distance measurement to an astronomical object is only possible for those objects that are "close enough" (within about a thousand parsecs) to Earth. For objects in the solar systems the first steps are radars, triangulation and Kepler's 3rd law. For nearby stars up to by now $10^3 pc$[5] trigonometric parallaxes can be used[6]. The techniques for determining distances to more distant objects are all based on various measured correlations between methods that work at close distances with methods that work at larger distances. Several methods rely on a standard candle, which is an astronomical object that has a known luminosity.
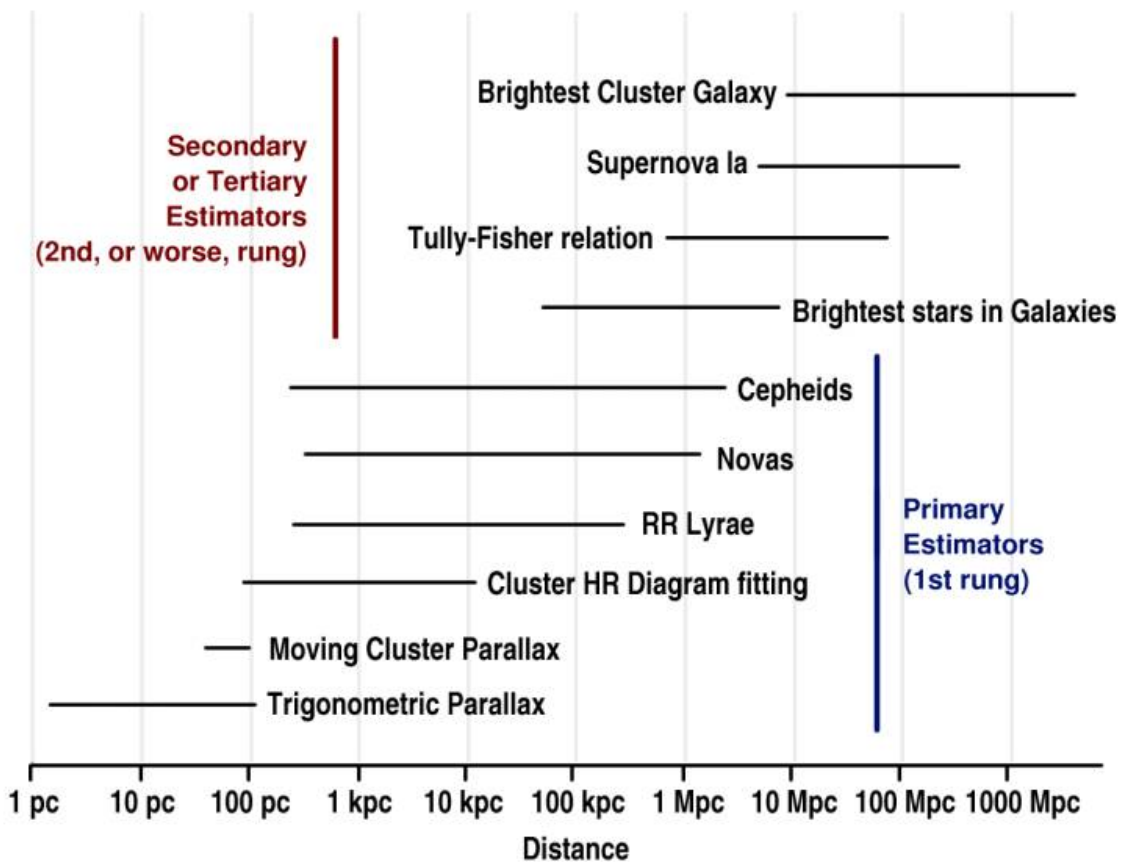
Figure 1.1.3:   the cosmic distance ladder

The ladder analogy arises because no one technique yields distances at all ranges, it only works within a certain range. Each rung of the ladder provides information that can be used to determine the distances at the next higher rung. In Figure 1.1.3 on page 14 one can

---

[4]Fernie (1967), Sandage and Tammann (1968, 1969, 1974, 1976a, b) and others conclude that there is no reason to doubt, that an "universal" period-luminosity relation exists for at least all the galaxies included in their study. However the universality of this relation is not entirely settled.

[5]Hipparcos satellite (ESA) (1990–93)

[6]parsec is short for parallax of one arc second (symbol: pc) $1pc \approx 31 \cdot 10^{12} km$ or 3.26 light-years

see that Cepheids are useful for a wide range from 10^3 to 10^7 pc. Beyond 10^8 pc and up the Tully-Fisher relationship which relates the velocity width and the luminosity of spiral galaxies is important.

In 1915 Harlow Shapley used Cepheids to place initial constraints on the size and shape of the Milky Way, and of the placement of our Sun within it.

In 1924 Edwin Hubble discovered Cepheid variables in the Andromeda (M31) galaxy. This settled the Island Universe debate, concerning the question of whether the Milky Way and the Universe were synonymous, or whether the Milky Way was merely one in a plethora of galaxies that constitutes the Universe.[7] He was able to calculate the distance of M31 to 285 Kpc, today's value being 770 Kpc.

Combining his calculations based on Cepheids of distances of galaxies with Vesto Slipher's measurements of the speed at which the galaxies recede from us, in 1929 Hubble and Milton L. Humason formulated what is now known as Hubble's law, concerning the expansion of the Universe.

The Hubble Space Telescope (HST) has found dozens of Cepheids in the galaxy M100 alone, the distance to which has been estimated thereby to be about 53 million light-years. It also made the most distant Cepheid measurement to date, of the galaxy NGC 4603 to be about 108 million light-years. By means of HST Cepheid observations, better constraints on Hubble's law have been calculated, and many characteristics of our galaxy and our relationship to it have been clarified, for example: the Sun's height above the galactic plane, the distance to the galactic centre, and the interpretation of the local galactic spiral structure[8].

The use of Cepheid variable stars is not without its problems however. At nearby galaxies they have an error of about 7% and up to a 15% error for the most distant. The largest source of error with Cepheids as standard candles is the possibility that the period-luminosity relation is affected by metallicity.

1.2 Short History of One Dimensional Simulations

The mathematical treatment of radial pulsations of stars has been developed through the use of three distinct degrees of approximation. The simplest approach, assuming linear, adiabatic oscillations was first used by Eddington (1918). When applied to models using accurate microphysics and opacities, this type of analysis portrays the overall mechanical aspects of the system quite well and predicts periods in good agreement with observations. To study the growth and decay of pulsations, however, non adiabatic effects must be included. The eigenvalue approach to the problem of linear, non adiabatic pulsations has

---

[7]Hubble, E. *Cepheids in spiral nebulae*, The Observatory, Vol. 48, p. 139–142 (1925)

[8]Majaess D. J., Turner D. G. and Lane D. J., *Characteristics of the Galaxy according to Cepheids.* Monthly Notices of the Royal Astronomical Society (2009)

produced a very good representation of small-amplitude pulsation. Several major surveys using up-to-date physics have been completed in this approximation and have provided valuable information regarding the physical basis of pulsation and the location of the instability strip in the H-R-Diagram. Even so, it is the limiting-amplitude behaviour of variable stars that is observed and this can only be studied using non-linear methods.

1.2.1   Baker and Kippenhahn

In [BK 1962] model envelopes for five population I stars in and near the δ Cephei region ($M = 11.5 M_\odot$, $L = 5000 L_\odot$, $T_{eff} = 5390^o$) of the H-R diagram have been investigated in order to study their stabilities against pulsation; that is to determine whether a small radial distortion of the equilibrium models decreases or increases with time in order to make the star pulsate like the observed pulsating variables.

A particular model is calculated for given values of M, L, T_{eff} and the chemical composition $X = 0.6$ the helium abundance Y is assumed to be $Y = 1 - X$.

The equations for the atmosphere consist of one for the dependence of temperature on the optical depth τ as given by [BV 1958] and one for pressure. This suffices to fix the values of P and T at $\tau = 2/3$ which is used to obtain an outer boundary condition for the equations which describe the inner structure.

The equations below the photosphere. One must integrate the following three equations for radiative energy transport and hydrostatic equilibrium under conditions of spherical symmetry:

$$\frac{d\ln T}{d\ln P} = \nabla_{rad} = \frac{3}{16\pi acG}\frac{\kappa L P}{M_r T^4} \tag{1.2.1}$$

$$\frac{d\ln r}{d\ln P} = -\frac{rP}{G\rho M_r} \tag{1.2.2}$$

$$\frac{d\ln M_r}{d\ln P} = -\frac{4\pi r^4 P}{G\rho M_r^2} \tag{1.2.3}$$

The integrations proceed from the photosphere up to a point "quite deep in the interior". The luminosity is assumed constant since there is no energy production in the region of interest. The density ρ is related to P and T through the equation of state:

$$\rho = \frac{\mu}{R_{gas}}\frac{\beta P}{T}, \qquad \beta = \frac{a}{3}\frac{T^4}{P}$$

The molecular weight depends on the chemical composition and on the degree of ionisation y_i of the three most important stages of ionisation (H, He, He+). Then

$$\mu = \frac{\mu_0}{1 + \sum_{i=1}^{3}\nu_i y_i}$$

where $\mu_0 = \frac{4}{1+3X}$, $\nu_1 = \frac{4X}{1+3X}$, $\nu_2 = \nu_3 = \frac{1-X}{1+3X}$ and the y_i may be obtained from the Saha equation.

The actual integration of an equilibrium model is carried out as follows: The quantities L, T_{eff} and M are given for a particular star. Then the radius R of the photosphere can be obtained from L and T_{eff}:

$$R = \frac{1}{T_{eff}^2} \sqrt{\frac{L}{\pi a c}}$$

Therefrom the structure of the atmosphere is determined and one obtains the pressure and temperature for all points $\tau \leqq 2/3$: From this point on equations (1.2.1) to (1.2.3) are integrated inward beginning with a mesh size $\Delta \log P = 0.02$. The mesh size is doubled or halved automatically depending on the precision of the result as determined by the difference between extrapolated and interpolated values. In the very sensitive region where the opacity increases rapidly due to H- absorption the mesh becomes as small as one sixteenth of the original size. The integration is carried out up to a maximum pressure $\log P = 8$.

The equilibrium models. Model I closely resembles δ Cephei with a period of 6 days, for models II and III temperature was increased, the periods became shorter. For model IV luminosity was increased and for model V mass decreased both resulting in longer periods. Then the pulsational oscillations of these models were investigated.

The results may be summarised as follows[9]: "In the region of the H-R diagram near the position of δ Cephei the He+ ionisation zones give sufficient excitation to the pulsations to overcome the damping. The damping of a given star increases strongly with decreasing period, so that it is plausible that a normal star pulsates only in its fundamental mode and not simultaneously in an overtone. Assuming that the (lowest) characteristic pulsation of a star satisfies the period-density relation during a part of the stars evolution, it is found that stars which lie to the left of the Cepheid region in the H-R diagram no longer pulsate, because in them the excitation is smaller than damping."

1.2.2 Christy

In [Chr 1964] and [Chr 1966a] the author set out to demonstrate that the observed pulsation motions in Cepheids and RR Lyrae stars arise spontaneously because of the particular physical properties of the envelopes. The relevant physical properties being the equation of state and the opacity. The equation of state in question was obtained by assuming a perfect gas of H, H^+, He, He^+, He^{++} and electrons. H_2 was ignored. The relative numbers of the various ions were determined by solving the Saha equation of equilibrium, ignoring pressure ionisation, ionic interaction etc. The contribution of the various ionic species to the pressure and internal energy including the ionisation energy was computed. The opacities used were Rosseland mean opacities obtained from A.N. Cox and J.N. Steward, they included the effects of bound-bound transitions in addition to the usual bound-free, free-free and scattering contributions.

---

[9]from [BK 1962] p 117

In order to integrate numerically the partial differential equations $\frac{\partial^2 r}{\partial t^2} = -\frac{GM}{r^2} - 4\pi r^2 \frac{\partial P}{\partial M}$ and $\frac{\partial E}{\partial t} + P\frac{\partial V}{\partial t} + \frac{dL}{dM}$ of motion where $L = -\left(4\pi r^2\right)^2 \frac{4\sigma}{3\kappa}\frac{dT^4}{dM}$ they are expressed as difference equations. Shock waves are treated by the von Neumann-Richtmyer method, which involves the introduction of an artificial viscosity which creates a pressure on rapid compression but none on expansion. The viscous pressure is given by

$$Q^{n-\frac{1}{2}}\left(I - \frac{1}{2}\right) = \begin{cases} C_q \frac{\left[U^{n-\frac{1}{2}}(I) - U^{n-\frac{1}{2}}(I-1)\right]^2}{V^n(I-\frac{1}{2}) - V^n(I-\frac{1}{2})} & U(I) - U(I-1) < 0 \\ 0 & U(I) - U(I-1) \geq 0 \end{cases} \tag{1.2.4}$$

where $\Delta M\left(I - \frac{1}{2}\right) = M\left(I\right) - M\left(I - 1\right)$ and the specific volume of the mass element at $I - 1$ is $V^n(I - \frac{1}{2}) = \frac{4\pi}{3}\left\{[R^n\left(I\right)]^3 - [R^n\left(I - 1\right)]^3\right\}/\Delta M\left(I - \frac{1}{2}\right)$. Further equations are for the radius

$$R^{n+1}\left(I\right) = R^n\left(I\right) + \Delta t^{n+\frac{1}{2}} U^{n+\frac{1}{2}}\left(I\right)$$

the velocity

$$U^{n+\frac{1}{2}}\left(I\right) = U^{n-\frac{1}{2}}\left(I\right) - \Delta t^n \left\{ \frac{GM(I)}{[R^n(I)]^2} + \frac{4\pi[R^n(I)]^2\left[P^n\left(I+\frac{1}{2}\right) - P^n\left(I-\frac{1}{2}\right) + Q^n\left(I+\frac{1}{2}\right) - Q^n\left(I-\frac{1}{2}\right)\right]}{\Delta M(I)} \right\}$$

and the energy transport

$$\left(E^{n+1}\left(I + \frac{1}{2}\right) - E\left(I + \frac{1}{2}\right) + \left\{\frac{1}{2}\left[P^n\left(I + \frac{1}{2}\right) + P^{n+1}\left(I + \frac{1}{2}\right)\right] + Q^{n+\frac{1}{2}}\left(I + \frac{1}{2}\right)\right\}\right.$$
$$\left[V^{n+1}(I + \tfrac{1}{2}) - V^n(I + \tfrac{1}{2})\right]\big)\,\Delta M\left(I + \frac{1}{2}\right) =$$
$$\frac{1}{2}\Delta t^{n+\frac{1}{2}}\left[L^{n+1}\left(I\right) + L^n\left(I\right) - L^{n+1}\left(I + 1\right) - L^n\left(I + 1\right)\right]$$

where the total luminous flux through radius $R^n\left(I\right)$ is given by

$$L^n\left(I\right) = \left\{4\pi\left[R^n\left(I\right)\right]^2\right\}^2 \left[W^n\left(I - \frac{1}{2}\right) - W^n\left(I + \frac{1}{2}\right)\right] 2F^n\left(I\right)$$

here $W = T^4$ and $2F^n\left(I\right)$ is a suitable difference approximation to $\frac{4}{3}\sigma/\kappa\Delta M$.

The solution of the energy transport equation for the new temperature presents an additional problem since the equation is nonlinear, it was solved by a process of iteration. Radiative transfer was included as diffusion approximation and convection was omitted.

The domains started at an outer border of $P = 0$ and the depth of the envelope was chosen so that the estimated sound travel time through the remaining core was less then 1 percent of the total sound travel time through the envelope. This involved an envelope mass of about 2 percent of the stellar mass and a temperature at its base greater then $10^6 K$. The radius of the base was never greater than $\frac{1}{7}$ of the stellar radius. The domain was equipped with a grid of mass points such that the ratio of successive values of ΔM is constant. It was found that 30 to 40 points was sufficient (!). Occasionally calculations with up to 100 mass points have been used but could not be followed over many periods. In order to cover the envelope in about 35 steps it was necessary to use $\Delta M\left(I - 1\right)/\Delta M\left(I\right)$ up to 1.5.

The initial condition. Since the solution is expected to only depend on the equation of state and the opacities, Christy states that if starting from arbitrary initial conditions presumably in the course of time the solution would settle down to the correct final state, either static or pulsating as the case might be. Since this would take a lot of time the initial condition of the time dependent problem is based on the solution of the static envelope problem for the same star and initiating the pulsation by superimposing some arbitrary $U(M)$. This procedure initiates a mixture of harmonics. Of this mixture only the few lowest harmonics survived long.

In [Chr 1966a] non-linear calculations for one hundred RR Lyrae models have been carried out in order to investigate stability, the dependence of the location of the instability strip on composition, mass and luminosity. When exploring the source of the driving energy of these models it was found that in the models of the most favoured composition, 30 percent helium, the hydrogen ionisation region is almost as important to the driving as the He II ionisation. Christy points out the advantages of non-linear treatment that: „When Baker and Kippenhahn [BK 1962] attempted to include this zone they pointed out two particular peculiarities of this region when linear calculations are used. First, the behaviour of this region is sensitive to the outer boundary conditions employed. Second, the amplitude of, for example, the temperature variation in the hydrogen zone is very large. Now the non-linear theory (and observations) show that the description must be in terms of a moving front. Thus there is a relatively thin layer of the star in which the temperature rises from photospheric values to 20000 or 30000 K. This steep temperature front then moves up and down through a considerable mass in the course of the cycle of pulsation. The front is also steeper when it is moving out and less steep when it recedes. In the linear approximation, a steep moving front appears almost as a singularity in the amplitude. The out-of-phase terms in the amplitude show the motion of the front, but the actual amplitude of the variations in this region can only be seen from non-linear terms. Thus the linear theory shows an excessively large amplitude in a region of negligible thickness whereas the actual motion involves a large (but finite) amplitude in a region of considerable thickness. The significance of the hydrogen zone is related to how far the front actually moves and how much phase delay it can introduce into the light-curve, and these questions seem almost impossible to answer from the linear theory.“

1.2.3 Cox

A similar program was developed in [CBE 1966] solving the Navier-Stokes equations together with the Rosseland radiation-diffusion equation, the standard conduction equation in a Lagrangian system. Shocks are treated with the von Neumann-Richtmyer artificial viscosity method.

The main difference to the approach in section 1.2.2 is the inclusion of a mixing-length type of equation for the convective energy transport thus approximating the effects involving two

or more dimensions needed to describe convective energy-transport. A simplified method of calculating time-dependent convection has been developed. The convective flux is changed slowly so that the flux at time n is

$$F_{c,i}^n = F_{c,i}^{n-1} + \frac{v_i^{n-\frac{1}{2}} \Delta t}{L_i^{n-\frac{1}{2}}} \left(F_{c,i} - F_{c,i}^{n-1} \right)$$

where $L_i^{n-\frac{1}{2}}$ is the average mixing length and $F_{c,i}$ is calculated using

$$F_{c,i} A_i = \frac{2}{g_i L_i Q_i} \left[\frac{A_- \Gamma_{i-\frac{1}{2}} \left(\frac{\partial E}{\partial T} \right)_{V,i-\frac{1}{2}} T_{i-\frac{1}{2}}}{V_{i-\frac{1}{2}}} + \frac{A_+ \Gamma_{i+\frac{1}{2}} \left(\frac{\partial E}{\partial T} \right)_{V,i+\frac{1}{2}} T_{i+\frac{1}{2}}}{V_{i+\frac{1}{2}}} \right] v_i^3$$

at time n. Here Γ is the ratio of specific heats $\frac{c_p}{c_V}$, $A_\pm = 4\pi r_\pm^2$, $r_\pm = \frac{1}{4}(r_{i\pm 1} + 3r_i)$ and Q_i is a dimensionless quantity defined by Böhm-Vitense [BV 1958].

In [CCOKE 1966] these computation techniques were used to study self-excited radial pulsations in stellar-envelope models and the basic physics of the destabilising mechanism arising from He^+ionisation in the envelopes. The mass of the envelope is about 10^{-4} of the total stellar mass ($= 5.395\,M_\odot$). The temperature at the bottom was $10^5 K$, still high enough to include the entire He^+ionisation zone. The bottom boundary was kept fixed in time at 0.8-0.9 % of the total stellar radius and a constant luminosity was fed into the envelope from below. The entire mass to be included was divided into up to 150 mass zones, normally 50 mass zones were used, the mass ratio between consecutive cells being 1.3. The envelope was initially set to a good approximation of hydrostatic equilibrium so that the velocities of all interfaces were very small at the outset. This requirement was then removed and the subsequent time behaviour of the envelope was calculated. Stable envelopes were distinguished from unstable ones after some ten-to-thirty pulsation periods. Unstable envelopes developed radial pulsations whose amplitude grew exponentially to some limiting amplitude in several hundred periods, this process was sped up by multiplying the velocity by a factor 10. The properties of the pulsations at limiting amplitudes were found to be independent of the method of reaching it. Most of the unstable envelopes studied (about eleven) had $\delta R/R_0 \approx 0.04 - 0.05$, total surface velocity amplitude $\approx 60 - 70 km/sec$, and total bolometric light range $\approx 0.3 - 0.4 mag$. The relative smallness of the radial variations suggested to the authors that the limiting amplitude is determined primarily by a „saturation effect" of the driving mechanism.

The results showed that the opacity variations and the small values of the $\Gamma_3 - 1$ in the He^+ ionisation zone both produce negative dissipation in and above this region. Evidence was also found for the existence of negative dissipation in the H ionisation region. But to avoid having to deal with problems of radiative transfer in optically thin regions the mass of the outermost zone was chosen sufficiently large so that the optical depth of the zone remained large compared to unity at all times. In the case of 50-zone models the outermost 10 zones had masses comparable to that of the fiftieth zone. Because of this

requirement of fairly massive zones in the outermost regions the effects of hydrogen and first helium ionisation (while included in the opacity and equation-of-state tables) were hardly treated as these two zones together were generally confined to only one or two mass zones. Consequently reliable information on phase relations between luminosity and radial velocity was not obtained.

Two „envelope instability strips" corresponding to a pure He/H and an Aller mix (including metals) were investigated. Some disadvantages of using only envelopes (thickness $\leq 0.15R$) instead of complete stellar models were found to be: the pulsation periods of the models were too short, the correct details of the luminosity- and radial-velocity-curves could not be obtained.

1.2.4 Stellingwerf

Since the usual nonlinear approach of the above sections has proved to be computationally extremely expensive at the time, in [Ste 1974] a scheme for relaxation to a periodic solution as well as a method of limit cycle stability analysis was developed. The developed procedures were intended to be included as additions to an existing nonlinear hydrodynamic code. This code was treated as a „black-box" in the sense that the physical and mathematical details were not regarded.

Assume that we have a stellar model with J mass zones and I variables per zone. Let $K = IJ$ and list all the variables by zone in the K-dimensional vector z. z^n is the set of structure variables at step n, and N the total number of steps in one period Π. $\bar{z}$ denotes the desired periodic solution with period $\bar{\Pi}$. That is $\bar{z}$ satisfies the periodic boundary conditions

$$\bar{z}^0 - \bar{z}^N = 0 \qquad (1.2.5)$$

and for uniqueness also satisfies the phase condition

$$\bar{z}_i^0 - \bar{z}_{i,0}^0 = 0 \qquad (1.2.6)$$

for some particular i, this condition means that the phase of the solutions is fixed by picking a variable and arbitrarily setting its value at time 0 to $\bar{z}_{i,0}^0$, e.c. setting the outer velocity (at time zero) equal to zero. The overall problem is to find all such periodic solutions of a given model. Note that once $\bar{z}^0$ and $\bar{\Pi}$ are given the black-box code can generate the entire solution. Each periodic mode was searched for separately. To begin the relaxation to the solution $\bar{z}$ guess the time 0 values as usual and make a guess for the actual period $\bar{\Pi}$. Insert z^0 and Π into the black box code and obtain z^N. It is assumed that the hydrodynamic code operates smoothly and the derivatives $\partial z^N / \partial z^0$ and $\partial z^N / \partial \Pi$ are available. The desired solution is written

$$\begin{aligned} \bar{z}^0 &= z^0 + \delta z^0 \\ \bar{\Pi} &= \Pi + \delta\Pi \end{aligned} \qquad (1.2.7)$$

Regarding z^N as a function of z^0 and Π equation (1.2.5) becomes

$$\left(Id - \frac{\partial z^N}{\partial z^0}\right)\delta z^0 = z^N - z^0 + \frac{\partial z^N}{\partial \Pi}\delta \Pi \qquad (1.2.8)$$

Solving this set of equations for δz^0 we obtain a relation of the form

$$\delta z^0 = c\delta \Pi + d \qquad (1.2.9)$$

Using equation (1.2.7), equation (1.2.6) becomes

$$\delta z_i^0 = \bar{z}_{i,0}^0 - z_i^0 \qquad (1.2.10)$$

this specifies δz_i^0 and in turn fixes $\delta \Pi$ in the ith component of equation (1.2.9):

$$\delta \Pi = \left(\bar{z}_{i,0}^0 - z_i^0 - d_i\right)/c_i \qquad (1.2.11)$$

The other components of δz^0 are then given by substituting this value of $\delta \Pi$ in equation (1.2.9) and the new approximation to $\bar{z}^0$ is then given by equation (1.2.7). The process is repeated until the corrections δz^0 are sufficiently small.

To settle the question of stability consider an arbitrary perturbation δz^0 of the periodic solution $\bar{z}^0$, define $C^n = \frac{\partial z^n}{\partial z^0}$. For a fixed Π this matrix has the properties of a transformation in time of δz^0: $\delta z^n = C^n \delta z^0$ in particular

$$\delta z^N = C^N \delta z^0 \qquad (1.2.12)$$

Now suppose that δz^0 has been picked to be an eigenvector of C^N with eigenvalue k; equation (1.2.12) then becomes

$$\delta z^N = k\delta z^0 \qquad (1.2.13)$$

The eigenvectors of C^N therefore form a set of perturbations, after each period the perturbation merely scales by the complex constant k. Regarding the components of the perturbation as smooth functions of time $\delta z(t)$ and putting $\eta = (1/\Pi)/\log k$ we find from equation (1.2.13) that $\delta z(t) = e^{\eta t}\phi(t)$ where $\phi(t) = e^{-\eta t}\delta z(t)$ is periodic with period Π. So, although the perturbation may not be periodic it contains the secondary period given by

$$\Pi_{pert} = \frac{2\pi}{Im(\eta)} = \Pi\frac{2\pi}{arg(k)} \qquad (1.2.14)$$

The eigenvectors δz span the space of all possible perturbations of the motion; the star therefore, will depart from periodic motion in the sense of linear perturbation theory if and only if the modulus of some eigenvector is greater than unity. A flow chart for the entire calculation is shown in figure 1.2.1.
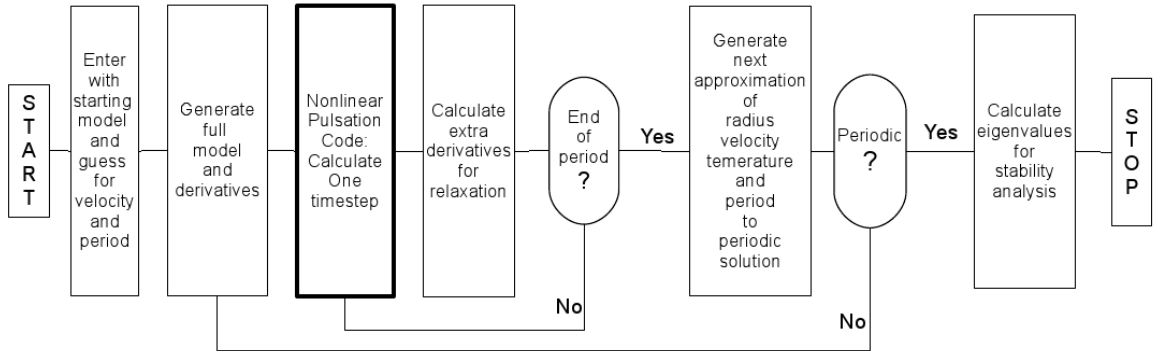
Figure 1.2.1:   flow chart for the relaxation

In [Ste 1975] the modal stability of RR Lyrae stars has been investigated with this method and both the growth rates of the small-amplitude solutions and the mode switching rates of the small-amplitude solutions were obtained, resulting in a complete description of the long term modal behaviour of the model. A standard mass $M = 0.578M_\odot$ and composition ($Y = 0.3, Z = 0.002$) were adopted, thus restricting the survey to two parameters: luminosity and effective temperature. Each model had 29 zones with the inner boundary at $r_0 = 0.66R$ and $T_{25} = 11000°K$. The zone mass ratio h is $1.2 \leq h \leq 1.6$. The nonlinear stability results show a narrow (300° K wide in T_{eff}) region of „ fundamental or first harmonic" behaviour whose blue edge is nearly the same as the linear fundamental blue edge. In a large region towards the red these models show aperiodic mixed-mode behaviour similar to that observed for several stars; the mass and radius for the mixed-mode RR Lyrae star AC And were derived and found to be in good agreement with pulsational and evolutionary results.

1.2.5   More Recent Results[10]

Since the early works mentioned above there has been little basic progress. The quality of the opacities that are now used is much better (OPAL[11], OP[12] and Andersen-Ferguson[13]). In addition some treatment of convection is necessary and is routinely included in the calculations in the form of time-dependent mixing length. Parallel to direct numerical simulations, however, the amplitude equation formalism has been developed in the 1980's. The physical conditions that prevail in Cepheids and RR Lyrae stars, namely that the growth rates of the dominant modes are small compared to their frequencies, form the basis for the applicability of these techniques. Amplitude equations, or normal forms as they are known in nonlinear dynamics, are very general and describe the underlying mathematical

---

[10]In this chapter I follow the overview given by Buchler [Buc 2009]

[11]From investigators (Rogers, F,J., & Iglesias, C.A.) at the Lawrence Livermore National Laboratory (LLNL) in Livermore, CA. see e.g.[RSI 1996]

[12]Seaton, M.J. 1995, ed. *The Opacity Project*, Vol. 1 (Bristol: Institute of Physics Publishing)

[13]see [AF 1994]

structure of the pulsations. When combined with numerical simulations, they provide not only an excellent description of the modal selection problem, e.g. of where the region of double mode behaviour or hysteresis occur, but they also yield a deeper understanding of these bifurcations in the pulsational behaviour.

The ingredients of time dependent mixing length. The effects of turbulence and convection in one-dimensional hydrodynamics appear via the turbulent pressure and viscous stresses p_t and p_v, the convective flux F_c and the energy coupling term:

$$\frac{du}{dt} = -\frac{1}{\rho}\frac{\partial}{\partial r}\left(p + p_t + p_v\right) - \frac{GM_r}{r^2} \tag{1.2.15}$$

$$\frac{de}{dt} + p\frac{dv}{dt} = -\frac{1}{\rho r^2}\frac{\partial}{\partial r}\left[r^2\left(F_r + F_c\right)\right] + C \tag{1.2.16}$$

The turbulent and convective quantities are supposed to be functions of the „turbulent energy" e_t that is assumed to satisfy

$$\frac{de_t}{dt} + \left(p_t + p_v\right)\frac{dv}{dt} = -\frac{1}{\rho r^2}\frac{\partial}{\partial r}\left(r^2 F_t\right) - C \tag{1.2.17}$$

Expressions for p_t, F_t, p_v and C can be derived in analogy with gas kinetic theory, however without the same solid physical basis. All these terms include α-parameters of $O(1)$ and physics provides little guidance for their values. There is also some ambiguity about the physical acceptability of the terms for F_c and the source term S_t that appears in the equation of the energy coupling term C:

$$
\begin{aligned}
F_c &\sim \alpha_c e_t^{1/2} Y \qquad or \quad F_c \sim \alpha_c e_t Y^{1/2} \\
S_t &\sim \alpha_S e_t^{1/2} Y \qquad or \quad S_t \sim \alpha_S e_t Y^{1/2}
\end{aligned} \tag{1.2.18}
$$

where

$$Y \equiv \left[-\frac{H_p}{c_p}\frac{\partial s}{\partial r}\right]_+ \qquad or \quad Y \equiv -\frac{H_p}{c_p}\frac{\partial s}{\partial r} \tag{1.2.19}$$

During the last decades mixing length theory has achieved many successes:[14]

1. One of the most striking properties of the Cepheids both for the fundamental and the first overtone mode pulsations is the progression of the Fourier decomposition coefficients of the lights curves and the radial velocity curves. Full amplitude Cepheid model sequences do a good job reproducing the Fourier properties of the F and the O1 Cepheids.

2. The amplitude equation formalism that was developed for explaining the effect of internal resonances on the appearance of light and radial velocity curves has demonstrated that it is the 2:1 resonance between the self-excited F mode and the vibrationally stable but resonant second overtone that is responsible for the structure of the Fourier coefficients for periods around 10 days rather than a shock wave that reflects off the core. For the first

---

[14]Relevant publications are listed in [Buc 2009]

overtone Cepheids it is the 2:1 resonance of the stable fourth overtone with the self excited first overtone that causes structure at periods in the vicinity of 4 days.

3. A full amplitude model survey of F and O1 Cepheids has found that the phase lag between light and radial velocity curves is in good agreement with observations. This study has furthermore demonstrated that the phase lag can also be used observationally as a discriminant between F and O1 mode pulsations.

4. The period ratio P_1/P_0 as a function of P_0 of the beat Cepheids is a sensitive function of the metallicity Z. This property has recently been taken advantage of to determine the metallicities in the LMC and SMC with the help of Cepheid modelling. The same method has been applied to the 5 known beat Cepheids in M33. Interestingly this yields a galactic metallicity gradient for M33 that is in good agreement with results from totally independent methods.

5. A comparison of light curves of full amplitude bump Cepheid models with observed light curves can also be used as a metallicity tracer and distance indicator.

6. Theoretical period-colour-luminosity relations are in good agreement with observational ones.

7. Theory has been ahead of observations by predicting the existence of strange Cepheids and RR Lyrae that pulsate in a high (7th to 12th) overtone in which the pulsation is confined to the outer region, more specifically, above the hydrogen ionisation front. Typically the predicted periods of these self exited modes are 4 to 5 times smaller than the fundamental period of the same object. The amplitudes are predicted to be in the millimag range. On the observational side some evidence for the existence of strange Cepheids has been found. However it is hard to distinguish between intrinsic pulsations and ellipsoidal binary motion at the millimag level.

There are a number of well known problems with time dependent mixing length theory. In the first place it is a phenomenological rather than consistent physical description, then MLT is a local approximation whereas 3D simulations show that plumes are a highly non local phenomenon. Moreover a number of (up to 8 or more) α-parameters appear in time dependent mixing length models and physics provides no guidance for their values. Therefore some of these parameters are calibrated with the help of a comparison of the results with observations, but there is a wide range to choose from. The less important parameters are fixed arbitrarily. It is somewhat disturbing that one needs a different set of α-values for RR Lyrae stars and for Cepheids and for different metallicity.

On the other hand amongst the list of known problems of MLT are some serious discrepancies for which stellar evolution calculations are at fault but on which Cepheid modelling unfortunately has to rely.

First, low mass, low Z (metallicity) evolution loops do not penetrate the instability strip where Cepheids are actually observed. It has been suggested that this could be a metallicity selection effect. There remains disagreement about the treatment of convection and

convective overshoots which leads to uncertainties in the Cepheid Mass-Luminosity-Z relation. Unfortunately this in turn causes uncertainties in Cepheid modelling which depends on a ML relation. Since time dependent mixing length has these problems efforts have been made to go beyond the simple model described above, while keeping its 1D feature. This unfortunately leads to a proliferation of equations with a concomitant numerical cost and perhaps little guarantee of substantial improvement.

According to Buchler there remain two great challenges for the modelling of Cepheids, and for that matter of RR Lyrae stars which are quite similar in many ways. These are the modelling of multidimensional convection in the highly structured envelopes of Cepheids on the one hand[15], and of non radial pulsations on the other.

---

[15] And indeed the two dimensional simulation of convection is tackled in this thesis.

Chapter 2

The Equations

2.1 The Equations of Hydrodynamics

In order to extend the ANTARES-code [Mut et al 2010a, Mut et al 2007, Mut et al 2010b] for Cepheid modelling it is necessary to use a radially moving, spherical grid and formulate the equations accordingly [WNM 1984]. One must restate the conservation relations for the radiating fluid in terms of a logical[1] mesh in the adaptive coordinate system. At the beginning I will formulate all equations as integral conservations relations of fluid contained in definite volumes of the adaptive coordinate system (hence fixed values of logical mesh-indices). This approach is satisfying both physically and intuitively and is well posed computationally for it can be employed in such a way as to guarantee global conservation within the flow. Three different time derivatives are used in an adaptive coordinate system: The Eulerian derivative taken with fixed coordinates in the laboratory frame, the Lagrangean (or co-moving) derivative taken with respect to a definite volume element and the moving-mesh derivative taken with respect to fixed values of the mesh-coordinates, which are neither fixed in the laboratory frame nor in the fluid.

Thus the Eulerian fluid velocity is

$$\vec{u} = D\vec{r}/Dt \tag{2.1.1}$$

where $\vec{r} = \vec{r}(\vec{r_0}, t)$ is the position of a definite point ("molecule") in the fluid, and the grid velocity is

$$\vec{u_g} = d\vec{r}/dt \tag{2.1.2}$$

where $\vec{r} = \vec{r}(i, j, k, t)$ is the position of a definite set of grid coordinates (specified by (i, j, k)). The relative velocity of the fluid with respect to the adaptive grid is then $\vec{u}_{rel} = \vec{u} - \vec{u}_g$. As usual the Lagrangean and the Eulerian derivatives of any quantity f are related by

$$(Df/Dt) = (\partial f/\partial t) + (\vec{u} \cdot \nabla) f \tag{2.1.3}$$

---

[1][WNM 1984] use this expression for the mesh of indices

and the moving-grid and the Eulerian derivatives are related by

$$(df/dt) = (\partial f/\partial t) + (\vec{u} \cdot \nabla) f \tag{2.1.4}$$

If J_f denotes the Jacobian of the transformation between the coordinates defining an initial fluid volume dV^0_{fluid} and the volume $dV_{fluid} = J_f dV^0_{fluid}$ of the same fluid at a later time one has the Euler expansion formula

$$D\left(lnJ_f\right)/Dt = \nabla \cdot \vec{u} \tag{2.1.5}$$

which in turn leads to the Reynolds transport theorem [CM 1990]

$$\frac{D}{Dt}\left(\int_{V_{fluid}} f dV_{fluid}\right) = \int_{V_{fluid}} \left[\frac{\partial f}{\partial t} + \nabla \cdot (\vec{u}f)\right] dV_{fluid} \tag{2.1.6}$$

By precisely the same analysis one can expand these theorems to the adaptive coordinate system. Now writing $dV = JdV^0$ to relate a moving-mesh volume dV to its original volume dV^0 we obtain the moving-mesh expansion formula

$$D\left(lnJ\right)/Dt = \nabla \cdot \vec{u}_g \tag{2.1.7}$$

and the moving mesh transport theorem

$$\frac{d}{dt}\left(\int_V f dV\right) = \int_V \left[\frac{\partial f}{\partial t} + \nabla \cdot (\vec{u_g}f)\right] dV \tag{2.1.8}$$

$$= \int_V \frac{\partial f}{\partial t}dV + \int_{\partial V} f\vec{u}_g \cdot \overrightarrow{dS}$$

In equation (2.1.8) V denotes a definite volume corresponding to fixed values of the adaptive coordinates. Note also that this equation reduces correctly to the Eulerian and Lagrangean limits. For $\vec{u}_g \equiv 0$ the grid is fixed in the laboratory frame and equation (2.1.8) becomes

$$\frac{d}{dt}\left(\int_V f dV\right) = \frac{\partial}{\partial t}\int_V f dV = \int_V \frac{\partial f}{\partial t}dV \tag{2.1.9}$$

whereas if we set $\vec{u}_g \equiv \vec{u}$ the grid is fixed in the fluid and equation (2.1.8) reduces to equation (2.1.6).

Although equations (2.1.7) and (2.1.8) can be derived purely formally, it is satisfying to notice that they are also intuitively obvious from equations (2.1.5) and (2.1.6). In both cases we have chosen a set of markers moving in the laboratory frame. In equations (2.1.5) and (2.1.6) the markers are identified with bits of fluid moving according to a velocity field $\vec{u}$, whereas in equations (2.1.7) and (2.1.8) they are identified with a logical grid, moving according to a velocity field $\vec{u}_g$. From equation (2.1.8) and the standard Lagrangean equation of continuity

$$(D\rho/Dt) = -\rho\left(\nabla \cdot \vec{u}\right) \tag{2.1.10}$$

the useful result

$$\frac{d}{dt}\left(\int_V f dV\right) = \int_V \left[\rho \frac{D}{Dt}\left(\frac{f}{\rho}\right) - \nabla \cdot (\vec{u}_{rel}f)\right] dV \qquad (2.1.11)$$

$$= \int_V \rho \frac{D}{Dt}\left(\frac{f}{\rho}\right) dV - \int_{\partial V} \vec{u}_{rel}f \cdot \partial S$$

is derived. (2.1.11) gives the moving volume integral of a Lagrangean time derivative; V again denotes a definite volume in the adaptive coordinate system.

Now let $f = \rho$ in (2.1.11) an we get the integral version of equation of continuity in moving coordinates

$$\frac{d}{dt}\left(\int_V \rho dV\right) = \int_V \left[-\nabla \cdot (\rho\vec{u}_{rel})\right] dV \qquad (2.1.12)$$

Since $\vec{u}_{rel} = \vec{u} - \vec{u}_g$ and $\vec{I} = \rho\vec{u}$ conservation of mass as expressed by the continuity equation becomes:[2]

$$\frac{\partial \rho}{\partial t} = -\nabla \cdot \left[\vec{I} - \rho\vec{u_g}\right] \qquad (2.1.13)$$

Conservation of momentum and energy are derived in the same way. The results are:

Conservation of momentum

$$\frac{\partial \vec{I}}{\partial t} = -\nabla \cdot \left[\frac{\vec{I}\vec{I}}{\rho} - \vec{I}\vec{u_g} - \overline{\sigma}\right] - \nabla p + \rho\vec{g} \qquad (2.1.14)$$

or since polar coordinates are used

$$\frac{\partial \vec{I}}{\partial t} = -\nabla \cdot \left[\frac{\vec{I}\vec{I}}{\rho} - \vec{I}\vec{u_g} - \overline{\sigma} + p \cdot Id\right] + \frac{2p}{r} + \rho\vec{g} \qquad (2.1.15)$$

Conservation of "total" energy

$$\frac{\partial e}{\partial t} = -\nabla \cdot \left[\frac{\vec{I}}{\rho}(e + p) - e\vec{u_g} - \frac{\vec{I}}{\rho} \cdot \overline{\sigma}\right] + \vec{g} \cdot \vec{I} + Q_{rad} \qquad (2.1.16)$$

The viscous stress tensor for polar coordinates in two dimensions reads

$$\overline{\sigma} = \eta \begin{pmatrix} \frac{4}{3}\left(\frac{\partial u_r}{\partial r} + \frac{u_r}{r}\right) - \frac{2}{3}\frac{1}{r}\frac{\partial u_\varphi}{\partial \varphi} & \frac{\partial u_\varphi}{\partial r} + \frac{u_\varphi}{r} + \frac{1}{r}\frac{\partial u_r}{\partial \varphi} \\ \frac{\partial u_\varphi}{\partial r} + \frac{u_\varphi}{r} + \frac{1}{r}\frac{\partial u_r}{\partial \varphi} & -\frac{2}{3}\left(\frac{\partial u_r}{\partial r} + \frac{u_r}{r}\right) + \frac{4}{3}\frac{1}{r}\frac{\partial u_\varphi}{\partial \varphi} \end{pmatrix} \qquad (2.1.17)$$

The gravity is determined as

$$\vec{g} = \left(\frac{m_{tot} \cdot G}{r^2}, 0, 0\right)^T \qquad (2.1.18)$$

---

[2]For the meaning of $\nabla\cdot$and ∇ in spherical polar Coordinates see Appendix A

G	$= 6.673 \cdot 10^{-8} cm^3/g/s^2$	gravitational constant
c	$= 2.998 \cdot 10^{10} cm/s$	speed of light in vacuum
h	$= 6.626 \cdot 10^{-27} erg\ s$	Planck's constant
k	$= 1.381 \cdot 10^{-16} erg/K$	Boltzmann's constant
σ	$= 5.670 \cdot 10^{-5} erg/s/cm^2/K^4$	Stefan-Boltzmann constant
R_{gas}	$= 8.314472 \cdot 10^7 erg/K/mol$	universal gas constant
π	$= 3.1415927$	
$M_\odot$	$= 1.98892 \cdot 10^{10}$	Mass of the Sun

Table 2.1:   unities and values of used constants

the values of all the constants and quantities are in the cgs system

2.2   Radiative Transfer

To obtain a realistic simulation near the surface, nontrivial energy exchange between gas and radiation must be included by the radiative transport equation (RTE). It can be described by the radiative heating rate Q_{rad}, an additive term in the energy equation. For regions deeper down the Diffusion Approximation $Q_{rad} = -\nabla \cdot (\kappa \nabla T)$ can be used. Since we assume LTE (see section 2.2.2) the effects of scattering are not included.

2.2.1   Intensity and Flux

The specific Intensity I_v at any specific position $\vec{r}$ travelling in direction $\vec{n}$ with frequency ν at time t is defined in [Mih 1978] such that the amount of energy transported by radiation of frequencies $(\nu, \nu + d\nu)$ across an element of area dS into a solid angle $d\omega$ in a time interval dt is

$$dE_{rad} = I(\tilde{r}, \tilde{n}, \nu, t)dS \cos\theta\, d\omega\, d\nu\, dt \qquad (2.2.1)$$

where θ is the angle between the direction of the beam and the normal to the surface (i.e $dS\cos\theta = \vec{n} \cdot \vec{dS}$); see Figure 2.2.1 on page 31. The dimensions of I are $ergs\, cm^{-2}\, sec^{-1}\, hz^{-1}\, sr^{-1}$. As it has just be defined, the specific intensity provides a complete description of the radiation field from a macroscopic point of view.

Along a single ray we need only consider the one-dimensional problem. In spherical geometry the atmosphere will be regarded as *spherical symmetric*. Thus the specific intensity will be independent of the coordinates Θ and Φ of the triplet (r, Θ, Φ) which specifies the location in the atmosphere. To specify direction of the radiation $\vec{n}$ it is convenient to introduce polar and azimuthal angles (θ, ϕ) now measured with respect to a unit vector $\underline{r}$ in radial direction; we then have $\vec{n} \cdot \vec{k} = \cos\theta$, $\vec{n} \cdot \vec{i} = \sin\theta\cos\phi$, $\vec{n} \cdot \vec{j} = \sin\theta\sin\phi$. Spherical symmetry implies azimuthal invariance, therefore the azimuthal angle ϕ of the pair (θ, ϕ) which specifies the direction of the beam relative to the local outward normal

can be dropped and we can now write $I = I(r, \theta, \nu, t)$. The variable θ can be replaced with $\mu \equiv \cos\theta$.
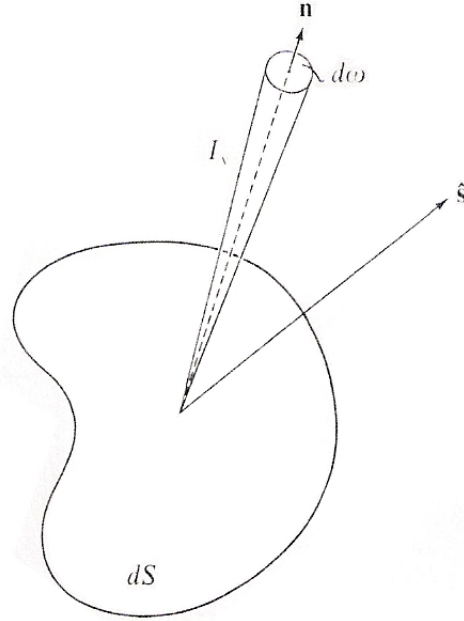

Figure 2.2.1:   pencil of radiation used to define specific intensity

The mean intensity. In both the physical and the mathematical description of a radiation field it is useful to employ various angular averages or *moments*. If the intensity field is known the mean intensity (zero-order moment) is determined as

$$J(\vec{r}, \nu, t) = \frac{1}{4\pi} \int I(\vec{r}, \vec{n}, \nu, t)\, d\omega \tag{2.2.2}$$

The mean intensity has dimensions $ergs\, cm^{-2}\, sec^{-1}\, hz^{-1}$. The element of solid angle $d\omega$ is given by $d\omega = \sin\theta d\theta d\phi = -d\mu d\phi$. If we consider one-dimensional atmospheres I is independent of ϕ, hence

$$J(r, \nu, t) = \frac{1}{4\pi} \int_0^{2\pi} d\phi \int_{-1}^1 d\mu I(r, \mu, \nu, t) = \frac{1}{2} \int_{-1}^1 d\mu I(r, \mu, \nu, t) \tag{2.2.3}$$

The radiative flux. We define the flux of radiation $\vec{F}(\vec{r}, \nu, t)$ as a vector quantity such that $\vec{F} \cdot \vec{dS}$ gives the net rate of radiant energy flow across an the arbitrarily oriented surface $\vec{dS}$ per unit time and frequency interval. Noting that $\vec{n} \cdot \vec{dS} = dS\cos\theta$, where θ is the angle between the direction of propagation $\vec{n}$ and the normal to $\vec{dS}$, we immediately recognise that the flux can be derived from the specific intensity via equation (2.2.1) for dE_{rad} is nothing more than the contribution of the pencil of radiation moving in direction $\vec{n}$ to the net energy flux. Thus we merely sum over all solid angles and obtain

$$\vec{F}(\vec{r}, \nu, t) = \oint I(\vec{r}, \vec{n}, \nu, t) \cdot \vec{n} d\omega \tag{2.2.4}$$

The flux has dimensions $ergs\,cm^{-2}\,sec^{-1}\,hz^{-1}sr^{-1}$. Note that is the first moment of the radiation field with respect to angle. In a homogeneous spherical atmosphere only the radial component of $\vec{F}$ can be nonzero, that component is often referred to as "the flux" and can be written as

$$F\left(r, \nu, t\right) = 2\pi \int_{-1}^{1} I\left(r, \mu, \nu, t\right) \mu d\mu \qquad (2.2.5)$$

2.2.2   Local Thermodynamic Equilibrium (LTE)

„Thermodynamic equilibrium prevails when a single value T of the temperature is sufficient to describe the thermodynamic state everywhere. The particles then have Maxwellian velocity distributions for that T, the states of ionisation and excitation of the atoms are distributed according to the Boltzmann and Saha equation for that same T, and the radiation field has the homogeneous and isotropic black-body form given by the Kirchhoff-Planck function for this T, namely

$$B_\nu\left(T\right) = \frac{2h\nu^3}{c^2} \frac{1}{\exp(h\nu/kT) - 1} \qquad (2.2.6)$$

No temperature gradient exists in thermodynamic equilibrium. It is obvious that this situation is realised virtually nowhere." ([Sti 2002])

„*Local* thermodynamic equilibrium means that at a certain place a single temperature T does not suffice to describe the statistical particle velocities, the population of the atomic states, and the local ratio of emission or absorption of radiation. In LTE the most important simplification of the radiative transfer problem is $S_\nu = B_\nu\left(T\right)$." ([Sti 2002]) (Scattering is not considered here.)

„Whether or not LTE can be assumed depends on the thermalisation length. This is the distance over which a particle or photon emitted in a certain collision or transition has undergone sufficient further collisions or absorption/emission processes so that it can no longer be distinguished within the respective distribution. In LTE the thermalisation length must be shorter than the distance over which the temperature of the gas changes markedly." "([Sti 2002])

„Significant departures from LTE must be expected in the upper photosphere, especially in strong lines where scattering dominates over thermal emission and disturbs the detailed energy balance of LTE. This effect can be neglected as long as these lines do not contribute significantly to the total radiative heating rate Q_{rad}." ([Vög 2003])

As is customary and largely appropriate in our context, we assume LTE.

2.2.3 The Radiative Transfer Equation

In order to determine Q_{rad} we start with the time- and frequency-dependent radiative transfer equation

$$\left(\frac{1}{c}\frac{\partial}{\partial t} + \mathbf{r} \cdot \nabla\right) I_\nu = \rho \chi_\nu \left(S_\nu - I_\nu\right) \tag{2.2.7}$$

where S_ν is the source function, an χ_ν is the opacity of the material.

Since the time a photon needs to travel through the photosphere is much shorter than any other relevant time scale and we consider only regions of relative high density the radiation field can be assumed to adjust instantaneously to any change of the thermodynamical state of the gas. Therefore we can neglect the time derivative in equation (2.2.7) and we obtain the time-independent radiative transfer equation (RTE)

$$\left(\mathbf{r} \cdot \nabla\right) I_\nu = \rho \chi_\nu \left(S_\nu - I_\nu\right) \tag{2.2.8}$$

Instead of solving the three-dimensional RTE the one-dimensional RTE is solved along several ray-directions. In one dimension and spherical coordinates equation (2.2.8) simplifies to

$$\mu \frac{\partial I_\nu}{\partial r} + \frac{1}{r}\left(1 - \mu^2\right)\frac{\partial I_\nu}{\partial \mu} = \rho \chi_\nu \left(S_\nu - I_\nu\right) \tag{2.2.9}$$

This partial differential equation in r and μ can be simplified by using the characteristic paths that reduce the spatial operator to a single derivative with respect to path-length again called r

$$\mu \frac{\partial I_\nu}{\partial r} = \rho \chi_\nu \left(S_\nu - I_\nu\right) \tag{2.2.10}$$

Introducing the optical depth of an element at frequency ν as the independent coordinate

$$d\tau_\nu = \chi_\nu \rho dr \tag{2.2.11}$$

the RTE can be rewritten as

$$\mu \frac{\partial I_\nu}{\partial \tau_\nu} = S_\nu - I_\nu \tag{2.2.12}$$

The formal solution. For given S equation (2.2.12) is a linear first order differential equation with constant coefficients and must therefore have an integrating factor, namely

$$\partial \left[I_\nu e^{-\tau_\nu/\mu}\right]/\partial \tau_\nu = -\frac{1}{\mu} S_\nu e^{-\tau_\nu/\mu} \tag{2.2.13}$$

Integration of equation (2.2.13) yields

$$I\left(\tau_1, \mu, \nu\right) = I\left(\tau_2, \mu, \nu\right) e^{(\tau_2 - \tau_1)/\mu} + \frac{1}{\mu}\int_{\tau_1}^{\tau_2} S_\nu\left(t\right) e^{-(t-\tau_1)/\mu} dt \tag{2.2.14}$$

If the value $I\left(\tau_2, \mu, \nu\right)$ and the values of $S_\nu\left(t\right)$ along the ray are known between the optical depths τ_2 and τ_1 the value $I\left(\tau_1, \mu, \nu\right)$ can be determined.

The radiative heating rate can be computed either as

$$Q_{rad} = 4\pi \int_\nu \chi_\nu \left(J_\nu - S_\nu\right) d\nu \qquad (2.2.15)$$

or from the equivalent expression

$$Q_{rad} = - \int_\nu \left(\nabla \cdot F_\nu\right) d\nu \qquad (2.2.16)$$

2.3   The Equation of State

The equation of state completes the equations for radiation hydrodynamics (2.1.13), (2.1.14), (2.1.16) and (2.2.15) and describes the relations between thermodynamical quantities. It depends on the physical properties of the gas under study especially on the content of hydrogen, helium and „metals". It also depends on the degree of ionisation; therefore in the convection zones the simple thermodynamical relations for an ideal gas cannot be used.

For realistic microphysics the OPAL [RSI 1996] equation of state and opacities are included, for the RTE the Alexander low-temperature Rosseland opacities for grey radiative transfer [AF 1994] are used.

Chapter 3

Implementation in the ANTARES Code

The ANTARES (Advanced Numerical Tool for Astrophysical RESearch) code as used for these simulations performs various compressible simulations on differently structured grids. Though not everything is possible for every case. All is comprised in one parallelized Fortran90 program which can be broken up into separate modules to deal with specific cases.

Tasks within this PhD project were

- Implementing a stretched grid. Determining and implementing of the appropriate coefficients for derivatives, interpolation stencils and all the weights and coefficients used in the ENO.

- Implementing a moving, polar grid. Adjusting the radiative transfer solver and the update process to this grid.

- Development and discretisation of appropriate boundary conditions.

- Developing adaptive grid refinement and testing the effects thereof.

The differential equations solved by the ANTARES code can also be written as a system of conservation laws of the form

$$\partial_t U = -\nabla \cdot F\left(U\right) + S \tag{3.0.1}$$

A discretisation of the physical domain results in a centre grid r_i and a boundary grid $r_{i+\frac{1}{2}}$, where the function $F_i\left(U\right)$, also known as "the fluxes", is computed at the cell centre; $\widetilde{F}_{i+\frac{1}{2}}\left(U\right)$ are the fluxes interpolated to the cell boundaries. The viscosities are also included in this function $F_i\left(U\right)$. (Section 3.6)

3.1   The Initial Condition

log Density

log Temperature
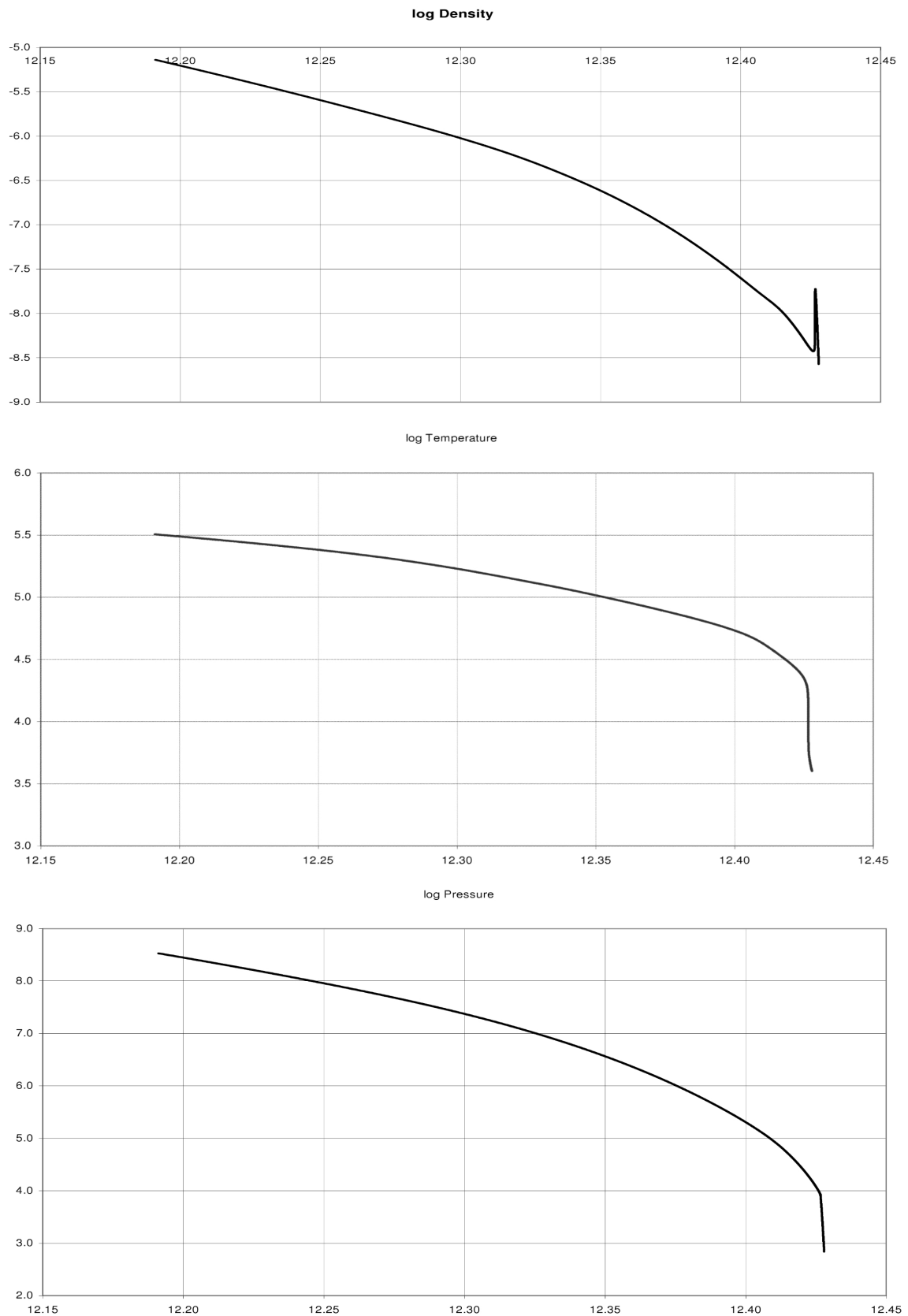
log Pressure

Figure 3.1.1:   initial Conditions of density, temperature and pressure

Abscissa: Log(radius)

We start with a one-dimensional model kindly provided by Günter Houdek[1] of a Cepheid of effective temperature 5125K, luminosity $L = 912.797L_{\odot}$, mass $M = 5M_{\odot}$, hydrogen contents $X = 0.7$, metallicity $Z = 0.01$ as depicted in figure 3.1.1.[2]

The computational domain reaches from 4000K to 320000K, thus the outer 42% of the star are computed.

We start with a one-dimensional purely radiative model. In order to help the pulsations starting the gravity is reduced by 1% for the first few steps. To ensure that this star is indeed a pulsator and pulsates in the fundamental mode as indicated for example in [FBK 2000] (Figure 3.1.3 on page 38) a Fourier analysis of the radius is done.
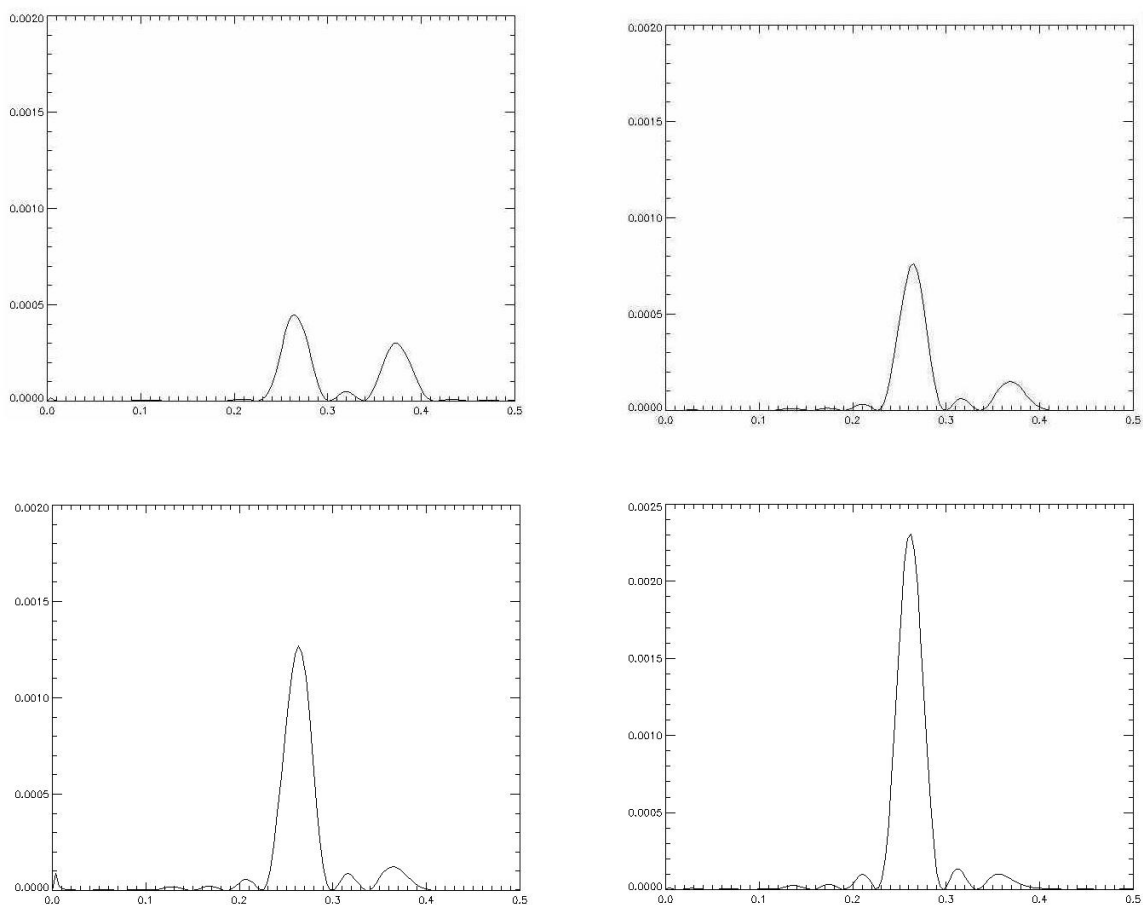

Figure 3.1.2:   Fourier analysis of the radial pulsation

Abscissa: frequency in 1/days, ordinate: radius squared. For (a) the first ten sound crossing times were taken into account, (b) used sound crossing times 50 to 60, (c) 100 to 110 and (d) 150 to 160. The first hump corresponds to the fundamental mode the second to the first overtone.

After pulsation becomes stable and stays so for a considerable time the one-dimensional

---

[1]Institute of Astronomy, Vienna University
[2]higher metallicity gives a better resolution of Q_{rad}.

model is converted into a two-dimensional one by setting the one-dimensional model side by side. The new lateral momentum is slightly perturbed in a random fashion.
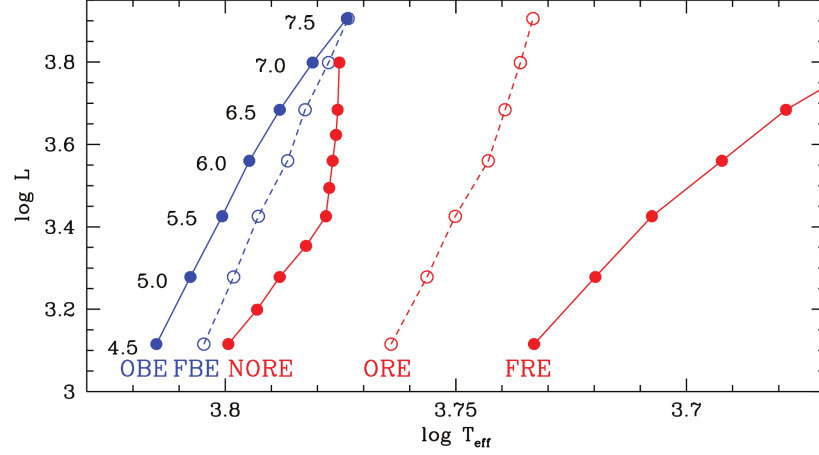

Figure 3.1.3:   instability strip boundaries for convective models (from [FBK 2000])

in the Log L - Log Teff plane. From left to right: (first) overtone linear blue edge (OBE), fundamental linear blue edge (FBE), nonlinear overtone red edge (NORE), overtone linear red edge (ORE) and fundamental linear red edge (FRE); the labels on left refer to the stellar masses.

3.2   The Grid Structure

The computational domain is equipped with a polar grid.

In radial direction $N_x = 510$ grid points plus 4 ghost cells at each boundary are used. The r-range covers $r \in [r_{top}, r_{bot}]$, where r_{bot} is fixed and r_{top} varies with time. The grid is stretched in radial direction by a factor q. The mesh sizes are $\Delta r_{i+1} = q\Delta r_i$ varying from $\Delta r_0 = 0.046 Mm$ at the top to $\Delta r_{N_x-1} = 12 Mm$ at the bottom. Thus the numerical grid becomes

$$r_i = r_{bot} + \frac{q^i - 1}{q^{N_x} - 1} \left(r_{top} - r_{bot} \right) \tag{3.2.1}$$

Cell boundary values are defined as $r_{i+\frac{1}{2}} = r_i - \frac{\Delta r_i}{1+\sqrt{q}}$ and $r_{i-\frac{1}{2}} = r_i + \frac{\sqrt{q}\Delta r_{i-1}}{1+\sqrt{q}}$, cell heights as $\Delta r_{i+\frac{1}{2}} = \sqrt{q}\Delta r_i$.

In angular direction the angle φ-range covers $\varphi \in \left[-\frac{\varphi_{tot}}{2}, +\frac{\varphi_{tot}}{2} \right]$, the mesh size is $\Delta\varphi = \frac{\varphi_{tot}}{N_y}$. The numerical grid is given by

$$\varphi_j = j\Delta\varphi - \frac{\varphi_{tot}}{2} \tag{3.2.2}$$

Cell boundary values are defined as $\varphi_{j\pm\frac{1}{2}} = \varphi_j \pm \frac{\Delta\varphi}{2}$.
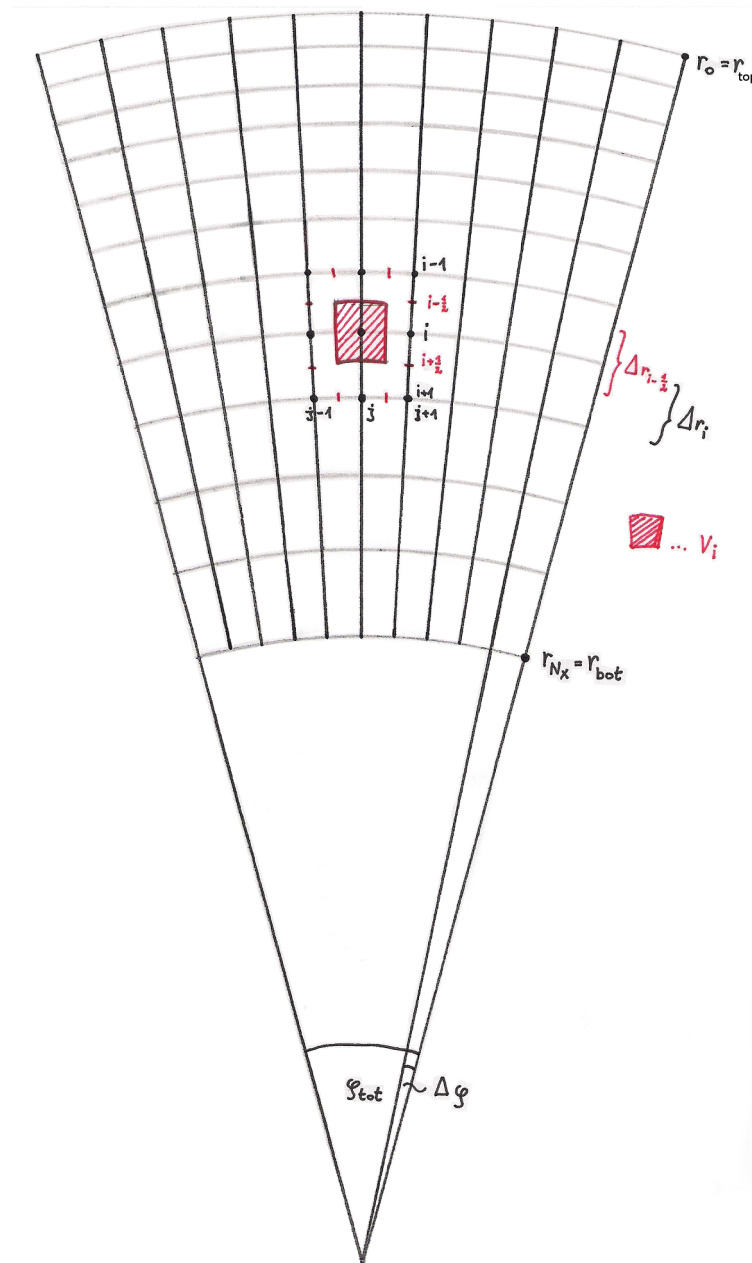
Figure 3.2.1:   polar grid

The physical distance between two adjacent points in lateral direction is computed as $\Delta y_i = r_i \Delta \varphi$.

Cell volumes or either computed as

$$V_i = \frac{2}{3} \left(r_{i-\frac{1}{2}}^3 - r_{i+\frac{1}{2}}^3 \right) \Delta \varphi \qquad (3.2.3)$$

or approximated by[3]

$$\widetilde{V}_i = 2 r_i^2 \Delta r_{i-\frac{1}{2}} \Delta \varphi \qquad (3.2.4)$$

---

[3]In 1D: $\Delta \varphi = 2\pi$

For each cell the surface is given by $A_{i\pm\frac{1}{2}} = 2r^2_{i\pm\frac{1}{2}}\Delta\varphi$ at the top and at the bottom. At the sides it is exactly

$$B_i = \frac{\pi}{2}\left(r^2_{i-\frac{1}{2}} - r^2_{i+\frac{1}{2}}\right) \tag{3.2.5}$$

or approximately

$$\widetilde{B}_i = \pi r_i \Delta r_{i-\frac{1}{2}} \tag{3.2.6}$$

3.3   Time Stepping and Time Step Restrictions

The largest possible time step is determined by the CFL-condition. In each time step and in every cell the distance that the information is transported by flow velocities must be shorter than the mesh width. Therefore we get a time step restriction

$$\Delta t_{CFL} = c_{courant}\min_{i,j}\left(\frac{\min(\Delta r_i, \Delta y_i)}{|\vec{u}| + c_{sound}}\right) \tag{3.3.1}$$

where $c_{courant}$ is the Courant number and c_{sound} is the sound velocity. The minimum $\min_{i,j}$ is taken over the whole domain. For all the simulations here a Courant number of $c_{courant} = \frac{1}{4}$ is selected.

Also the diffusion velocity and the radiative timescale have to be taken into account. The time scale for relaxing a temperature perturbation of arbitrary optical thickness by radiation [Spi 1957]

$$\Delta t_{rad} = c_{courant}\min_{i,j}\left(\frac{c_p}{16\kappa\sigma T^3}\left(1 - \frac{\kappa\rho}{k}arccot\frac{\kappa\rho}{k}\right)^{-1}\right) \tag{3.3.2}$$

may become smaller than the hydrodynamical time scale. In (3.3.2) κ is the opacity, σ is the Stefan-Boltzmann constant and $k = \frac{2\pi}{\min(\Delta r_i, \Delta y_i)}$. For the optical thick case where diffusion approximation can be used Δt_{rad} converges to the time scale of radiative diffusion

$$\Delta t_{diffusive} = c_{courant}\min_{i,j}\left(\frac{c_p}{16\kappa\sigma T^3}3\left(\frac{\kappa\rho}{k}\right)^2\right) \sim c_{courant}\min_{i,j}\left(\frac{min(\Delta r_i, \Delta y_i)^2}{\chi}\right) \tag{3.3.3}$$

If artificial diffusivities are used (section 3.6.3) an additional diffusive time step restriction is applied:

$$\Delta t_{artdiff} = c_{courant}\min_{i,j}\left(\frac{\min(\Delta r_i, \Delta y_i)}{\nu_i}\right) \tag{3.3.4}$$

The denominator consists of all the artificial diffusivities $\nu = \nu^{shk} + \nu^{hyp}$.

The time step used is either

$$\Delta t = \min\left(\Delta t_{CFL}, \Delta t_{rad}\right) \tag{3.3.5}$$

or if artificial diffusivities are used

$$\Delta t = \min\left(\Delta t_{CFL}, \Delta t_{rad}, \Delta t_{artdiff}\right) \tag{3.3.6}$$

In practise all our simulations were limited by the radiative time step.

If grid refinement is used Δt is determined for each grid separately, the number of steps during the grid refinement process is given by $int\left(\frac{\Delta t_{coarse}}{\Delta t_{fine}}\right)$. One of the advantages of adaptive grid refinement is a smaller number of grid refinement steps, since it helps to stay out of the optical thick realm, where $\Delta t_{fine} = \Delta t_{coarse}^2$.

3.4 Boundary Conditions
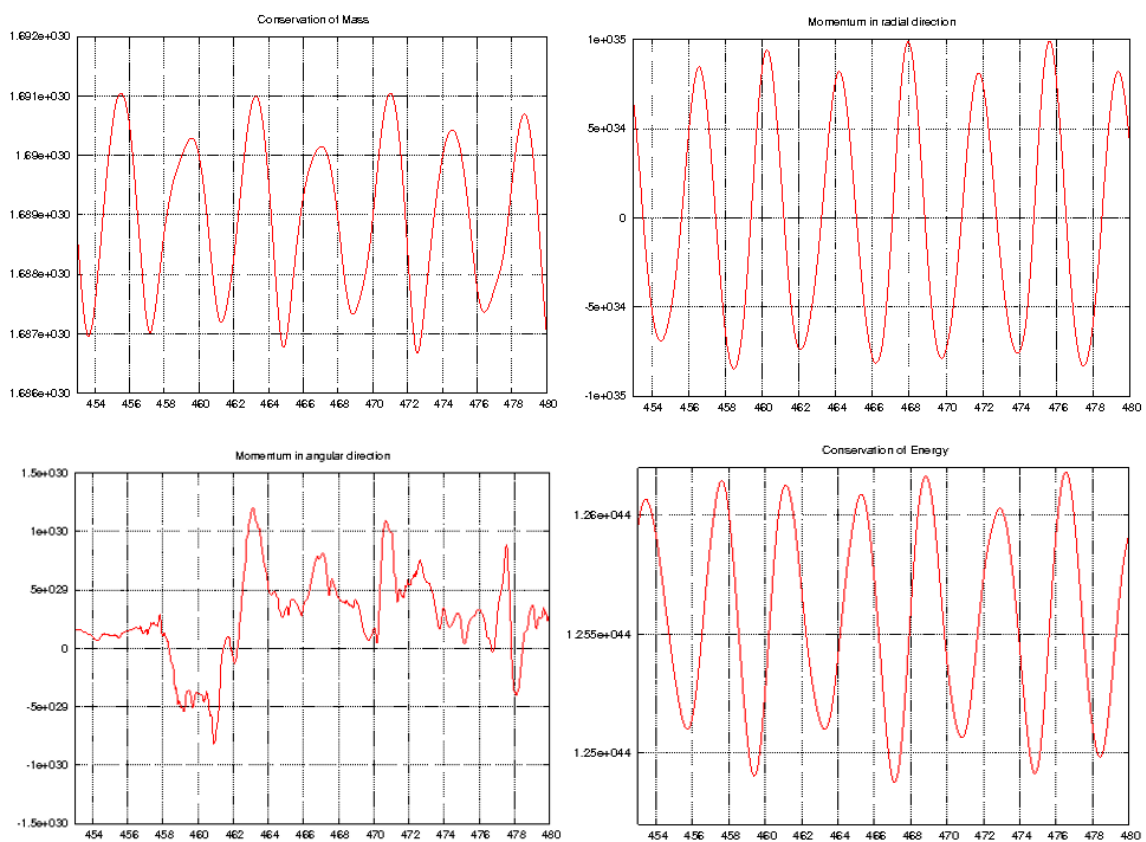
Figure 3.4.1:   conservation laws

2D simulation, abscissa: days

In horizontal direction all quantities are assumed to be periodic.

Boundary condition on the grid: The grid is fixed at the bottom thus the grid velocity vanishes, at the top it is determined as the horizontal average of the fluid velocity in radial direction.

$$u_g|_{top} = \overline{u_r}|_{top}$$
$$u_g|_{bot} = 0$$

For closed boundary conditions the vertical flux of mass, angular momentum and energy (except radiative energy) are set to zero, this is achieved by:

$$
\begin{aligned}
\frac{\partial \rho}{\partial r}\Big|_{top} &= 0 \\
u_r|_{top} &= u_g|_{top} \\
\frac{\partial u_\varphi}{\partial r}\Big|_{top} &= 0 \\
\frac{\partial T}{\partial r}\Big|_{top} &= 0
\end{aligned}
$$

at the top, and

$$
u_r|_{bot} = 0
$$

at the bottom. Since the star is purely radiative at the bottom the incoming energy transport is adjusted by keeping the radial component of radiative flux density $\kappa \nabla T$ at its initial value.

Note that here are no boundary conditions on density and no boundary condition on angular momentum at the bottom.

At the top the conditions for the velocities are set on 3 points and for temperature on 2 points, at the bottom one point is used for radial velocity and two for radiative flux.

Conservation of mass, momentum and energy are not violated by this boundary conditions over time:

3.5 Evolving in Time

The physical state $\vec{q}^{\,n+1} = \left(\rho, \vec{I}, e\right)^{n+1}$ at time step $n+1$ is computed from the physical state $\vec{q}^{\,n} = \left(\rho, \vec{I}, e\right)^n$ at time step n by a Runge Kutta scheme [SO 1988], either of second or third order[4]. By temporal discretisation the ordinary differential equation $q_t = L(q)$ becomes $\frac{q^{n+1} - q^n}{\Delta t} = L(q)$ where the vector $L(q)$ contains the spatial derivatives and source terms.

Using a second order Runge-Kutta scheme two time steps are necessary to calculate the state at time :

$$
\begin{aligned}
q_0 &= q^n \\
q_1 &= q_0 + \Delta t L(q_0) \\
q_2 &= \frac{1}{2}\left(q_0 + q_1 + \Delta t L(q_1)\right) \\
q^{n+1} &= q_2
\end{aligned}
\qquad (3.5.1)
$$

---

[4]In fact for all simulation second order was sufficient.

For the third order scheme three steps are used:

$$
\begin{aligned}
q_0 &= q^n \\
q_1 &= q_0 + \Delta t L(q_0) \\
q_2 &= \frac{1}{4}\left(3q_0 + q_1 + \Delta t L(q_1)\right) \\
q_3 &= \frac{1}{3}\left(q_0 + 2q_2 + 2\Delta t L(q_2)\right) \\
q^{n+1} &= q_3
\end{aligned}
\tag{3.5.2}
$$

At the beginning of each time step q^n the value of Δt is computed, and if grid refinement is done, the number of grid refinement steps are computed as well.

Each of the intermediate states is calculated by the following algorithm:

- Start with a physical state given as cell averages, grid velocity and coordinates.

- Computing the inviscid central fluxes according to the differential equation

- Interpolate these fluxes to cell boundary fluxes in all directions using a one-dimensional WENO-scheme (section 6.8)

- Calculate the viscous central fluxes and interpolate to cell boundary fluxes by fourth order interpolation (section 6.6).

- The radiative heating rate is computed by solving the radiative transfer equation (section 6.7).

- For the update process cell volumes and the sizes of the surface at time $n + 1$ are computed. The new values of the conserved variables are determined (section 6.9).

- The grid is updated by moving the grid coordinates with grid velocity $\vec{u}_g^n$. Actually only the outermost point is moved with grid velocity, all the other points are computed to satisfy equation (3.2.1).

- Call the equation of state to get the other used quantities. Compute remaining grid variables and gravity.

- Grid velocity $\vec{u}_g^{n+1}$is determined. The velocity at the top is determined as the horizontal average of the fluid at the top, at the bottom $\vec{u}_g^{n+1} \equiv 0$. From this a dilation factor d_{fac} and the grid velocity elsewhere are computed.

- Hydrodynamic boundary conditions are applied (section 6.4).

After the whole Runge-Kutta step is complete grid refinement can be done. In order to do this the boundary of the grid refinement zone, the grid velocity and the radial coordinates[5]

---

[5]Since the patch moves with the grid indices, note that $r_{bot}$is not fixed here.

are projected from the coarse grid to the fine one. The required number of steps is done in precisely the same way as for the coarse grid, with the exemption that the boundary conditions are replaced by projections from the coarse grid.

3.6   Spatial Interpolation of Viscous Fluxes

3.6.1   Interpolation and Derivatives

For an equidistant grid and a stretched grid the following interpolation methods can be used within the ANTARES code in order to find the boundary values for the viscous fluxes and their like. Here I present the formulae for the stretched grid as used in radial direction.[6]

1. second order

$$f_{i+\frac{1}{2}} = \frac{q^{0.5}f_i + f_{i+1}}{q^{0.5}+1}$$

2. 4th order

$$
\begin{aligned}
f_{i+\frac{1}{2}} = \ & -\frac{q^4}{q^{3.5}+2q^3+2q^{2.5}+3q^2+3q^{1.5}+2q+2q^{0.5}+1}f_{i-1} + \\
& +\frac{q^3+2q^{2.5}+3q^2+2q^{1.5}+q}{q^{2.5}+3q^2+4q^{1.5}+4q+3q^{0.5}+1}f_i + \\
& +\frac{q^2+2q^{1.5}+3q+2q^{0.5}+1}{q^{2.5}+3q^2+4q^{1.5}+4q+3q^{0.5}+1}f_{i+1} - \\
& -\frac{1}{q^{3.5}+2q^3+2q^{2.5}+3q^2+3q^{1.5}+2q+2q^{0.5}+1}f_{i+2}
\end{aligned}
$$

Spatial Derivatives within the viscous fluxes

For the viscous stress tensor as well as for the temperature gradient used for the diffusion approximation derivatives are taken at the cell centre. The numerical approximation of these derivatives is:

1. second order

$$\frac{1}{r_{i+1}-r_i}\left(-\frac{q^2}{q+1}u_{i-1} + (q-1)\,u_i + \frac{1}{q+1}u_{i+1}\right)$$

2. 4th order

$$
\begin{aligned}
\frac{1}{r_{i+1}-r_i}\ \Bigg(& \frac{q^7}{(q^2+q+1)(q^3+q^2+q+1)}u_{i-2} && -\frac{q^3(q+1)}{q^2+q+1}u_{i-1} + \\
& +2\,(q-1)\,u_i && +\frac{q+1}{q(q^2+q+1)}u_{i+1} - \\
& && -\frac{1}{q(q^2+q+1)(q^3+q^2+q+1)}u_{i+2}\Bigg)
\end{aligned}
$$

For these simulations the 4th order methods were used. At the upper and lower physical boundary the asymmetric stencils of the same order are used.

---

[6]For the equidistant case used in lateral direction see [Obe 2007] or set $q = 1$.

3.6.2   Subgrid-scale Modelling

The most widely used models are based on the work of Smagorinsky (1963) and Lilly (1962). The subgrid-scale stress is written as[7]

$$\tau_{ij}^a = \tau_{ij} - \frac{1}{3}\delta_{ij}\tau_{kk} = -2\rho K_m \tilde{D}_{ij} \tag{3.6.1}$$

where $\tilde{D}_{ij}$ is the strain rate tensor:

$$\tilde{D}_{ij} = \frac{1}{2}\left(\frac{\partial \tilde{u}_i}{\partial x_j} + \frac{\partial \tilde{u}_j}{\partial x_i}\right) - \frac{1}{3}\delta_{ij}\frac{\partial \tilde{u}_k}{\partial x_k} \tag{3.6.2}$$

The eddy viscosity K_m is given by

$$K_m = C\Delta^2 \left|\tilde{D}\right| \tag{3.6.3}$$

where Δ is the filter width, approximated here as $(\Delta r_i \Delta y_i)^{1/2}$, and as $(\Delta r_i \Delta y_i \Delta z_i)^{1/3}$ in three dimensions, and C is a dimensionless coefficient. This coefficient is a constant parameter often written as the Smagorinsky coefficient $c_s = C^{1/2}$.

3.6.3   Artificial Diffusivities

Artificial diffusivities [SN 1998] are intended to remove short-wavelength noise without damping longer wavelengths and diffuse strong discontinuities in order to stabilise the numerical code.

The viscous stress tensor

$$\underline{\tau}_{kl} = \mu\left(\frac{\partial u_k}{\partial x_l} + \frac{\partial u_l}{\partial x_k} - \frac{2}{3}\delta_{kl}\left(\nabla \cdot \vec{u}\right)\right) \tag{3.6.4}$$

is replaced by artificial equivalents of the form

$$\underline{\tau}_{kl} = \frac{1}{2}\rho\left(\nu_k\left(u_l\right)\frac{\partial u_k}{\partial x_l} + \nu_l\left(u_k\right)\frac{\partial u_l}{\partial x_k}\right) \tag{3.6.5}$$

where $u = (u_1, u_2, u_3)^T$ and $k, l = $ 1,2,3 .

The coefficients ν_k for direction k consists of two parts, a shock resolving part ν_k^{shk} and a hyper-diffusive part ν_k^{hyp}:

$$\nu_k\left(u_l\right) = \nu_k^{shk} + \nu_k^{hyp}\left(u_l\right) \tag{3.6.6}$$

The shock resolving part in direction k is defined by

$$\nu_k^{shk} = \begin{cases} C_{shk}\Delta x_k^2 \left|\nabla \cdot \vec{u}\right| & \nabla \cdot \vec{u} < 0 \\ 0 & \nabla \cdot \vec{u} \geq 0 \end{cases} \tag{3.6.7}$$

---

[7]The superscript a denotes the anisotropic part of a tensor.

which is only applied in regions undergoing compression, i.e. where $\nabla \cdot \vec{u} < 0$. The Hyper-diffusive part in direction k is defined by

$$\nu_k^{hyp}(f) = C_{hyp}\Delta x_i c_{tot} \frac{\max_3 \left|\Delta_k^3 f\right|}{\max_3 \left|\Delta_k^1 f\right|} \tag{3.6.8}$$

where $c_{tot} = \|\vec{u}\| + c_{sound}$ and

$$
\begin{aligned}
\left(\Delta_k^3 f\right)_i &= \left|3\left(u_{i+1} - u_i\right) - \left(u_{i+2} - u_{i-1}\right)\right| \\
\left(\Delta_k^1 f\right)_i &= \left|u_{i+1} - u_i\right|
\end{aligned}
$$

For each grid point the index i runs in direction k. Artificial diffusivities were used only in a few tests for the simulations presented in Chapter 4.

3.7 Numerical Implementation of Radiative Transfer

Instead of solving the three dimensional RTE (2.2.8) the one-dimensional RTE (2.2.9) with $r = 1$ is solved along several directions, to this end the short characteristic method [KA 1988] is used.[8]

3.7.1 Boundary Conditions

In horizontal directions all quantities are assumed to be periodic.

Since radiation comes from within the star and not from the outside there is no incoming radiation, i.e. $I_{rad}|_{top} = 0$ for all entering rays.

At the bottom of the computational domain the diffusion approximation $I_\nu|_{bot} = B_\nu$ is valid. The diffusion approximation holds for optical depths greater than about ten. The lower boundary condition can be either applied at a certain optical depth τ_{bot} or at a fixed percentage of the domain. τ_{bot} is calculated with the Rosseland mean opacity and in the region below that border the radiative heating rate Q_{rad} is calculated according to the diffusion approximation $Q_{rad} = \nabla \cdot (\kappa \nabla T)$.

3.7.2 Numerical Scheme

Since grey radiative transfer is used the Planck function is $S = B(T) = \frac{\sigma}{\pi}T^4$.

At grid point P the intensity along a certain ray can be determined if the intensity in the layer where the short ray originates is known as it is at the upper and lower boundaries.

At the sides the intensity from the previous time step is used for the periodic boundary condition.

---

[8]It is more efficient and accurate than the long characteristic method [Obe 2007]

Overview:

1. N_{rays} ray directions are specified at each grid point $x_{i,j}$.

2. The rays are classified according to the four corners of the surrounding box.

3. For each ray the points of entrance and exit plus the corresponding distances are determined. Since the grid moves, this has to be done every step, even point wise prestoring is impossible.

4. The RTE is solved along each ray.

5. The mean intensity is computed by solid angle integration

6. The radiative heating rate is determined.

ad 1 - ray directions:
Two different approaches are implemented in the ANTARES-code.

The simple method for N_{rays} rays in two dimensions is to choose evenly spaced angles and set he components of r^i to $\left(-\cos\frac{(2i-1)\pi}{N_{rays}}, \sin\frac{(2i-1)\pi}{N_{rays}} \right)$. Thus there is no purely horizontal or vertical ray. The number of directions along which the RTE is solved is a multiple of four. For the one-dimensional problem the projection of these vectors yields $\left(-\cos\frac{(2i-1)\pi}{N_{rays}} \right)$ where N_{rays} has to be an even number.

For three dimensional simulations the one-dimensional RTE would be solved along 24 ray directions which are chosen according to the angular quadrature formulae of type A4 and A6 of Carlson [Car 1963].

i	x_i	y_i	z_i
1	$\frac{1}{3}$	$\frac{1}{3}$	$\sqrt{\frac{7}{9}}$
2	$\frac{1}{3}$	$\sqrt{\frac{7}{9}}$	$\frac{1}{3}$
3	$\sqrt{\frac{7}{9}}$	$\frac{1}{3}$	$\frac{1}{3}$

(a) Carlson A4

i	x_i	y_i	z_i
1	$\sqrt{\frac{1}{15}}$	$\sqrt{\frac{1}{15}}$	$\sqrt{\frac{13}{15}}$
2	$\sqrt{\frac{1}{15}}$	$\sqrt{\frac{7}{15}}$	$\sqrt{\frac{7}{15}}$
3	$\sqrt{\frac{1}{15}}$	$\sqrt{\frac{13}{15}}$	$\sqrt{\frac{1}{15}}$
4	$\sqrt{\frac{7}{15}}$	$\sqrt{\frac{1}{15}}$	$\sqrt{\frac{7}{15}}$
5	$\sqrt{\frac{7}{15}}$	$\sqrt{\frac{7}{15}}$	$\sqrt{\frac{1}{15}}$
6	$\sqrt{\frac{13}{15}}$	$\sqrt{\frac{1}{15}}$	$\sqrt{\frac{1}{15}}$

(b) Carlson A6

Table 3.1: ray directions in the first octant

The directions in each octant are arranged in a triangular pattern. In two dimensions A4 reduces to 12 rays, 3 in each quadrant (Figure 3.7.1 on page 48) and in one dimension to 4 different rays.
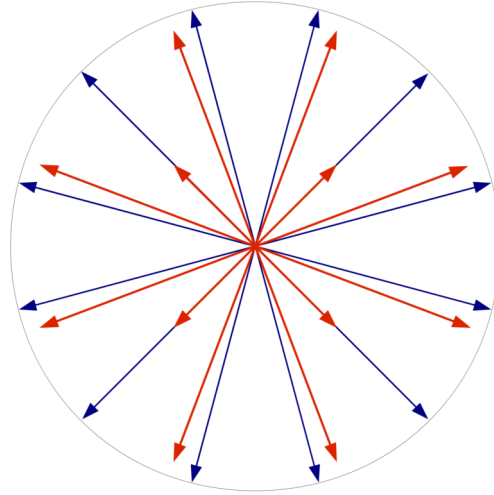

Figure 3.7.1:   ray directions in two dimensions

Blue: equidistant angles; Red: derived from the 3D case

ad 2 - ray classification:

The rays are classified according to the four corners of the surrounding box as this choice does not depend on the grid-point $x_{i,j}$ as would a classification by the surface directions.

direction	
1	Rays entering from the corner $x_{i+1,j+1}$
-1	Rays entering from the corner $x_{i-1,j-1}$
2	Rays entering from the corner $x_{i+1,j-1}$
-2	Rays entering from the corner $x_{i-1,j+1}$

Table 3.2:   ray classification

ad 3 - distances:

The entrance point U as well as the exit point Q can be located either on the surface of constant radius or of constant angle. They have to be determined separately.

ad 4 - solving the RTE:

For incoming radiation values of $I(\tau_U)$ along the ray direction r^i are known. The optical depth τ_U there is set to zero. To determine $I(\tau_U)$ along this ray direction one has to interpolate the values of the required physical quantities to the points U and Q. In two dimensions 4 points are used for all but the intensity, where 2 points have to suffice. Then one evaluates the equation

$$I(\tau_p) = I(\tau_U)\exp(\tau_u - \tau_p) + \int_{\tau_U}^{\tau_P} S(t)\exp(t - \tau_p)\,dt \qquad (3.7.1)$$

numerically to get $I(\tau_P)$. This procedure is repeated recursively since after the first step one gets just the intensity on a single new point:

Numerical Integration. To perform the numerical integration on the right hand side of (3.7.1) one has to determine τ_P and τ_Q, $\tau_U = 0$ is already known. The optical depth at point P is defined as $\tau_P = \int_U^P \rho\chi dx$ and at point Q as $\tau_Q = \int_U^Q \rho\chi dx$.

By constructing a quadratic interpolation polynomial through the three points $(U, \rho(U)\chi(U))$, $(P, \rho(P)\chi(P))$ and $(Q, \rho(Q)\chi(Q))$ and performing an exact integration of this interpolation polynomial one gets approximations for τ_P and τ_Q.
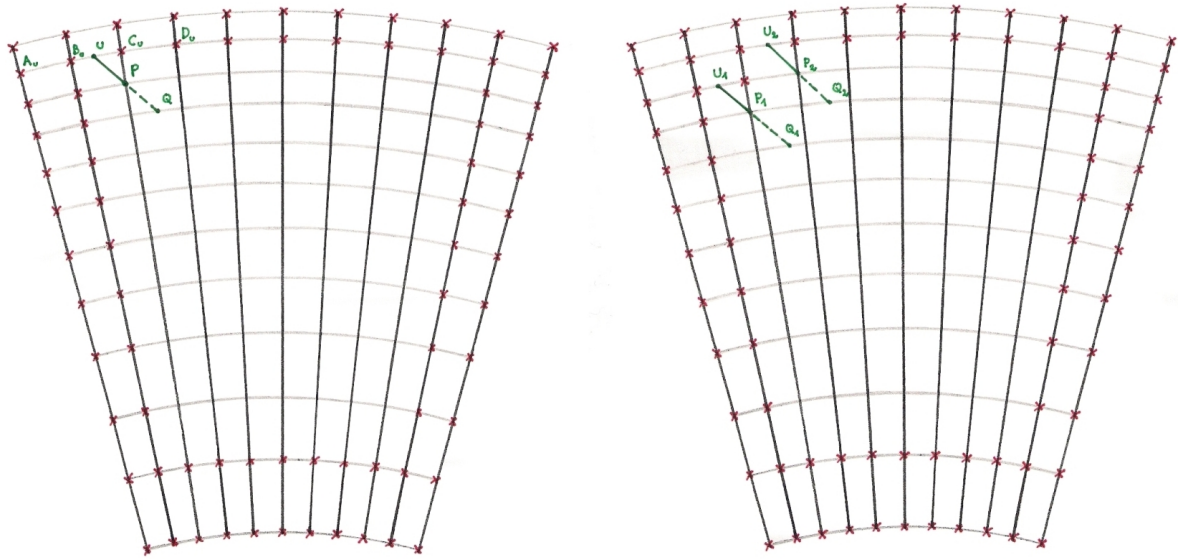

Figure 3.7.2: 1st and 2nd step of the computation of I_{rad}

for a ray in direction 1

A more stable but less accurate approximation is calculated by

$$\tau_P \approx \tfrac{1}{2}(\rho(U)\chi(U) + \rho(P)\chi(P)) \cdot \left|\vec{UP}\right|$$

$$(3.7.2)$$

$$\tau_Q \approx \tau_P + \tfrac{1}{2}(\rho(P)\chi(P) + \rho(Q)\chi(Q)) \cdot \left|\vec{PQ}\right|$$

here an integral is evaluates twice numerically by the trapezoid rule.
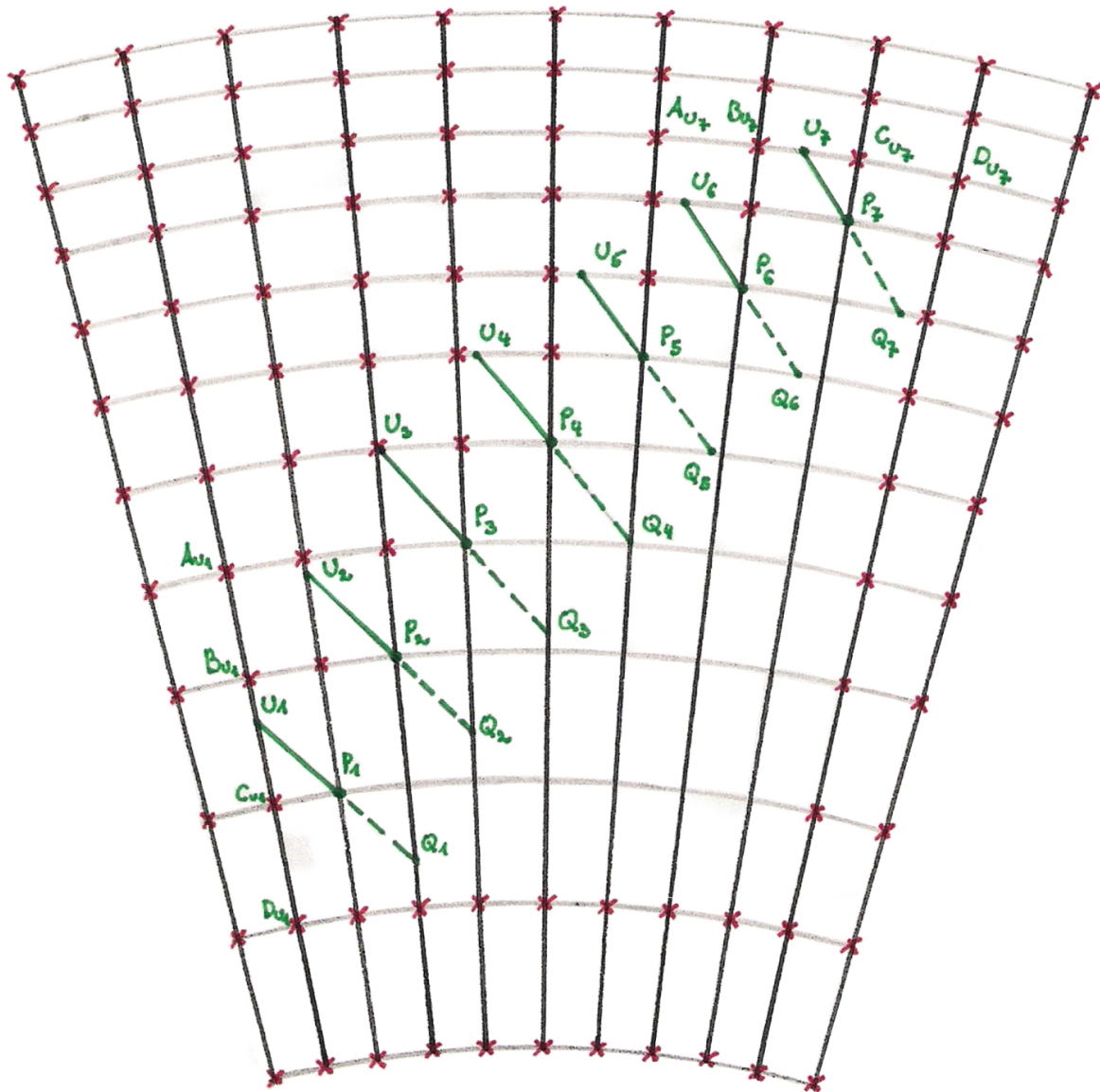

Figure 3.7.3:   8th step thereof

The integration on the right hand side of equation (3.7.1) is performed by a quadrature rule proposed by Olson and Kunasz. Let τ_1 be the optical depth along the path from U to P and let τ_2 be the optical depth along the path from P to Q. A numerical approximation to the integral $\int_{\tau_U}^{\tau_P} S(t) \exp(t - \tau_p) dt$ is given by

$$\int_{\tau_U}^{\tau_P} S(t) \exp(t - \tau_p) dt = \alpha S(U) + \beta S(P) + \gamma S(Q) \qquad (3.7.3)$$

where

$$
\begin{aligned}
e_0 &= 1 - \exp(\tau_1) \\
e_1 &= \tau_1 - e_0 \\
e_2 &= \tau_1^2 - 2e_0 \\
\alpha &= \frac{e_0 + (e_2 - (2\tau_1 + \tau_2)e_1)}{\tau_1(\tau_1 + \tau_2)} \\
\beta &= \frac{(2\tau + \tau_2)e_1 - e_2}{\tau_1\tau_2} \\
\gamma &= \frac{e_2 - \tau_1 e_1}{\tau_2(\tau_2 + \tau_1)}
\end{aligned}
$$

Interpolation. The values for the physical quantities at point U are interpolated from the neighbouring grid points. For the two-dimensional case 4 grid points $A_U = (x_{i-1}, y_{i-1})$, $B_U = (x_i, y_i)$, $C_U = (x_{i+1}, y_{i+1})$ and $D_U = (x_{i+2}, y_{i+2})$ are used for the interpolation at U; A_Q, B_Q, C_Q and D_Q are used for the interpolation at Q. For the interpolation of I only the points B_U and C_U are used.

For one-dimensional interpolation various methods are implemented in the ANTARES code, see [Obe 2007] for details.

ad 5 - mean intensity:
For every grid point the one-dimensional RTE is solved along ray directions. To get the mean intensity an integration over the solid angle is performed. The ray directions are chosen according to a Gauss-Fourier quadrature rule. Gaussian quadrature is based on making the formula

$$
\int_{-1}^{1} F(x)dx = \sum_{i=1}^{N} w_i F(x_i) \tag{3.7.4}
$$

exact for the first $2N - 1$ powers of x. An analogous quadrature formula for $\sin j\pi x$ and $\cos j\pi x$ $(j = 0, 1, 2, \dots, n-1)$ is obtained by applying the trapezoidal-type approximation

$$
\int_{-1}^{1} F(x)dx \approx \frac{2}{N} \sum_{k=1}^{N} F\left([2k - 1 - N + \alpha]/N\right), \ |\alpha| \leqq 1 \tag{3.7.5}
$$

to the function $F(x) = \exp(\pm\pi n x i)$ which leads to

$$
\int_{-1}^{1} F(x)\,dx \ \approx \ \frac{2}{N} \exp\left[\pm\frac{\pi n}{N}(1 - N + \alpha)i\right] \cdot \tag{3.7.6}
$$

$$
\cdot \sum_{k=1}^{N} \exp\left[\pm\frac{\pi n}{N}(2k - 2)i\right] \tag{3.7.7}
$$

The error in equation (3.7.6) vanishes for all integers $n \neq 0 (mod N)$ since

$$
0 = \sum_{k=1}^{N} \exp\left[\pm\frac{\pi n}{N}(2k - 2)i\right] = \frac{\exp(\pm 2\pi n i) - 1}{\exp(\pm 2\pi n i/N) - 1} \tag{3.7.8}
$$

Therefore the approximation (3.7.6) is exact for all $\sin n\pi x$ and $\cos n\pi x$, $n \neq 0 (mod N)$. Obviously it is also exact for $n = 0$) since $F(x)$ is constant.

If $\alpha = 0$, the trapezoidal approximation is also exact for any odd function $F(x)$.

Thus the rays directions are equidistant and the weights are identical,

$$J = \sum_{i=1}^{N_{rays}} \frac{1}{N_{rays}} I\left(r^i\right) \tag{3.7.9}$$

as is also the case for the A4 and A6 method of Carlson.

ad 6 - radiative heating
The radiative heating rate is given by

$$Q_{rad} = 4\pi\rho\chi\left(J - S\right) \tag{3.7.10}$$
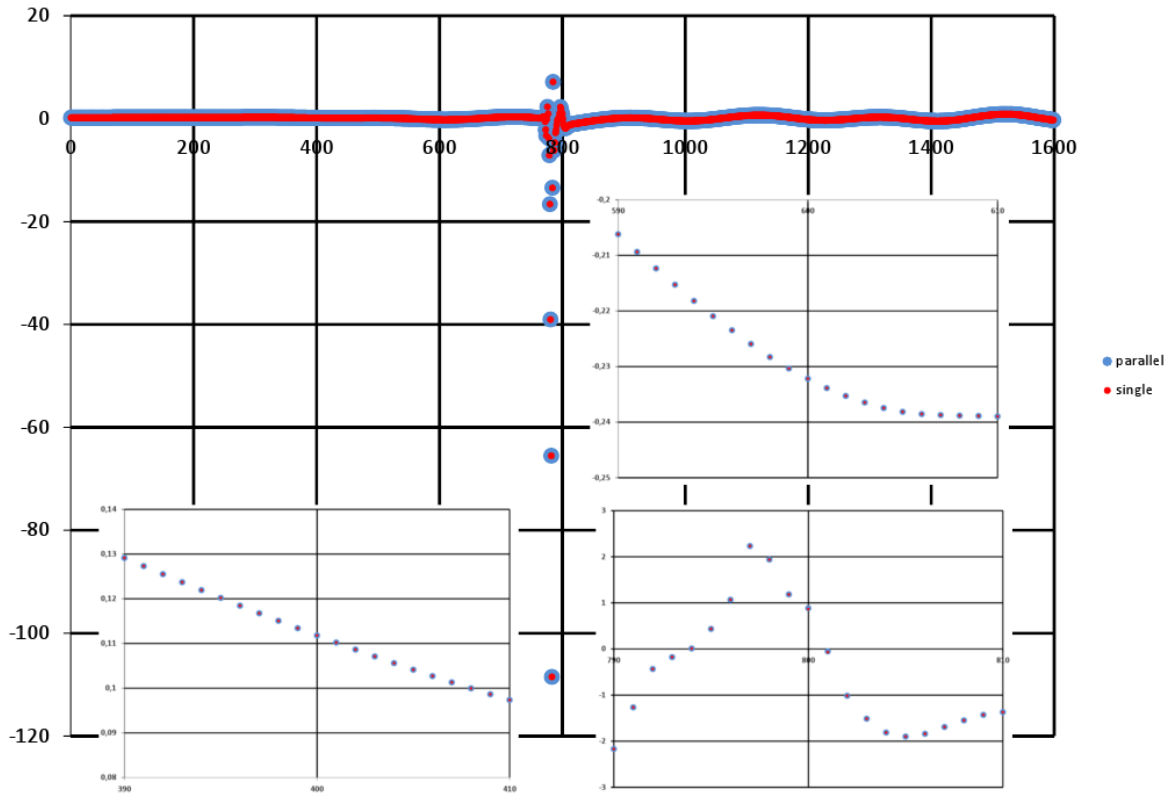
Figure 3.7.4:   parallelisation test

Parallelisation. To calculate the intensity for a specific ray direction in a subdomain the corresponding processor has to wait until the intensity is calculated in the adjacent subdomain from which the ray enters. But, for simulations with numerous processors one has to ensure that as many processors as possible are busy. Since the grid is not homogeneous and is moving the intersection points of the ray with the grid vary with the

radius and shift in time, thus there is no order in which one can follow any ray of given ray direction through the whole computational domain and an algorithm similar to the one implemented for the equidistant grid (see [Obe 2007]) can not be used. For this reason and because the time steps are rather small, the fully parallelized version of radiative transfer is not used. Instead the old values are used on the boundaries of each domain just as it is done for the boundary condition in lateral direction. Figure 3.7.4 shows a 1D simulation with sufficient resolution (magenta line in Figure 3.7.5 on page 53), the border between the domains is between point number $200i$ and $200i + 1$. After 3 minutes (i.e 40000 time steps) there is no visible difference.

3.7.3   The Resolution of Q_{rad}

In order to resolve the steep gradient of density, temperature etc. in the hydrogen ionisation zone a finer resolution than specified in Section 3.2 is needed. To get a first estimate of the required spacing, we compare the pressure scale heights $H_p = P/\nabla P$ in the form $P/(\rho g)$ in the region of interest. Substituting the gas pressure $P_{gas} = \frac{\rho R_{gas} T}{\mu}$ for the pressure P and the effective temperature T_{eff} for the temperature T yields a ratio of pressure scale heights

$$\frac{H_p}{H_{p\odot}} = \frac{T_{eff}\,\mu_\odot\,g_\odot}{T_{eff\odot}\,\mu\,g} \qquad (3.7.11)$$
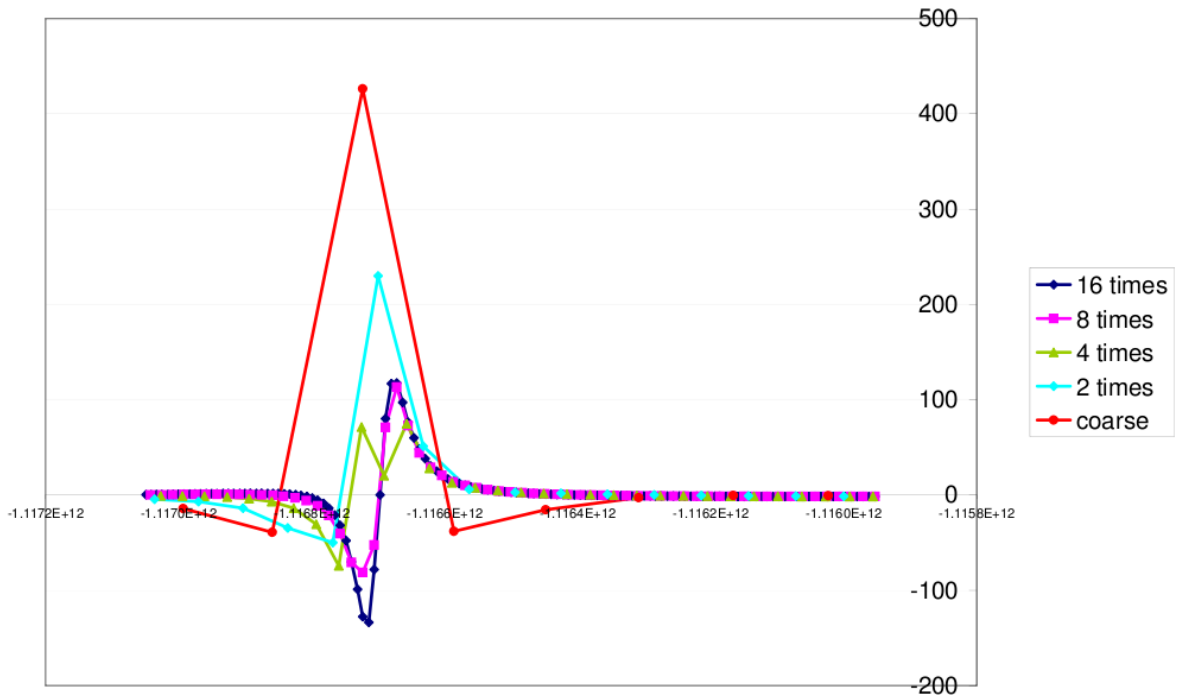

Figure 3.7.5:   the resolution of Q_{rad}

In our simulations of the Sun it was found that a spacing of 20km in radial direction is necessary, this would translate to approximately 4.25 Mm for our particular Cepheid. But we also must take into account the super-adiabatic gradient $\nabla - \nabla_{ad}$. In the Sun $(\nabla - \nabla_{ad})_{\odot} \approx 0.6$ for the Cepheid, who was derived by MLT it depends very much on the α-parameter. For our initial condition no turbulent pressure was included and $\nabla - \nabla_{ad} \approx 14$, thus the grid spacing would reduce to 0.18 Mm or a grid seven times as fine [9]. On the other hand for the same Cepheid with turbulent pressure included $\nabla - \nabla_{ad} \approx 3.2$ and the grid need only be finer by a factor two.

While the first scenario is the only possible solution for a one dimensional, purely radiative simulation, there is reason to assume that in more dimensions a smaller factor can be achieved after convection has set in. The additional computation time is of course substantial, a factor 7 in grid refinement leads to a factor ~ 20 for the number of time steps required when the time step is limited by Δt_{rad} (3.3.2). That this estimations holds true at least in 1D as has been tested and in Figure 3.7.5 on page 53 we present a comparison after 0.25 sec.; obviously a grid refinement of 4 is not enough while a factor 8 suffices, the difference to 16 is not worth the cost.

Here I present one dimensional simulations where the grid was refined over the whole domain. In Chapter 4 a two dimensional simulation with co-moving grid refinement can be found.

3.7.4 Domain Decomposition for Parallelisation

Parallelisation is done with MPI. Each node processes a rectangular subdomain. The number of required processors is specified by the number of subdivisions in all spacial directions. Due to radiative transfer the nodes near the surface have more calculations to work upon, than the ones in the interior that do only diffusion approximation. In [Obe 2007] this problem was solved by an extra domain decomposition for radiative transport and by redistributing all the information needed. But here radiative transport is only done on a small fraction of the total computational domain and since there is a lower limit on the number of points on a single processor, this approach would lead to a small number of processors in radial direction.

This problem is solved by assigning less grid points to the processors on top, so that they are all kept busy at the same time. This is only possible because there is no call to MPI routines during the ENO and the radiative transport routines. With 8 processors in radial direction the distribution was 3 processors with 52 points, one processor with 54 points and 4 processors with 75 points each. The exact numbers depend on the number of rays used.

---

[9]This is the value supplied by Günter Houdek. After interpolation to our grid and reevaluation of the equation of state we arrived at a factor 17

3.8 WENO with Marquina Flux Splitting

If you use a simple polynomial interpolation from the centre grid to the boundary grid shocks or discontinuities either smear out or run into oscillations. In order to avoid this various essentially non oscillatory schemes (ENO[10]) are implemented in the ANTARES code, where interpolation is done by upwinding adaptive stencils. I will concentrate here on the scheme used in my simulations namely ENO of 3rd order with Marquina flux splitting on a moving grid stretched in one direction[11].

The WENO[12] method is a weighted combination of adaptive stencils designed to give high order polynomial approximations of the divergence term in smooth regions. Across discontinuities the smoothest stencil is chosen in spite of its being of lower order. So for a 5th order WENO scheme the 3rd order ENO stencils are combined to give 5th order accuracy in smooth regions, near shocks the accuracy is at least of 3rd order.

In the ANTARES code the WENO scheme of 5th order accuracy is implemented, therefore this and the modifications necessary for a stretched and moving grid will be shown in detail. For hyperbolic systems the set of conservations laws is first transformed to the eigensystem, where the equations decouple and the upwinding directions can be chosen. For the moving grid the grid velocity only enters into the eigenvalues, the eigenvectors are unchanged.

3.8.1 The Basics of ENO

WENO schemes are based on ENO schemes, which were first introduced by Harten, Engquist and Chakravarthy in the form of cell averages. The key idea of ENO schemes is to use the smoothest stencil among several candidates to approximate the fluxes at cell boundaries to a high order accuracy and at the same time to avoid spurious oscillations near shocks. This presentation follows the works of [Shu 1997, FMDO 1998].

The hyperbolic part of the system of conservation laws (2.1.13), (2.1.15) and (2.1.16) can be written as

$$
\frac{\partial}{\partial t}
\begin{bmatrix}
\rho \\
\rho \vec{u} \\
e
\end{bmatrix}
= -\nabla \cdot
\begin{bmatrix}
\rho \vec{u} \\
\rho \vec{u} \vec{u} + p Id \\
(e + p)\,\vec{u}
\end{bmatrix}
\tag{3.8.1}
$$

in two dimensions let

$$
\begin{aligned}
\vec{u} &= (u, v)^T \\
\vec{q} &= (\rho, \rho u, \rho v, e)^T \\
f(\vec{u}) &= \left(\rho u, \rho u^2 + p, \rho uv, (e + p)\, u\right)^T \\
g(\vec{u}) &= \left(\rho v, \rho uv, \rho v^2 + p, (e + p)\, v\right)^T
\end{aligned}
\tag{3.8.2}
$$

---

[10][HEOC 1987], [SO 1988]

[11]The stretching is only done in radial direction, in angular direction the grid is equidistant $q = 1$

[12][LOC 1994], [JS 1996]

then 3.8.2 can be rewritten as

$$\vec{q}_t = - \left([f_r\left(\vec{q}\right)]_r + [f_\varphi\left(\vec{q}\right)]_\varphi \right) = - \sum_{i=1}^{2} [f_{r_i}\left(\vec{q}\right)]_{r_i} \qquad (3.8.3)$$

where $r_1 = r$ and $r_2 = \varphi$.

In the ANTARES code the spatial discretisation is done for each direction separately. At the cell boundaries numerical approximations $\left(\hat{f}_r\right)_{i\pm\frac{1}{2},j}$ and $\left(\hat{f}_\varphi\right)_{i,j\pm\frac{1}{2}}$ are calculated in order to get approximations for

$$
\begin{aligned}
{}[f_r\left(\vec{q}\right)]_r &\approx \frac{1}{\Delta r_i}\left(\left(\hat{f}_r\right)_{i+\frac{1}{2},j} - \left(\hat{f}_r\right)_{i-\frac{1}{2},j}\right) \qquad (3.8.4)\\
{}[f_\varphi\left(\vec{q}\right)]_\varphi &\approx \frac{1}{\Delta\varphi}\left(\left(\hat{f}_\varphi\right)_{i,j+\frac{1}{2}} - \left(\hat{f}_\varphi\right)_{i,j-\frac{1}{2}}\right)
\end{aligned}
$$

at the point $r_{i,j}$. From now on we will consider only one dimension. Note however that the radial and angular direction are different. In radial direction the grid is stretched while it is equidistant in angular direction. I will present here the stencils and coefficients for the stretched grid the values for the equidistant grid can be found in [Obe 2007]. For $i = 1, \ldots, N$ the cell boundaries are $r_{i-\frac{1}{2}} = r_i - \frac{1}{1+\sqrt{q}}h_i$ and $r_{i+\frac{1}{2}} = r_i - \frac{q}{1+\sqrt{q}}h_i$ where $h_i = r_{i+\frac{1}{2}} - r_{i-\frac{1}{2}}$ and the cells are $I_i = \left[r_{i-\frac{1}{2}}, r_{i+\frac{1}{2}}\right]$. Since we do not use ENO near the physical boundaries in the ANTARES code all values are available for $i < 1$ and $i > N$ if needed.

3.8.1.1 Reducing a system into Independent Scalar Equations

Consider a system of N convective conservation laws in one spatial dimension

$$\vec{U}_t + \left[\vec{F}\left(\vec{U}\right)\right]_x = 0 \qquad (3.8.5)$$

The basic idea of characteristic numerical schemes is to transform this nonlinear system into a system of nearly independent scalar equations of the form

$$u_t + v u_x = 0 \qquad (3.8.6)$$

discretise each scalar equation independently in a v-upwind biased fashion, and then transform the discretised system back into the original variables. In a smooth region of the flow, we can get a better understanding of the structure of the system by expanding out the derivatives as

$$\vec{U}_t + J\vec{U}_x = 0 \qquad (3.8.7)$$

where $J = \frac{\partial \vec{F}}{\partial \vec{U}}$ is the Jacobian matrix of the convective flux function. If J were a diagonal matrix with real diagonal elements this system would be decoupled into N independent scalar equations as desired. We will transform this system into that form by multiplying by a matrix that diagonalises J. If this is possible the system is called hyperbolic. The

necessary matrices turn out to be the matrices of left-multiplying and right-multiplying eigenvectors of J. Thus we require that J has N real eigenvalues λ^p, $p = 1, \ldots, N$, and that there are N eigenvectors for multiplying against J from the right. These eigenvectors are the columns of a matrix R in the equation

$$JR = R \, Diag\,(\lambda^p) \qquad (3.8.8)$$

In the same way there are N eigenvalues for multiplying against J from the left, these are used as the rows of a Matrix L so that

$$LJ = Diag\,(\lambda^p)\; L \qquad (3.8.9)$$

Thus the matrices L and R can be chosen to be inverses. These matrices transform to a system of coordinates in which J is diagonalised as desired:

$$LJR = Diag\,(\lambda^p) \qquad (3.8.10)$$

On any particular node x_0 L and R have the values L_0 and R_0. To get a locally diagonalised form the system equation is multiplied by the constant matrix L_0 which diagonalises J at x_0 with eigenvalues λ_0^p and nearly diagonalises J at nearby points.

$$\left[L_0 \vec{U} \right]_t + L_0 J R_0 \left[L_0 \vec{U} \right]_x = 0 \qquad (3.8.11)$$

Thus the equations are sufficiently decoupled for us to apply upwind biased discretisation independently to each component, with λ_0^p determining the upwind biased direction for the p-th component equation. Once this system is fully discretised, the entire system is multiplied by $R_0 = L_0^{-1}$ to return to the original variables.

In terms of (3.8.2) the procedure of discretising at a point is simply to multiply the entire system by the left eigenvector matrix L_0 and discretise the $p = 1, \ldots, N$ scalar components of this system

$$\left[\left(L_0 \vec{U} \right)_p \right]_t + \left[\left(L_0 \vec{F} \left(\vec{U} \right) \right)_p \right]_x = 0 \qquad (3.8.12)$$

independently using upwind biased differencing with the upwind direction for the p-th equation determined by the sign of λ^p. Then the resulting spatially discretised system of equations is multiplied by R_0 to recover the spatially discretised fluxes for the original variables:

$$\vec{U}_t + R_0 \Delta \left(L_0 \vec{F} \left(\vec{U} \right) \right) = 0 \qquad (3.8.13)$$

where Δ stands for the upwind biased discretisation operator.

λ^p is called the p-th characteristic velocity or speed, $\left(L_0 \vec{U} \right)_p = \vec{L}_0^p \cdot \vec{U}$ the p-th characteristic state or field and $\left(L_0 \vec{F} \left(\vec{U} \right) \right)_p = \vec{L}_0^p \cdot \vec{F} \left(\vec{U} \right)$ the p-th characteristic flux. According to the local linearisation it is approximately true that the p-th characteristic field rigidly translates in space at the p-th characteristic velocity. Thus this decomposition corresponds to the local physical propagation of independent "waves" or "signals".

3.8.1.2   Eigenvalues and Eigenvectors for a Moving Grid

If there is a grid velocity involved the matrices of right and left eigenvectors remain unchanged, for two dimensions they are for direction x (u_y is the fluid velocity in the perpendicular direction):

$$R = \begin{pmatrix} 1 & u_x - c & u_y & -u_x c + \frac{e+p}{\rho} \\ 1 & u_x & 0 & \frac{e}{\rho} - u_y^2 - \rho a_2 \\ 0 & 0 & 1 & u_y \\ 1 & u_x + c & u_y & u_x c + \frac{e+p}{\rho} \end{pmatrix} \tag{3.8.14}$$

$$L = \begin{pmatrix} -\frac{1}{2} a_{i1} a_1 + \frac{u_x}{c} & -\frac{1}{2}\left(u_x a_{i1} + \frac{1}{c}\right) & -\frac{1}{2} u_y a_{i1} & \frac{1}{2} a_{i1} \\ a_{i1} a_1 + 1 & u_x a_{i1} & u_y a_{i1} & -a_{i1} \\ a_{i1} u_y a_1 & u_x u_y a_{i1} & 1 + u_y^2 a_{i1} & -u_y a_{i1} \\ -\frac{1}{2} a_{i1} a_1 + \frac{u_x}{c} & -\frac{1}{2}\left(u_x a_{i1} - \frac{1}{c}\right) & -\frac{1}{2} u_y a_{i1} & \frac{1}{2} a_{i1} \end{pmatrix}^T , \tag{3.8.15}$$

where $c = \left(\frac{\partial p}{\partial T} / \left(\rho \frac{\partial \varepsilon}{\partial T} a_{i1}\right)\right)^{1/2}$, $a_1 = -\rho a_2 - u_x^2 - u_y^2 + \frac{e}{\rho}$, $a_2 = -\frac{\partial \varepsilon}{\partial \rho} + \left(\rho \frac{\partial p}{\partial \rho}\right) / a_{i1}$ and $a_{i1} = \frac{\rho}{\rho^2 a_2 + p}$.

The only difference is in the eigenvalues. They change from

$$\begin{pmatrix} u_x - c \\ u_x \\ u_x \\ u_x + c \end{pmatrix} \quad \text{to} \quad \begin{pmatrix} u_x - u_g - c \\ u_x - u_g \\ u_x - u_g \\ u_x - u_g + c \end{pmatrix} \qquad .$$

Reconstruction from cell averages

Given the cell averages $\bar{v}_i \equiv v(r_i)$ of a function we want to find a numerical flux function $\hat{v}_{i+\frac{1}{2}} \equiv \hat{v}(v_{i-r}, \ldots, v_{i+s})$ such that the flux difference approximates the derivative $v'(r_i)$ to k-th order accuracy where v is sufficiently smooth:

$$\frac{1}{\Delta r_i}\left(\hat{v}_{i+\frac{1}{2}} - \hat{v}_{i-\frac{1}{2}}\right) = v'(r_i) + O\left(r_i^k\right) \qquad (i = 1, \ldots N) \tag{3.8.16}$$

where O is a Landau symbol. For each $i = 1, \ldots N$ we consider a stencil $S(i) = \{I_{i-r}, \ldots, I_{i+s}\}$, $r + s = k - 1$, $r, s \geq 0$, then there exists a unique polynomial $p(x)$ of degree k-1 with

$$\frac{1}{\Delta r_i} \int_{r_{i-1/2}}^{r_{i+1/2}} p(\xi)\, d\xi = \bar{v}_i \tag{3.8.17}$$

and

$$p(r_i) = v(r_i) + O\left(r_i^k\right) \tag{3.8.18}$$

inside I_i. In order to construct $p(x)$ we define the primitive function $V(x) = \int_{-\infty}^{x} v(\xi)\, d\xi$ then

$$V\left(r_{i+\frac{1}{2}}\right) = \sum_{j=-\infty}^{i} \int_{r_{j-1/2}}^{r_{j+1/2}} v(\xi)\, d\xi = \sum_{j=-\infty}^{i} \bar{v}_j \Delta r_i \tag{3.8.19}$$

$P(x)$is the unique polynomial of degree $\leq k$ that interpolates $V(x)$ at the $k+1$ points $r_{i-r-1/2}, \ldots, r_{i+s+1/2}$. Let $p(x) = P'(x)$, then 3.8.17 is valid since $\forall j = i - r, \ldots, i + s$

$$
\begin{aligned}
\frac{1}{\Delta r_j} \int_{r_{j-1/2}}^{r_{j+1/2}} p(\xi)\, d\xi &= \frac{1}{\Delta r_j} \int_{r_{j-1/2}}^{r_{j+1/2}} P'(\xi)\, d\xi \\
&= \frac{1}{\Delta r_j} \left(P\left(r_{j+\frac{1}{2}}\right) - P\left(r_{j-\frac{1}{2}}\right) \right) \\
&= \frac{1}{\Delta r_j} \left(V\left(r_{j+\frac{1}{2}}\right) - V\left(r_{j-\frac{1}{2}}\right) \right) \\
&= \frac{1}{\Delta r_j} \left(\int_{-\infty}^{r_{j+1/2}} v(\xi)\, d\xi - \int_{-\infty}^{r_{j-1/2}} v(\xi)\, d\xi \right) \\
&= \frac{1}{\Delta r_j} \int_{r_{j-1/2}}^{r_{j+1/2}} v(\xi)\, d\xi \\
&= \bar{v}_j
\end{aligned}
$$

Since $P(r_i) = V(r_i) + O\left(\Delta r_i^{k+1}\right)$ standard approximation theory yields $p(r_i) = v(r_i) + O\left(\Delta r_i^{k+1}\right)$ and (3.8.18) is valid.

grid	$r_{i-\frac{5}{2}}$	r_{i-2}	$r_{i-\frac{3}{2}}$	r_{i-1}	$r_{i-\frac{1}{2}}$	r_i	$r_{i+\frac{1}{2}}$	r_{i+1}	$r_{i+\frac{3}{2}}$	r_{i+2}	$r_{i+\frac{5}{2}}$	r_{i+3}
$S_{-1}(i)$		r_{i-2}		r_{i-1}		r_i	$r_{i+\frac{1}{2}}$					
$S_0(i)$				r_{i-1}		r_i	$r_{i+\frac{1}{2}}$	r_{i+1}				
$S_1(i)$						r_i	$r_{i+\frac{1}{2}}$	r_{i+1}		r_{i+2}		
$S_2(i)$							$r_{i+\frac{1}{2}}$	r_{i+1}		r_{i+2}		r_{i+3}

Table 3.3:   stencil location $S_r(i)$for $k=3$ and $r=-1, 0, 1, 2$

The polynomial $p(r_i)$ give s the approximations:

$$
\begin{aligned}
\hat{v}_{i+1/2}^- &= p\left(r_{i+1/2}\right) = v\left(r_{i+1/2}\right) + O\left(\Delta r_i^k\right) \\
\hat{v}_{i-1/2}^+ &= p\left(r_{i-1/2}\right) = v\left(r_{i-1/2}\right) + O\left(\Delta r_i^k\right)
\end{aligned}
$$

k	r	j=0	j=1	j=2
1	-1	1		
	0	1		
2	-1	$\frac{q+2}{q+1}$	$-\frac{1}{q+1}$	
	0	$\frac{q}{q+1}$	$\frac{1}{q+1}$	
	1	$-\frac{q}{q+1}$	$\frac{2q+1}{q+1}$	
3	-1	$\frac{q^3+3q^2+4q+3}{q^3+2q^2+2q+1}$	$-\frac{q^3+2q^2+3q+1}{q(q^3+2q^2+2q+1)}$	
	0	$\frac{q^2}{q^2+q+1}$	$\frac{q^2+2q+2}{q^3+2q^2+2q+1}$	$-\frac{1}{q^3+2q^2+2q+1}$
	1	$-\frac{q^3}{q^3+2q^2+2q+1}$	$\frac{q(2q^2+2q+1)}{q^3+2q^2+2q+1}$	$\frac{1}{q^2+q+1}$
	2	$\frac{q^3}{q^2+q+1}$	$-\frac{q(q^3+3q^2+2q+1)}{q^3+2q^2+2q+1}$	$\frac{3q^3+4q^2+3q+1}{q^3+2q^2+2q+1}$

Table 3.4:   the constants c_{rj} for $k = 1, 2, 3$, $j = 0, 1, 2$

j	r=-1	r=0	r=1
0	$\frac{q^5+3q^4+5q^3+7q^2+5q+4}{q^5+2q^4+3q^3+3q^2+2q+1}$	$\frac{q^3}{q^3+q^2+q+1}$	$-\frac{q^5}{q^5+2q^4+3q^3+3q^2+2q+1}$
1	$-\frac{q^6+2q^5+5q^4+5q^3+6q^2+3q+1}{q^2(q^5+2q^4+3q^3+3q^2+2q+1)}$	$\frac{q^4+2q^3+4q^2+3q+3}{q^5+2q^4+3q^3+3q^2+2q+1}$	$\frac{q^2(2q^3+2q^2+2q+1)}{q^5+2q^4+3q^3+3q^2+2q+1}$
2	$\frac{q^5+2q^4+3q^3+4q^2+2q+1}{q^3(q^5+2q^4+3q^3+3q^2+2q+1)}$	$-\frac{q^3+q^2+2q+1}{q(q^5+2q^4+3q^3+3q^2+2q+1)}$	$\frac{q^3+2q^2+2q+2}{q^5+2q^4+3q^3+3q^2+2q+1}$
3	$-\frac{1}{q^3(q^3+q^2+q+1)}$	$\frac{1}{q(q^5+2q^4+3q^3+3q^2+2q+1)}$	$-\frac{1}{q^5+2q^4+3q^3+3q^2+2q+1}$

Table 3.5:   the constants c_{rj} for $k = 4$, $r = -1, 0, 1$

j	r=2	r=3
0	$\dfrac{q^6}{q^5+2q^4+3q^3+3q^2+2q+1}$	$-\dfrac{q^6}{q^3+q^2+q+1}$
1	$-\dfrac{q^3\left(q^3+2q^2+q+1\right)}{q^5+2q^4+3q^3+3q^2+2q+1}$	$\dfrac{q^3\left(q^5+2q^4+4q^3+3q^2+2q+1\right)}{q^5+2q^4+3q^3+3q^2+2q+1}$
2	$\dfrac{q\left(3q^4+3q^3+4q^2+2q+1\right)}{q^5+2q^4+3q^3+3q^2+2q+1}$	$-\dfrac{q\left(q^6+3q^5+6q^4+5q^3+5q^2+2q+1\right)}{q^5+2q^4+3q^3+3q^2+2q+1}$
3	$\dfrac{1}{q^3+q^2+q+1}$	$\dfrac{4q^5+5q^4+7q^3+5q^2+3q+1}{q^5+2q^4+3q^3+3q^2+2q+1}$

Table 3.6:   the constants c_{rj} for $k=4$, $r=2,3$

j	r=-1
0	$\dfrac{q^9+4q^8+9q^7+16q^6+22q^5+26q^4+24q^3+19q^2+11q+5}{q^9+3q^8+6q^7+9q^6+11q^5+11q^4+9q^3+6q^2+3q+1}$
1	$-\dfrac{q^{11}+3q^{10}+8q^9+14q^8+22q^7+27q^6+29q^5+25q^4+19q^3+10q^2+4q+1}{q^3(q^9+3q^8+6q^7+9q^6+11q^5+11q^4+9q^3+6q^2+3q+1)}$
2	$\dfrac{q^{11}+3q^{10}+7q^9+13q^8+19q^7+23q^6+24q^5+21q^4+14q^3+8q^2+3q+1}{q^5(q^9+3q^8+6q^7+9q^6+11q^5+11q^4+9q^3+6q^2+3q+1)}$
3	$-\dfrac{q^7+2q^6+3q^5+4q^4+5q^3+3q^2+2q+1}{q^6(q^7+2q^6+3q^5+4q^4+4q^3+3q^2+2q+1)}$
4	$\dfrac{1}{q^6(q^4+q^3+q^2+q+1)}$

j	r=0
0	$\dfrac{q^4}{q^4+q^3+q^2+q+1}$
1	$\dfrac{q^8+3q^7+7q^6+11q^5+15q^4+15q^3+13q^2+8q+4}{q^9+3q^8+6q^7+9q^6+11q^5+11q^4+9q^3+6q^2+3q+1}$
2	$-\dfrac{q^8+2q^7+5q^6+7q^5+9q^4+8q^3+7q^2+3q+1}{q^2(q^9+3q^8+6q^7+9q^6+11q^5+11q^4+9q^3+6q^2+3q+1)}$
3	$\dfrac{q^6+2q^5+3q^4+4q^3+4q^2+2q+1}{q^3(q^9+3q^8+6q^7+9q^6+11q^5+11q^4+9q^3+6q^2+3q+1)}$
4	$-\dfrac{1}{q^3(q^7+2q^6+3q^5+4q^4+4q^3+3q^2+2q+1)}$

Table 3.7:   the constants c_{rj} for $k=5$, $r=-1,0$

j	r=1
0	$-\dfrac{q^7}{q^7+2q^6+3q^5+4q^4+4q^3+3q^2+2q+1}$
1	$\dfrac{q^3\left(2q^4+2q^3+2q^2+2q+1\right)}{q^7+2q^6+3q^5+4q^4+4q^3+3q^2+2q+1}$
2	$\dfrac{q^7+3q^6+6q^5+9q^4+10q^3+9q^2+6q+3}{q^9+3q^8+6q^7+9q^6+11q^5+11q^4+9q^3+6q^2+3q+1}$
3	$-\dfrac{q^5+2q^4+3q^3+3q^2+3q+1}{q(q^9+3q^8+6q^7+9q^6+11q^5+11q^4+9q^3+6q^2+3q+1)}$
4	$\dfrac{1}{q(q^8+2q^7+4q^6+5q^5+6q^4+5q^3+4q^2+2q+1)}$

j	r=2
0	$\dfrac{q^9}{q^8+2q^7+4q^6+5q^5+6q^4+5q^3+4q^2+2q+1}$
1	$-\dfrac{q^5\left(q^5+3q^4+3q^3+3q^2+2q+1\right)}{q^9+3q^8+6q^7+9q^6+11q^5+11q^4+9q^3+6q^2+3q+1}$
2	$\dfrac{q^2\left(3q^7+6q^6+9q^5+10q^4+9q^3+6q^2+3q+1\right)}{q^9+3q^8+6q^7+9q^6+11q^5+11q^4+9q^3+6q^2+3q+1}$
3	$\dfrac{q^4+2q^3+2q^2+2q+2}{q^7+2q^6+3q^5+4q^4+4q^3+3q^2+2q+1}$
4	$-\dfrac{1}{q^7+2q^6+3q^5+4q^4+4q^3+3q^2+2q+1}$

j	r=3
0	$-\dfrac{q^{10}}{q^7+2q^6+3q^5+4q^4+4q^3+3q^2+2q+1}$
1	$\dfrac{q^6\left(q^6+2q^5+4q^4+4q^3+3q^2+2q+1\right)}{q^9+3q^8+6q^7+9q^6+11q^5+11q^4+9q^3+6q^2+3q+1}$
2	$-\dfrac{q^3\left(q^8+3q^7+7q^6+8q^5+9q^4+7q^3+5q^2+2q+1\right)}{q^9+3q^8+6q^7+9q^6+11q^5+11q^4+9q^3+6q^2+3q+1}$
3	$\dfrac{q\left(4q^8+8q^7+13q^6+15q^5+15q^4+11q^3+7q^2+3q+1\right)}{q^9+3q^8+6q^7+9q^6+11q^5+11q^4+9q^3+6q^2+3q+1}$
4	$\dfrac{1}{q^4+q^3+q^2+q+1}$

Table 3.8:   the constants c_{rj} for $k=5$, $r=1,2,3$

j	r=4
0	$\frac{q^{10}}{q^4+q^3+q^2+q+1}$
1	$-\frac{q^6\left(q^7+2q^6+3q^5+5q^4+4q^3+3q^2+2q+1\right)}{q^7+2q^6+3q^5+4q^4+4q^3+3q^2+2q+1}$
2	$\frac{q^3\left(q^{11}+3q^{10}+8q^9+14q^8+21q^7+24q^6+23q^5+19q^4+13q^3+7q^2+3q+1\right)}{q^9+3q^8+6q^7+9q^6+11q^5+11q^4+9q^3+6q^2+3q+1}$
3	$-\frac{q\left(q^{11}+4q^{10}+10q^9+19q^8+25q^7+29q^6+27q^5+22q^4+14q^3+8q^2+3q+1\right)}{q^9+3q^8+6q^7+9q^6+11q^5+11q^4+9q^3+6q^2+3q+1}$
4	$\frac{5q^9+11q^8+19q^7+24q^6+26q^5+22q^4+16q^3+9q^2+4q+1}{q^9+3q^8+6q^7+9q^6+11q^5+11q^4+9q^3+6q^2+3q+1}$

Table 3.9: the constants c_{rj} for $k=5$, $r=4$

Differentiating $v\left(r_i\right)=\overline{v}_i=\frac{1}{\Delta r_i}\int_{r_{i-1/2}}^{r_{i+1/2}}v\left(\xi\right)d\xi$ gives $v\left(r_i\right)=\frac{1}{\Delta r_i}\left(v\left(r_{j+\frac{1}{2}}\right)-v\left(r_{j-\frac{1}{2}}\right)\right)$and after replacing $v\left(r_{j+\frac{1}{2}}\right)$and $v\left(r_{j-\frac{1}{2}}\right)$ by the approximations $\hat{v}_{i+1/2}^-$ and $\hat{v}_{i-1/2}^+$ the accuracy requirement (3.8.25) is met as long as the $O\left(\Delta r_i^k\right)$ terms in the approximations $\hat{v}_{i+1/2}^-$ and $\hat{v}_{i-1/2}^+$are smooth - an assumption that is true in practice. Hence the difference in (3.8.25) gives an extra $O\left(\Delta r_i\right)$ to cancel the one in the denominator.

The mapping from the given cell averages $\{\overline{v}_j\}$ in the stencil $S\left(i\right)$ to the values $\hat{v}_{i+1/2}^-$ and $\hat{v}_{i-1/2}^+$ is linear. Therefore there exist constants c_{rj} and $\tilde{c}_{rj}$ depending on the left shift r of the stencil $S\left(i\right)$ and the accuracy order k but not on the function $v\left(x\right)$ itself, such that:

$$\hat{v}_{i+1/2}^- = \sum_{j=0}^{k-1}c_{rj}\overline{v}_{i-r+j}$$

$$\hat{v}_{i-1/2}^+ = \sum_{j=0}^{k-1}\tilde{c}_{rj}\overline{v}_{i-r+j}$$

For reasons of symmetry $\tilde{c}_{rj}=c_{r-1,j}$. By manipulating the interpolation polynomial $P\left(x\right)$ and taking the derivative to get $p\left(x\right)$ one gets these coefficients c_{rj} and $\tilde{c}_{rj}$ which are prestored in the code. In tables 3.1 to 3.8 the coefficients up to order $k=5$ for a stretched grid can be seen. For ANTARES the orders 3 and 5 are relevant. Coefficients for the equidistant grid up to order $k=6$ can be found in [Obe 2007, Shu 1997].

Near discontinuities in the solution of hyperbolic conservation laws oscillations can occur because the stencil contains discontinuities. Therefore an adaptive stencil $S\left(i\right)$ is chosen for the interpolation of the cell boundary fluxes, the left shift r changes with the location r_i. The main idea of ENO approximation is after all to exclude discontinuous cells from the stencil $S\left(i\right)$.

3.8.2   The Advantages of WENO

Instead of choosing the „smoothest" stencil for the interpolation polynomial in the ENO reconstruction, a convex combination of all candidates is used to achieve the essentially non-oscillatory property. [LOC 1994]

Instead of performing a *2k-1* (5 in ANTARES) order ENO scheme using stencils of that order a combination of k stencils of order k is used to obtain the final accuracy $2k - 1$.

For a k-th order ENO scheme there are k candidate stencils

$$S_r\left(i\right) = \left\{x_{i-r}, \ldots, x_{i-r+k-1}\right\}, \quad r = 1, \ldots, k-1$$

which produce k different reconstructions of the value $v_{i+\frac{1}{2}}$:

$$\hat{v}^{(r)}_{i+1/2} = \sum_{j=0}^{k-1} c_{rj}\overline{v}_{i-r+j}, \quad r = 1, \ldots, k-1$$

The convex combination of the values $\hat{v}^{(r)}_{i+1/2}$ for the WENO approach is

$$\hat{v}_{i+1/2} = \sum_{r=0}^{k-1} w_r\hat{v}^{(r)}_{i+1/2}, \quad r = 1, \ldots, k-1$$

and is used as a new approximation for $\bar{v}_{i+1/2}$. For the weights $w_r \geq 0$, $\forall r$ and $\sum_{r=0}^{k-1} w_r = 1$ must be true. For a smooth function $v\left(x\right)$there are constants d_r so that $\sum_{k=0}^{k-1} d_r = 1$ and

$$\hat{v}^-_{i+1/2} = \sum_{r=0}^{k-1} d_r\hat{v}^{(r)}_{i+1/2} = v\left(r_{i+1/2}\right) + O\left(\triangle r_i^{2k-1}\right) \tag{3.8.20}$$

and constants $\widetilde{d}_r$ so that $\sum_{k=0}^{k-1} \tilde{d}_r = 1$ and

$$\hat{v}^+_{i-1/2} = \sum_{r=0}^{k-1} \tilde{d}_r\hat{v}^{(r)}_{i+1/2} = v\left(r_{i-1/2}\right) + O\left(\triangle r_i^{2k-1}\right) \tag{3.8.21}$$

On the stretched grid for these constants are

k	d_0	d_1	d_2
1	1		
2	$\frac{q+1}{q^2+q+1}$	$\frac{q^2}{q^2+q+1}$	
3	$\frac{q^2+q+1}{q^6+q^5+2q^4+2q^3+2q^2+q+1}$	$\frac{q^2\left(q^3+2q^2+2q+1\right)}{q^6+q^5+2q^4+2q^3+2q^2+q+1}$	$\frac{q^6}{q^6+q^5+2q^4+2q^3+2q^2+q+1}$

Table 3.10:   weights for k=1,2,3 for $\hat{v}^-_{i+1/2}$

k	$\tilde{d}_0$	$\tilde{d}_1$	$\tilde{d}_2$
1	1		
2	$\frac{1}{q^2+q+1}$	$\frac{q^2+q}{q^2+q+1}$	
3	$\frac{1}{q^6+q^5+2q^4+2q^3+2q^2+q+1}$	$\frac{q(q^3+2q^2+2q+1)}{q^6+q^5+2q^4+2q^3+2q^2+q+1}$	$\frac{q^4(q^2+q+1)}{q^6+q^5+2q^4+2q^3+2q^2+q+1}$

<div align="center">Table 3.11:   weights for k=1,2,3 for $\hat{v}^+_{i-1/2}$</div>

Note that $\tilde{d}_r \neq d_{k-1-r}$ for the stretched grid but would be the same if it where equidistant ($q = 1$).

If $w_r = d_r + O\left(\triangle r_i^{2k-1}\right)$ then $\hat{v}^{\mp}_{i\pm1/2}$ $(2k-1)$-th order accurate since

$$
\begin{aligned}
\sum_{r=0}^{k-1} w_r \hat{v}^{(r)}_{i+1/2} - \sum_{r=0}^{k-1} d_r \hat{v}^{(r)}_{i+1/2} &= \sum_{r=0}^{k-1} (w_r - d_r)\left(\hat{v}^{(r)}_{i+1/2} - v\,(i+1/2)\right) \\
&= \sum_{r=0}^{k-1} O\left(\triangle r_i^{k-1}\right) O\left(\triangle r_i^k\right) \\
&= O\left(\triangle r_i^{2k-1}\right)
\end{aligned}
$$

In [LOC 1994] weights of the form

$$
w_r = \frac{\alpha_r}{\sum_{s=0}^{k-1} \alpha_s} \tag{3.8.22}
$$

with $\alpha_r = \frac{d_r}{(\varepsilon+\beta_r)^2}$ are proposed. $\varepsilon > 0$ is the machine accuracy, which is introduced here to ensure that the denominator does not become zero. β_r are smoothness indicators of the stencil supposed to be zero when contains a discontinuity. A robust choice of smoothness indicators is defined by

$$
\beta_r = \sum_{l=1}^{k-1} \int_{r_{i-1/2}}^{r_{i+1/2}} \triangle r_i^{2l-1} \left(\frac{\partial^l p_r\,(x)}{\partial^l x}\right) dx \tag{3.8.23}
$$

where $p_r\,(x)$ is the reconstruction polynomial on the stencil $S_r\,(i)$. The smoothness indicators β_r are a measure for the total variation in the interval I_i.

With this choice the smoothness indicators are for $k = 2$:

$$
\begin{aligned}
\beta_0 &= \left(\frac{2}{q+1}\bar{v}_{i+1} - \frac{2}{q+1}\bar{v}_i\right)^2 \\
\beta_1 &= \left(\frac{2q}{q+1}\bar{v}_i - \frac{2q}{q+1}\bar{v}_{i-1}\right)^2
\end{aligned} \tag{3.8.24}
$$

and for $k = 3$:

$$\begin{aligned}
\beta_0 &= Y_0^2 \left(\bar{v}_i - (q+1)\bar{v}_{i+1} + \bar{v}_{i+2}\right)^2 + \left(Z_{10}\bar{v}_i + Z_{20}\bar{v}_{i+1} + Z_{30}\bar{v}_{i+2}\right)^2 \\
\beta_1 &= Y_1^2 \left(\bar{v}_i - (q+1)\bar{v}_{i+1} + \bar{v}_{i+2}\right)^2 + \left(Z_{11}\bar{v}_{i-1} + Z_{21}\bar{v}_i + Z_{31}\bar{v}_{i+1}\right)^2 \quad (3.8.25) \\
\beta_2 &= Y_2^2 \left(\bar{v}_i - (q+1)\bar{v}_{i+1} + \bar{v}_{i+2}\right)^2 + \left(Z_{12}\bar{v}_{i-2} + Z_{22}\bar{v}_{i-1} + Z_{32}\bar{v}_i\right)^2
\end{aligned}$$

where

β	Y	Z_1	Z_2	Z_3
0	$\dfrac{\sqrt{39}}{q(q^3+2q^2+2q+1)}$	$\dfrac{2q^2+4q+3}{q^3+2q^2+2q+1}$	$-\dfrac{2q^3+4q^2+5q+1}{q(q^3+2q^2+2q+1)}$	$\dfrac{2q+1}{q(q^3+2q^2+2q+1)}$
1	$\dfrac{\sqrt{39}q}{q^3+2q^2+2q+1}$	$\dfrac{2q^3+q^2}{q^3+2q^2+2q+1}$	$\dfrac{-2q^3-q^2+q+2}{q^3+2q^2+2q+1}$	$-\dfrac{q+2}{q^3+2q^2+2q+1}$
2	$\dfrac{\sqrt{39}q^3}{q^3+2q^2+2q+1}$	$\dfrac{q^4+2q^3}{q^3+2q^2+2q+1}$	$-\dfrac{q^4+5q^3+4q^2+2q}{q^3+2q^2+2q+1}$	$\dfrac{3q^3+4q^2+2q}{q^3+2q^2+2q+1}$

Table 3.12:   smoothness indicators for $k = 3$

With these ingredients the WENO algorithm can be performed in the following way

- The coefficients c_{rj}, d_r, Y_r and Z_{rj} are prestored.

- Calculate the k approximations $\hat{v}_{i+1/2}^{(r)}$ and $\hat{v}_{i-1/2}^{(r)}$ of order k

- Determine the smoothness indicators β_r3.8.25

- Form the weights w_r 3.8.22

- Calculate the $(2k-1)$-th order accurate reconstructions $\hat{v}_{i+1/2}^-$ and $\hat{v}_{i-1/2}^+$.

The ENO or WENO-algorithm yields two values $\hat{v}_{i+1/2}^-$ resulting from the stencil $S(i)$ and $\hat{v}_{i-1/2}^+$ resulting from $S(i+1)$. For stability it is important that upwinding is used in constructing, this can be achieved by computing the Roe speed $\bar{a}_{i+1/2} \equiv \frac{f(u_{i+1})-f(u_i)}{u_{i+1}-u_i}$

- If $\bar{a}_{i+1/2} \geq 0$ the movement is from the left. The numerical flux $\hat{f}_{i+1/2}$ is $\hat{v}_{i+1/2}^-$.

- Otherwise the movement is from the right. The numerical flux $\hat{f}_{i+1/2}$ is $\hat{v}_{i-1/2}^+$.

3.8.3   A Different Approach to WENO-Coefficients

From a different point of view another set of approximation coefficients C_{rj}, weights D_r and smoothness indicators B_i can be derived, which are also available in the ANTARES-code and were used for simulations presented in Chapter 4. Instead of as viewing $v(r_i)$

as cell averages and interpolating the primitive function, the flux function $v(r_i)$ itself is interpolated to the boundaries, leading to a different set of coefficients. This approach was chosen because we use a polar grid and though the spacing is that of a stretched grid in radial direction, the cell-volumes depend also on the radius as does the shape of the cells. Though this error is very small it can not be neglected.

k	r	j=0	j=1	j=2	j=3	j=4
1	-1	1				
	0	1				
2	-1	3/2	-1/2			
	0	1/2	1/2			
	1	-1/2	3/2			
3	-1	15/8	-5/4	3/8		
	0	3/8	3/4	-1/8		
	1	$-1/8$	3/4	3/8		
	2	3/8	-5/4	15/8		
4	-1	35/16	-35/16	21/16	-5/16	
	0	5/16	15/16	-5/16	1/16	
	1	$-1/16$	9/16	9/16	-1/16	
	2	1/16	-5/16	15/16	5/16	
	3	$-5/16$	21/16	-35/16	35/16	
5	-1	315/128	-105/32	189/64	-45/32	35/128
	0	35/128	35/32	-35/64	7/32	-5/128
	1	$-5/128$	15/32	45/64	-5/32	3/128
	2	3/128	-5/32	45/64	15/32	-5/128
	3	$-5/128$	7/32	-35/64	35/32	35/128
	4	35/128	-45/32	189/64	-105/32	315/128

Table 3.13: the constants C_{rj} for $k = 1, \ldots, 5$, $j = 0, \ldots, 4$ on an equidistant grid

k	r	j=0	j=1	j=2
1	-1	1		
	0	1		
2	-1	$\dfrac{a^2+a+1}{a(a+1)}$	$-\dfrac{1}{a(a+1)}$	
	0	$\dfrac{a^2}{a^2+1}$	$\dfrac{1}{a^2+1}$	
	1	$-\dfrac{a^2}{a+1}$	$\dfrac{a^2+a+1}{a+1}$	
3	-1	$\dfrac{a^6+2a^5+3a^4+3a^3+3a^2+2a+1}{a^2(a^4+2a^3+2a^2+2a+1)}$	$-\dfrac{a^4+a^3+a^2+a+1}{a^4(a^2+2a+1)}$	$\dfrac{a^2+a+1}{a^4(a^4+2a^3+2a^2+2a+1)}$
	0	$\dfrac{a^2\left(a^2+a+1\right)}{a^4+2a^3+2a^2+2a+1}$	$\dfrac{a^2+a+1}{a(a^2+2a+1)}$	$-\dfrac{1}{a(a^4+2a^3+2a^2+2a+1)}$
	1	$-\dfrac{a^5}{a+2a^3+2a^2+2a+1}$	$\dfrac{a\left(a^2+a+1\right)}{a+2a+1}$	$\dfrac{a^2+a+1}{a^4+2a^3+2a^2+2a+1}$
	2	$\dfrac{a^6\left(a^2+a+1\right)}{a^4+2a^3+2a^2+2a+1}$	$-\dfrac{a^2\left(a^4+a^3+a^2+a+1\right)}{a^2+2a+1}$	$\dfrac{a^6+2a^5+3a^4+3a^3+3a^2+2a+1}{a^4+2a^3+2a^2+2a+1}$

Table 3.14:   the constants C_{rj} for $k = 1, 2, 3$, $j = 0, 1, 2$

On the stretched grid, for better readability $a \equiv \sqrt{q}$:

j	r=-1
0	$\dfrac{a^{10}+2a^9+3a^8+4a^7+5a^6+5a^5+5a^4+4a^3+3a^2+2a+1}{a^3(a^7+2a^6+2a^5+3a^4+3a^3+2a^2+2a+1)}$
1	$-\dfrac{a^{10}+2a^9+3a^8+4a^7+5a^6+5a^5+5a^4+4a^3+3a^2+2a+1}{a^7(a^5+3a^4+4a^3+4a^2+3a+1)}$
2	$\dfrac{a^8+2a^7+3a^6+3a^5+3a^4+3a^3+3a^2+2a+1}{a^9(a^5+3a^4+4a^3+4a^2+3a+1)}$
3	$-\dfrac{a^4+a^3+a^2+a+1}{a^9(a^7+2a^6+2a^5+3a^4+3a^3+2a^2+2a+1)}$

Table 3.15:   the constants c_{rj} for $k = 4$, $r = -1$

j	r=0	r=1
0	$\dfrac{a^3\left(a^4+a^3+a^2+a+1\right)}{a^7+2a^6+2a^5+3a^4+3a^3+2a^2+2a+1}$	$-\dfrac{a^8}{a^7+2a^6+2a^5+3a^4+3a^3+2a^2+2a+1}$
1	$\dfrac{a^6+2a^5+3a^4+3a^3+3a^2+2a+1}{a^2(a^5+3a^4+4a^3+4a^2+3a+1)}$	$\dfrac{a^2\left(a^4+2a^3+3a^2+2a+1\right)}{a^5+3a^4+4a^3+4a^2+3a+1}$
2	$-\dfrac{a^4+a^3+a^2+a+1}{a^4(a^5+3a^4+4a^3+4a^2+3a+1)}$	$\dfrac{a^4+2a^3+3a^2+2a+1}{a(a^5+3a^4+4a^3+4a^2+3a+1)}$
3	$\dfrac{1}{a^4(a^7+2a^6+2a^5+3a^4+3a^3+2a^2+2a+1)}$	$-\dfrac{1}{a(a^7+2a^6+2a^5+3a^4+3a^3+2a^2+2a+1)}$

j	r=2	r=3
0	$\dfrac{a^{11}}{a^7+2a^6+2a^5+3a^4+3a^3+2a^2+2a+1}$	$-\dfrac{a^{12}\left(a^4+a^3+a^2+a+1\right)}{a^7+2a^6+2a^5+3a^4+3a^3+2a^2+2a+1}$
1	$-\dfrac{a^5\left(a^4+a^3+a^2+a+1\right)}{a^5+3a^4+4a^3+4a^2+3a+1}$	$\dfrac{a^6\left(a^8+2a^7+3a^6+3a^5+3a^4+3a^3+3a^2+2a+1\right)}{a^5+3a^4+4a^3+4a^2+3a+1}$
2	$\dfrac{a\left(a^6+2a^5+3a^4+3a^3+3a^2+2a+1\right)}{a^5+3a^4+4a^3+4a^2+3a+1}$	$-\dfrac{a^2\left(a^{10}+2a^9+3a^8+4a^7+5a^6+5a^5+5a^4+4a^3+3a^2+2a+1\right)}{a^5+3a^4+4a^3+4a^2+3a+1}$
3	$\dfrac{a^4+a^3+a^2+a+1}{a^7+2a^6+2a^5+3a^4+3a^3+2a^2+2a+1}$	$\dfrac{a^{10}+2a^9+3a^8+4a^7+5a^6+5a^5+5a^4+4a^3+3a^2+2a+1}{a^7+2a^6+2a^5+3a^4+3a^3+2a^2+2a+1}$

Table 3.16: the constants c_{rj} for $k=4$, $r=0,...,3$

j	r=-1
0	$\dfrac{a^{18}+3a^{17}+6a^{16}+10a^{15}+15a^{14}+20a^{13}+25a^{12}+29a^{11}+32a^{10}+33a^9+32a^8+29a^7+25a^6+20a^5+15a^4+10a^3+6a^2+3a+1}{a^4(a^{14}+3a^{13}+5a^{12}+8a^{11}+11a^{10}+13a^9+15a^8+16a^7+15a^6+13a^5+11a^4+8a^3+5a^2+3a+1)}$
1	$-\dfrac{a^{16}+2a^{15}+3a^{14}+5a^{13}+7a^{12}+8a^{11}+10a^{10}+11a^9+11a^8+11a^7+10a^6+8a^5+7a^4+5a^3+3a^2+2a+1}{a^{10}(a^8+3a^7+4a^6+5a^5+6a^4+5a^3+4a^2+3a+1)}$
2	$\dfrac{a^{16}+3a^{15}+6a^{14}+9a^{13}+12a^{12}+15a^{11}+18a^{10}+20a^9+21a^8+20a^7+18a^6+15a^5+12a^4+9a^3+6a^2+3a+1}{a^{14}(a^8+4a^7+8a^6+12a^5+14a^4+12a^3+8a^2+4a+1)}$
3	$-\dfrac{a^{12}+2a^{11}+3a^{10}+4a^9+5a^8+5a^7+5a^6+5a^5+5a^4+4a^3+3a^2+2a+1}{a^{16}(a^8+3a^7+4a^6+5a^5+6a^4+5a^3+4a^2+3a+1)}$
4	$\dfrac{a^{10}+2a^9+3a^8+4a^7+5a^6+5a^5+5a^4+4a^3+3a^2+2a+1}{a^{16}(a^{14}+3a^{13}+5a^{12}+8a^{11}+11a^{10}+13a^9+15a^8+16a^7+15a^6+13a^5+11a^4+8a^3+5a^2+3a+1)}$

Table 3.17: the constants C_{rj} for $k=5$, $r=-1$

j	r=0
0	$\dfrac{a^4\left(a^{10}+2a^9+3a^8+4a^7+5a^6+5a^5+5a^4+4a^3+3a^2+2a+1\right)}{a^{14}+3a^{13}+5a^{12}+8a^{11}+11a^{10}+13a^9+15a^8+16a^7+15a^6+13a^5+11a^4+8a^3+5a^2+3a+1}$
1	$\dfrac{a^{10}+2a^9+3a^8+4a^7+5a^6+5a^5+5a^4+4a^3+3a^2+2a+1}{a^3(a^8+3a^7+4a^6+5a^5+6a^4+5a^3+4a^2+3a+1)}$
2	$-\dfrac{a^{10}+2a^9+3a^8+4a^7+5a^6+5a^5+5a^4+4a^3+3a^2+2a+1}{a^7(a^8+4a^7+8a^6+12a^5+14a^4+12a^3+8a^2+4a+1)}$
3	$\dfrac{a^6+a^5+a^4+a^3+a^2+a+1}{a^9(a^8+3a^7+4a^6+5a^5+6a^4+5a^3+4a^2+3a+1)}$
4	$-\dfrac{a^4+a^3+a^2+a+1}{a^9(a^{14}+3a^{13}+5a^{12}+8a^{11}+11a^{10}+13a^9+15a^8+16a^7+15a^6+13a^5+11a^4+8a^3+5a^2+3a+1)}$

j	r=1
0	$-\dfrac{a^{11}\left(a^4+a^3+a^2+a+1\right)}{a^{14}+3a^{13}+5a^{12}+8a^{11}+11a^{10}+13a^9+15a^8+16a^7+15a^6+13a^5+11a^4+8a^3+5a^2+3a+1}$
1	$\dfrac{a^3\left(a^6+2a^5+3a^4+3a^3+3a^2+2a+1\right)}{a^8+3a^7+4a^6+5a^5+6a^4+5a^3+4a^2+3a+1}$
2	$\dfrac{a^8+3a^7+6a^6+8a^5+9a^4+8a^3+6a^2+3a+1}{a^2(a^8+4a^7+8a^6+12a^5+14a^4+12a^3+8a^2+4a+1)}$
3	$-\dfrac{a^4+a^3+a^2+a+1}{a^4(a^8+3a^7+4a^6+5a^5+6a^4+5a^3+4a^2+3a+1)}$
4	$\dfrac{a^2+a+1}{a^4(a^{14}+3a^{13}+5a^{12}+8a^{11}+11a^{10}+13a^9+15a^8+16a^7+15a^6+13a^5+11a^4+8a^3+5a^2+3a+1)}$

j	r=2
0	$\dfrac{a^{16}\left(a^2+a+1\right)}{a^{14}+3a^{13}+5a^{12}+8a^{11}+11a^{10}+13a^9+15a^8+16a^7+15a^6+13a^5+11a^4+8a^3+5a^2+3a+1}$
1	$-\dfrac{a^8\left(a^4+a^3+a^2+a+1\right)}{a^8+3a^7+4a^6+5a^5+6a^4+5a^3+4a^2+3a+1}$
2	$\dfrac{a^2\left(a^8+3a^7+6a^6+8a^5+9a^4+8a^3+6a^2+3a+1\right)}{a^8+4a^7+8a^6+12a^5+14a^4+12a^3+8a^2+4a+1}$
3	$\dfrac{a^6+2a^5+3a^4+3a^3+3a^2+2a+1}{a(a^8+3a^7+4a^6+5a^5+6a^4+5a^3+4a^2+3a+1)}$
4	$-\dfrac{a^4+a^3+a^2+a+1}{a(a^{14}+3a^{13}+5a^{12}+8a^{11}+11a^{10}+13a^9+15a^8+16a^7+15a^6+13a^5+11a^4+8a^3+5a^2+3a+1)}$

Table 3.18:   the constants C_{rj} for $k=5$, $r=0,1,2$

j	r=3
0	$-\dfrac{a^{19}\left(a^4+a^3+a^2+a+1\right)}{a^{14}+3a^{13}+5a^{12}+8a^{11}+11a^{10}+13a^9+15a^8+16a^7+15a^6+13a^5+11a^4+8a^3+5a^2+3a+1}$
1	$\dfrac{a^{11}\left(a^6+a^5+a^4+a^3+a^2+a+1\right)}{a^8+3a^7+4a^6+5a^5+6a^4+5a^3+4a^2+3a+1}$
2	$-\dfrac{a^5\left(a^{10}+2a^9+3a^8+4a^7+5a^6+5a^5+5a^4+4a^3+3a^2+2a+1\right)}{a^8+4a^7+8a^6+12a^5+14a^4+12a^3+8a^2+4a+1}$
3	$\dfrac{a\left(a^{10}+2a^9+3a^8+4a^7+5a^6+5a^5+5a^4+4a^3+3a^2+2a+1\right)}{a^8+3a^7+4a^6+5a^5+6a^4+5a^3+4a^2+3a+1}$
4	$\dfrac{a^{10}+2a^9+3a^8+4a^7+5a^6+5a^5+5a^4+4a^3+3a^2+2a+1}{a^{14}+3a^{13}+5a^{12}+8a^{11}+11a^{10}+13a^9+15a^8+16a^7+15a^6+13a^5+11a^4+8a^3+5a^2+3a+1}$

j	r=4
0	$\dfrac{a^{20}\left(a^{10}+2a^9+3a^8+4a^7+5a^6+5a^5+5a^4+4a^3+3a^2+2a+1\right)}{a^{14}+3a^{13}+5a^{12}+8a^{11}+11a^{10}+13a^9+15a^8+16a^7+15a^6+13a^5+11a^4+8a^3+5a^2+3a+1}$
1	$-\dfrac{a^{12}\left(a^{12}+2a^{11}+3a^{10}+4a^9+5a^8+5a^7+5a^6+5a^5+5a^4+4a^3+3a^2+2a+1\right)}{a^8+3a^7+4a^6+5a^5+6a^4+5a^3+4a^2+3a+1}$
2	$\dfrac{a^6\left(a^{16}+3a^{15}+6a^{14}+9a^{13}+12a^{12}+15a^{11}+18a^{10}+20a^9+21a^8+20a^7+18a^6+15a^5+12a^4+9a^3+6a^2+3a+1\right)}{a^8+4a^7+8a^6+12a^5+14a^4+12a^3+8a^2+4a+1}$
3	$-\dfrac{a^2\left(a^{16}+2a^{15}+3a^{14}+5a^{13}+7a^{12}+8a^{11}+10a^{10}+11a^9+11a^8+11a^7+10a^6+8a^5+7a^4+5a^3+3a^2+2a+1\right)}{a^8+3a^7+4a^6+5a^5+6a^4+5a^3+4a^2+3a+1}$
4	$\dfrac{a^{18}+3a^{17}+6a^{16}+10a^{15}+15a^{14}+20a^{13}+25a^{12}+29a^{11}+32a^{10}+33a^9+32a^8+29a^7+25a^6+20a^5+15a^4+10a^3+6a^2+3a+1}{a^{14}+3a^{13}+5a^{12}+8a^{11}+11a^{10}+13a^9+15a^8+16a^7+15a^6+13a^5+11a^4+8a^3+5a^2+3a+1}$

Table 3.19:   the constants C_{rj} for $k=5$, $r=3,4$

k	1	2	3
D_0	1	$\dfrac{a^2+a+1}{a^3+a^2+a+1}$	$\dfrac{a^4+a^3+a^2+a+1}{a^{10}+a^9+a^8+2a^7+2a^6+2a^5+2a^4+2a^3+a^2+a+1}$
D_1		$\dfrac{a^3}{a^3+a^2+a+1}$	$\dfrac{a^3\left(a^4+a^3+a^2+a+1\right)}{a^8+a^7+a^5+2a^4+a^3+a+1}$
D_2			$\dfrac{a^{10}}{a^{10}+a^9+a^8+2a^7+2a^6+2a^5+2a^4+2a^3+a^2+a+1}$

Table 3.20:   weights for k=1,2,3 for $\hat{v}_{i+1/2}^-$

k	1	2	3
$\tilde{D}_0$	1	$\dfrac{1}{a^3+a^2+a+1}$	$\dfrac{1}{a^{10}+a^9+a^8+2a^7+2a^6+2a^5+2a^4+2a^3+a^2+a+1}$
$\tilde{D}_1$		$\dfrac{a\left(a^2+a+1\right)}{a^3+a^2+a+1}$	$\dfrac{a\left(a^4+a^3+a^2+a+1\right)}{a^8+a^7+a^5+2a^4+a^3+a+1}$
$\tilde{D}_2$			$\dfrac{a^6\left(a^4+a^3+a^2+a+1\right)}{a^{10}+a^9+a^8+2a^7+2a^6+2a^5+2a^4+2a^3+a^2+a+1}$

Table 3.21:   weights for $k=1,2,3$ for $\hat{v}^+_{i-1/2}$

On the other hand the approach via exact cell volumes is impossible since ENO methods exist only for equidistant or stretched grids. For consistency this point of view is also assumed for the angular (equidistant) direction. Here I present the all coefficients both types of grids.

on the equidistant grid:

k	1	2	3
d_0	1	3/4	5/16
d_1		1/4	5/8
d_2			1/16

Table 3.22:   weights for $k=1,2,3$ for $\hat{v}^-_{i+1/2}$

The smoothness measurement are now for $k = 2$

$$
\begin{aligned}
\beta_0 &= \left(a\bar{v}_{i+1} - a\bar{v}_i\right)^2 \\
\beta_1 &= \left(\frac{1}{a}\bar{v}_i - \frac{1}{a}\bar{v}_{i-1}\right)^2
\end{aligned}
\tag{3.8.26}
$$

and for $k = 3$:

$$
\begin{aligned}
\beta_0 &= Y_0^2\left(\bar{v}_i - (q+1)\bar{v}_{i+1} + \bar{v}_{i+2}\right)^2 + \left(Z_{10}\bar{v}_i + Z_{20}\bar{v}_{i+1} + Z_{30}\bar{v}_{i+2}\right)^2 \\
\beta_1 &= Y_1^2\left(\bar{v}_i - (q+1)\bar{v}_{i+1} + \bar{v}_{i+2}\right)^2 + \left(Z_{11}\bar{v}_{i-1} + Z_{21}\bar{v}_i + Z_{31}\bar{v}_{i+1}\right)^2 \\
\beta_2 &= Y_2^2\left(\bar{v}_i - (q+1)\bar{v}_{i+1} + \bar{v}_{i+2}\right)^2 + \left(Z_{12}\bar{v}_{i-2} + Z_{22}\bar{v}_{i-1} + Z_{32}\bar{v}_i\right)^2
\end{aligned}
$$

where now

β	Y	Z_1	Z_2	Z_3
0	$\dfrac{\sqrt{13}}{\sqrt{3}a^4(a^2+1)}$	$\dfrac{a^2+a+1}{a^2(a+1)}$	$-\dfrac{a^4+a^3+a^2+a+1}{a^4(a+1)}$	$\dfrac{1}{a^4(a+1)}$
1	$\dfrac{\sqrt{13}}{\sqrt{3}(a^2+1)}$	$\dfrac{a^2}{a+1}$	$\dfrac{-a^3+1}{a(a+1)}$	$-\dfrac{1}{a(a+1)}$
2	$\dfrac{\sqrt{13}a^4}{\sqrt{3}(a^2+1)}$	$\dfrac{a^5}{a+1}$	$-\dfrac{a\left(a^4+a^2+a+1\right)}{a+1}$	$\dfrac{a\left(a^2+a+1\right)}{a+1}$

Table 3.23:   smoothness indicators for $k = 3$

Note that on the equidistant grid the smoothness indicators are the same for each method, this does not hold true on a stretched grid.

When using the original coefficients in an one dimensional simulation energy is not preserved in the long run, over the first 100 days it increases or decreases depending on the initial condition. With the other set of coefficients all the conserved variables are stable.

(a) interpolation of the primitive function   (b) interpolation of the flux function
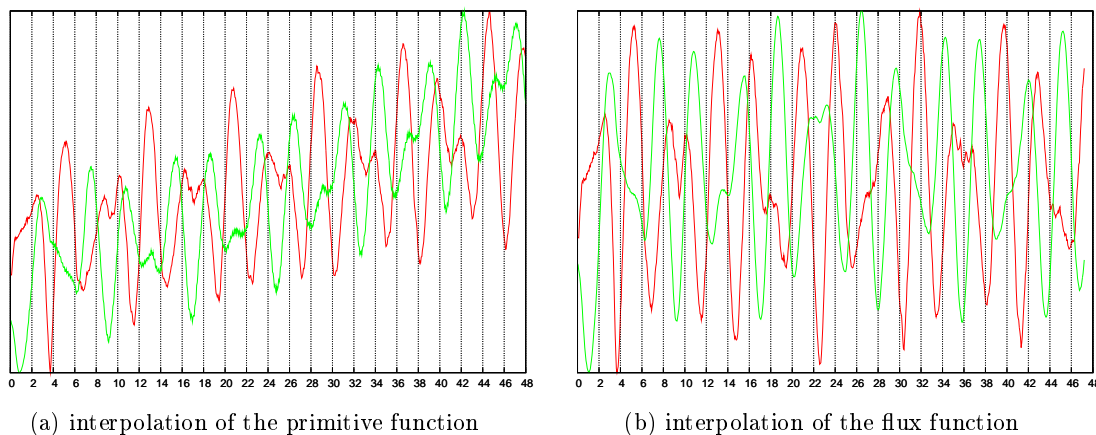
Figure 3.8.1:   effects of different ENO coefficients

Variation of radius (red) and total energy (green) during the first 48 days in one dimension.

3.8.4 Marquina Flux Splitting and Entropy Fix

When the states differ greatly across the cell wall using a single intermediate state in the transformation as presented above may add subtle spurious features to the solution. As an alternative [DM 1996] recommended obtaining the wall flux from a splitting procedure based on fluxes computed separately from the left and from the right side. At so called sonic points, i.e. a place where a characteristic velocity changes sign, it is possible to have a stationary expansion shock with a discontinuous jump in value. If this jump where smoothed out even slightly it would break up into an "expansion fan" which is the desired physical solution.

If there is a nearby sonic point add high order dissipation to the calculation of $\hat{f}_{i+1/2}$ being extremely small if the solution is locally smooth but large enough to break up an expansion shock. Using this flux splitting method fixes the problematic cases cases in [FMDO 1998] whereon the following presentation is based. Replacing the choice for the one state $U_{i+1/2}$ by two states when interpolating from the left and from the right leads to the definition of $J^L_{i+1/2}$ and $J^R_{i+1/2}$. Now there are two eigensystems for each $r_{i+1/2}$ the upwind direction is chosen to be

1. only to the right if $\lambda^L_{i+1/2} > 0$ and $\lambda^R_{i+1/2} > 0$. Fluxes are interpolated to the right using $J^L_{i+1/2}$. The fluxes in the $J^R_{i+1/2}$ scheme are set to zero.

2. only to the left if $\lambda^L_{i+1/2} < 0$ and $\lambda^R_{i+1/2} < 0$. Fluxes are interpolated to the left using $J^R_{i+1/2}$. The fluxes in the scheme are set to zero $J^L_{i+1/2}$.

3. When the signs of the eigenvalues differ a sonic point is nearby and an entropy fix (see below) with a dissipation coefficient $\alpha_{i+1/2} = \max\left(\left|\lambda^L\right|, \left|\lambda^R\right|\right)$ is applied. In the computation of $\hat{f}^L_{i+1/2}$ $\hat{f}^+_{i+1/2}$ is evaluated normally and $\hat{f}^-_{i+1/2} = 0$. In the computation of $\hat{f}^R_{i+1/2}$ $\hat{f}^-_{i+1/2}$ is evaluated normally and $\hat{f}^+_{i+1/2} = 0$. Thus $\hat{f}^L_{i+1/2} = \hat{f}^-_{i+1/2}$ and $\hat{f}^R_{i+1/2} = \hat{f}^+_{i+1/2}$.

3.8.4.1   Finding $U_{i+1/2}$ with Marquina Flux Splitting

Given a cell wall located at $r_{i+1/2}$ the states $U^L_{i+1/2}$ and $U^R_{i+1/2}$ can be found thus:

1. Take the upwind direction

2. Choose the divided differences of higher order by taking the one of smaller absolute value.

The divided differences are defined as[13]

$$
\begin{aligned}
D^0_j u &= u_j \\
D^1_{j+1/2} u &= \frac{u_{j+1} - u_j}{\Delta r_j} \\
D^0_j U &= \frac{D^1_{j+1/2} u - D^1_{j-1/2} u}{\Delta r_j + \Delta r_{j-1}}
\end{aligned} \tag{3.8.27}
$$

Looking for $u^L_{i+1/2}$: $k = i$ $\qquad\qquad\Big|\qquad$ Looking for $u^R_{i+1/2}$: $k = i+1$

$$
Q_0(r) = D^0_k u = u_k \tag{3.8.28}
$$

---

[13]u is a component of U

If $\left(\left|D^1_{k-1/2}u\right| < \left|D^1_{k+1/2}u\right|\right)$ then $\quad$ If $\quad$ $\left(\left|D^1_{k-1/2}u\right| \leq \left|D^1_{k+1/2}u\right|\right)$ then

$\qquad c = D^1_{k-1/2}u$, $k^* = k - 1$ $\qquad\qquad c = D^1_{k-1/2}u$, $k^* = k - 1$

else $\qquad c = D^1_{k+1/2}u$, $k^* = k$ endif $\qquad$ else $\qquad c = D^1_{k+1/2}u$, $k^* = k$ endif

$$Q_1(r) = c\,(r - r_j) \tag{3.8.29}$$

If $\quad \left(\left|D^2_{k^*}u\right| < \left|D^2_{k^*+1}u\right|\right)$ then $\qquad$ If $\quad \left(\left|D^2_{k^*}u\right| \leq \left|D^2_{k^*+1}u\right|\right)$ then

$\qquad c^* = D^2_{k^*}u$ $\qquad\qquad\qquad\qquad\qquad c^* = D^2_{k^*}u$

else $\qquad c^* = D^2_{k^*+1}u$ endif $\qquad$ else $\qquad c^* = D^2_{k^*+1}u$ endif

$$Q_2(r) = c^*\,(r - r_{k^*})\,(r - r_{k^*+1}) \tag{3.8.30}$$

In either cases $u_{i+1/2}$ is given by

$$u_{i+1/2} = Q_0\left(r_{i+1/2}\right) + Q_1\left(r_{i+1/2}\right) + Q_2\left(r_{i+1/2}\right) \tag{3.8.31}$$

With that states for $U^L_{i+1/2}$ and $U^R_{i+1/2}$ one can find the corresponding Jacobians $J^L_{i+1/2}$ and $J^R_{i+1/2}$ and their associated eigensystems.

3.8.4.2 WENO-Roe Discretisation

Interpolating the fluxes to $r_{i+1/2}$ to get $\hat{f}_{i+1/2}$ is done via defining a primitive function H the goal being to calculate which then gives. Again divided differences are used.

If $\qquad \left(\lambda_{i+1/2} > 0\right)$ then

$\qquad\qquad k = i$

else $\qquad k = i + 1$ endif

$$Q_1(r) = \left(D^1_k H\right)\left(r - r_{i+1/2}\right) \tag{3.8.32}$$

If $\qquad \left(\left|D^2_{k-1/2}H\right| < \left|D^2_{k+1/2}H\right|\right)$ then

$c = D^2_{k-1/2}H$, $k^* = k - 1$

else $\qquad c = D^2_{k+1/2}u$, $k^* = k$ endif

$$Q_2(r) = c\left(r - r_{i-1/2}\right)\left(r - r_{i+1/2}\right) \tag{3.8.33}$$

If $\qquad \left(\left|D_{k^*}^3 H\right| < \left|D_{k^*+1}^3 H\right|\right)$ then

$$c^* = D_{k^*}^3 H$$

else $\qquad c^* = D_{k^*+1}^3 H$ endif

$$Q_3(r) = c^*\left(r - r_{k^*-1/2}\right)\left(r - r_{k^*+1/2}\right)\left(r - r_{k^*+3/2}\right) \tag{3.8.34}$$

At last calculate

$$f_{i+1/2} = H'\left(r_{i+1/2}\right) = Q_1'\left(r_{i+1/2}\right) + Q_2'\left(r_{i+1/2}\right) + Q_3'\left(r_{i+1/2}\right) \tag{3.8.35}$$

3.8.4.3   Entropy Fix

Now consider two primitive functions H^+ and H^- and compute a divided difference table for each of them. The first divided differences at point r_i are

$$D_i^1 H^{\pm} = \frac{1}{2} f\left(r_i\right) \pm \frac{1}{2}\alpha_{i+1/2} u\left(r_i\right) \tag{3.8.36}$$

with $\alpha_{i+1/2}$ as defined above (in 3.). Normally the first order difference of the primitive is the value of the flux function at the cell centres, i.e. $D_i^1 H = f\left(r_i\right)$.

- For H^+ set $k = i$, replace H with H^+ and determine Q_1, Q_2, Q_3 and $\hat{f}_{i+1/2}^+$ using the algorithm above.

- For H^- set $k = i + 1$, replace H with H^- and determine Q_1, Q_2, Q_3 and $\hat{f}_{i+1/2}^-$ using the algorithm above.

- Then
$$\hat{f}_{i+1/2} = \hat{f}_{i+1/2}^+ + \hat{f}_{i+1/2}^- \tag{3.8.37}$$
is the numerical flux function with added high order dissipation. This choice eliminates entropy violating expansion shocks.

3.9   Updating

In the update process the change of the cell volumes due to the moving grid must be taken into account. Since the main purpose is the conservation of variables the following straightforward method is used to approximate the divergence:

$$\begin{aligned}
U_{i,j}^{n+1} \cdot V_i^{n+1} \;=\;\; & U_{i,j}^n \cdot V_i^n - \Delta t \cdot \\
& \left[\left(A_{i+\frac{1}{2}}\tilde{F}_{i+\frac{1}{2},j} - A_{i-\frac{1}{2}}\tilde{F}_{i-\frac{1}{2},j}\right) + \right. \\
& \left. + \left(B_i\tilde{F}_{i,j+\frac{1}{2}} - B_i\tilde{F}_{i,j-\frac{1}{2}}\right) + S \cdot V_i^n\right]
\end{aligned}$$

Due to the sheer size of the star the numbers involved are also large, the computation is more stable if the approximated values (equations (3.2.4) and (3.2.6)) are used for the cell volume and the lateral surface instead of the exact results ((3.2.3) and (3.2.5)). Thereby this equation can be written as

$$
\begin{aligned}
U_{i,j}^{n+1} = {} & U_{i,j}^{n} \frac{\widetilde{V}_{i}^{n}}{\widetilde{V}_{i}^{n+1}} - \Delta t \cdot \\
& \left[\left(\frac{\widetilde{A}_{i+\frac{1}{2}}}{\widetilde{V}_{i}^{n+1}} \tilde{F}_{i+\frac{1}{2},j} - \frac{\widetilde{A}_{i-\frac{1}{2}}}{\widetilde{V}_{i}^{n+1}} \tilde{F}_{i-\frac{1}{2},j} \right) + \right. \\
& \left. + \frac{B_i}{\widetilde{V}_{i}^{n+1}} \left(\tilde{F}_{i,j+\frac{1}{2}} - \tilde{F}_{i,j-\frac{1}{2}} \right) + S \frac{\widetilde{V}_{i}^{n}}{\widetilde{V}_{i}^{n+1}} \right]
\end{aligned}
$$

which reduces nicely to

$$
\begin{aligned}
U_{i,j}^{n+1} = {} & U_{i,j}^{n} \left(\frac{r_i^n}{r_i^{n+1}} \right)^2 \frac{\Delta r_{i-\frac{1}{2}}^n}{\Delta r_{i-\frac{1}{2}}^{n+1}} - \Delta t \cdot \\
& \left[\frac{1}{\Delta r_{i-\frac{1}{2}}^{n+1}} \left(\left(\frac{r_{i+\frac{1}{2}}^n}{r_i^{n+1}} \right)^2 \tilde{F}_{i+\frac{1}{2},j} - \left(\frac{r_{i-\frac{1}{2}}^n}{r_i^{n+1}} \right)^2 \tilde{F}_{i-\frac{1}{2},j} \right) + \right. \\
& \left. + d_{fac} \frac{\pi r_i^n}{2\Delta\varphi \left(r_i^{n+1}\right)^2} \left(\tilde{F}_{i,j+\frac{1}{2}} - \tilde{F}_{i,j-\frac{1}{2}} \right) + S \left(\frac{r_i^n}{r_i^{n+1}} \right)^2 \frac{\Delta r_{i-\frac{1}{2}}^n}{\Delta r_{i-\frac{1}{2}}^{n+1}} \right]
\end{aligned}
$$

For the momentum equation the difference between $\nabla \cdot (p \cdot Id)$ and ∇p is included in the source term. d_{fac} is the dilation factor of the grid.

Chapter 4

Simulations

4.1 One Dimensional Simulations

One dimensional simulations were not only necessary to obtain a start model for two dimensional simulations (see 3.1), they were also used for comparison of 1D and 2D simulations and for testing the grid refinement.

(a) 2D   (b) 1D
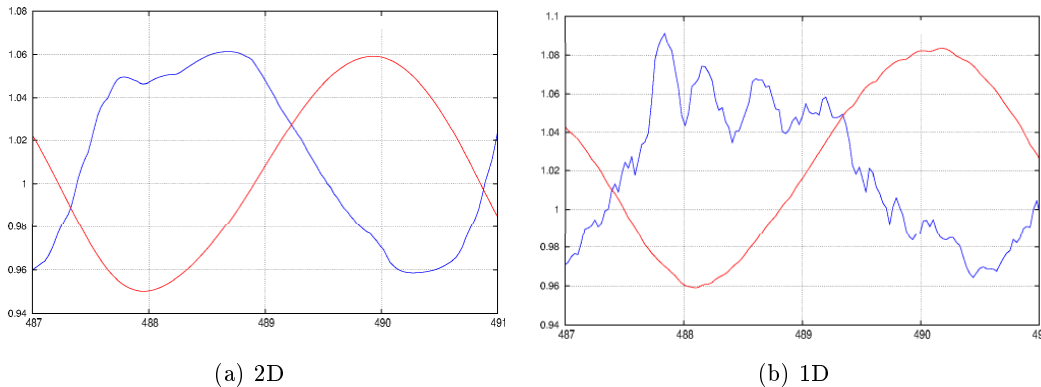
Figure 4.1.1:   pulsation in two and one dimensions

In figure 4.1.1 are plotted the lightcurve (blue line) and the variation of the radius (red line) during the 9-th period after the preliminary 1D simulation. Whereas in 2D both curves are smooth, this is not the case in 1D, there the pulsation velocity varies, so that there are artificial humps even in the radius. Since there is no angular direction, convection cannot set in and perturbations that may occur in the unresolved H-ionisation zone cannot escape in that direction. Some perturbations are even visible at the bottom of the computational domain, where they are reflected on the closed boundary (figure 4.1.3). Note that the variation of the radius is less in 2D than in 1D (11% instead of 12%) as the pulsation is damped by convection, this effect sets in as soon as convection starts after one to two periods and is then stable.

As is to be expected there is also more radiation emitted in the purely radiative 1D-model
(Figure 4.1.2).
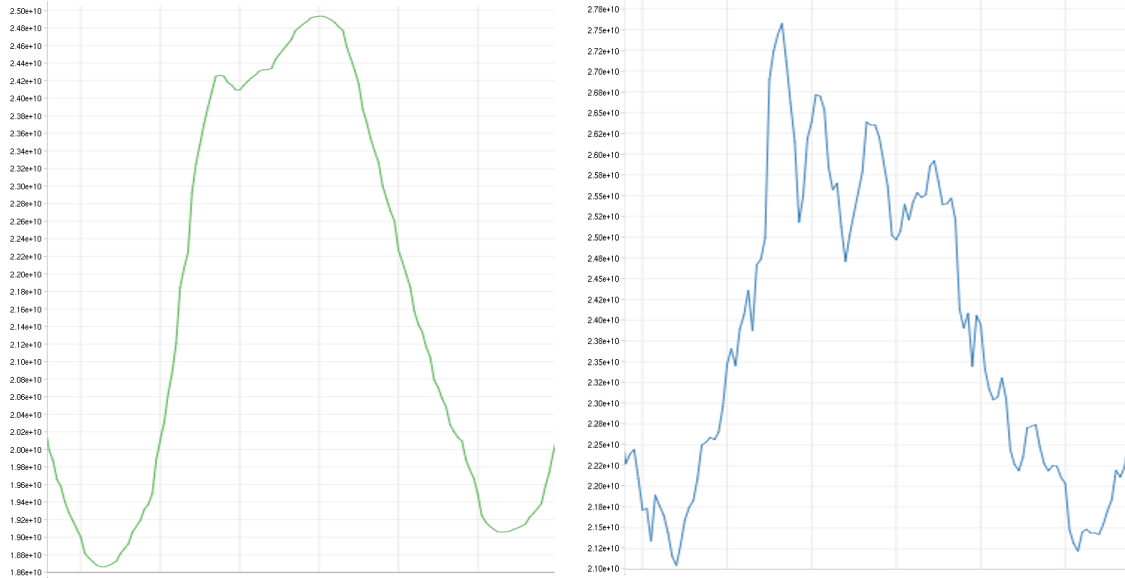
Figure 4.1.2:   lightcurve in two and one dimensions
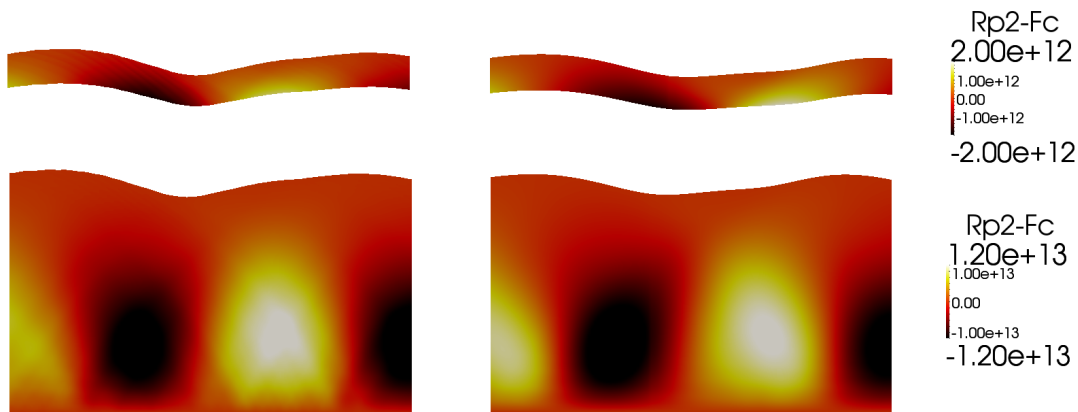
Figure 4.1.3:   convective flux $\frac{I_r}{\rho}\left(\rho h\right)$ in one and two dimensions

That these structures in the light curve are artificial can also be seen by grid refinement.
When the H-ionisation zone is sufficiently resolved, the curves are smooth (figure 4.1.4).
This simulation used a grid refinement factor of 7.[1] Note that both simulations are only
~ 100 days old and the fundamental mode and the overtone are still visible in the curves.
The age of these simulations is just between the first and the second Fourier-analysis in
figure 3.1.2 in section 3.1.

---

[1] for the grid refinement procedure see section 4.4
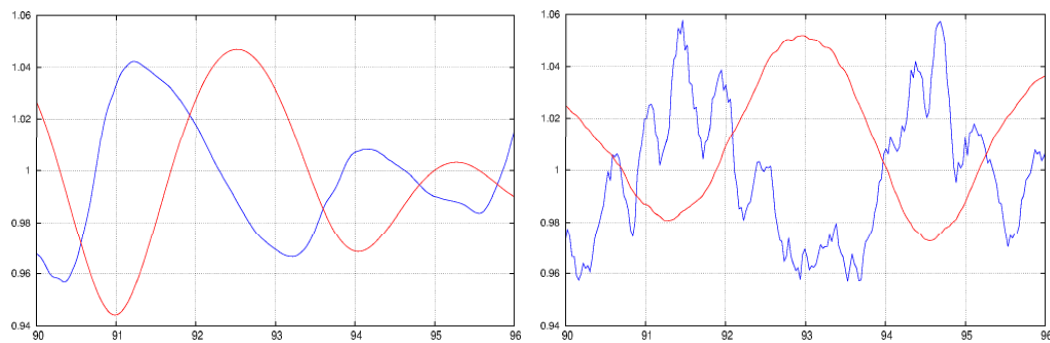
Figure 4.1.4:   lightcurves obtained with and without grid refinement

Since the opacity tables are not sufficiently exact for lower temperatures we tried artificial diffusivities in order to compute still larger regions up to 3700K. With artificial diffusivities the fundamental mode was reached in only 60 to 80 sound crossing times instead of 140 to 160, but still both curves where rather jagged for these low temperatures.

4.2   Long Time Study of the He-Ionisation Zone in 2D

A simulation on the coarse grid was carried out for about 12 periods. Convection set in after the first period. For data analysis the simulation was broken up into single periods, from one radial maximum to the next. In order not to loose context a part of the previous and the following period was added to each, leading to 10 extended periods to analyse. In each period one can observe the same pattern in various output parameters.

Figure 4.2.1 shows stream lines coloured by momentum plotted over the convective flux (equation 4.2.6) during the 8-th period and depicts the upper part of the computational domain. In the first frame the star is fully expanded and you can see the remnants of an old plume that moves downwards and will eventually almost disappear in the last frame. From the third picture onwards the formation of another plume is clearly visible, it also starts to travel towards the centre of the star. In the last frame the streamlines already indicate the formation of the next plume that will appear during the next period.
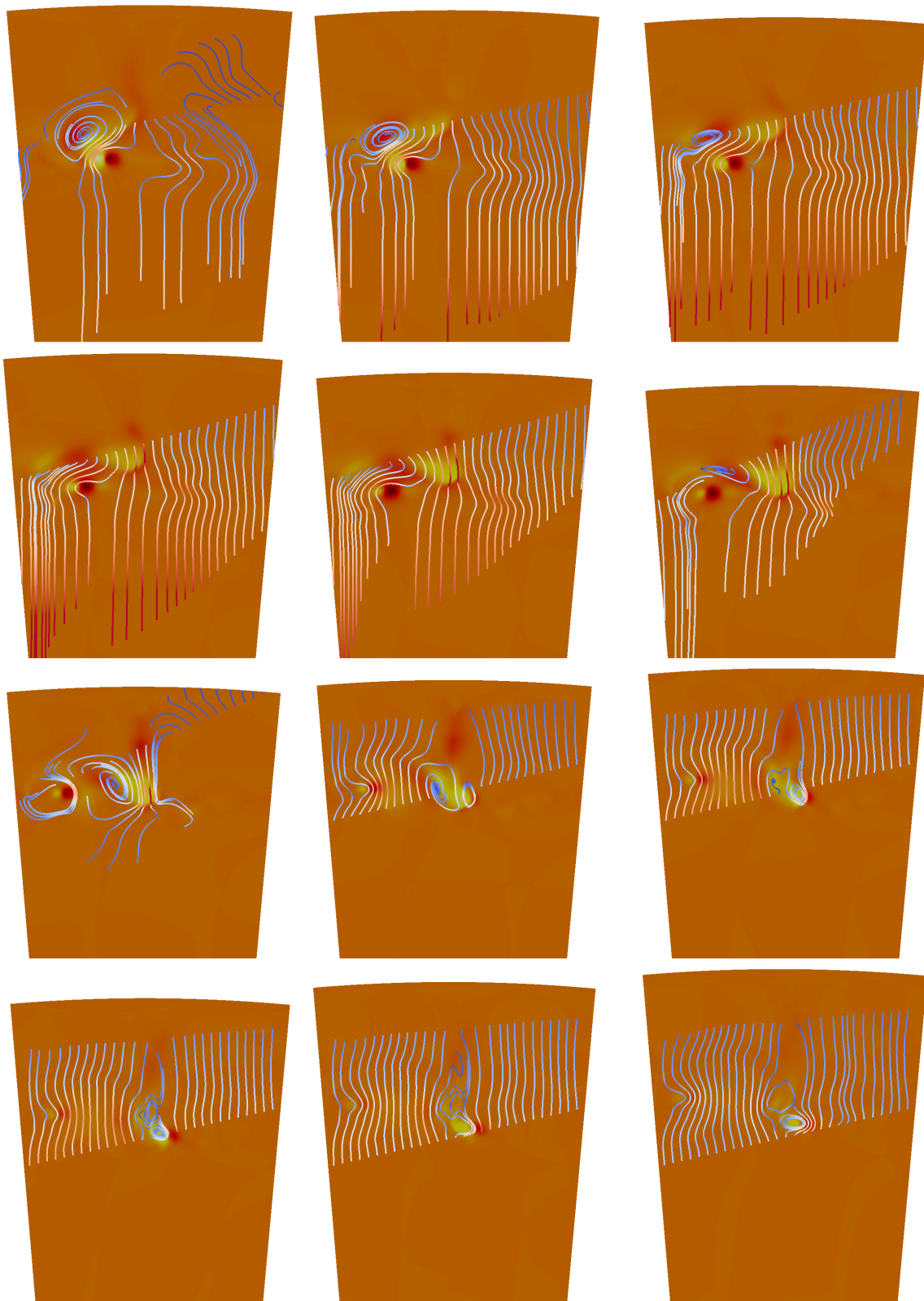
Figure 4.2.1:   convective flux
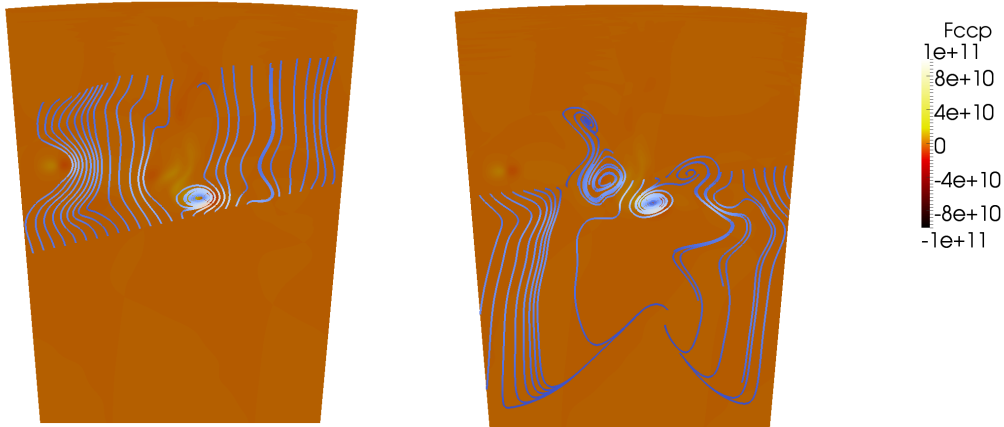
Figure 4.2.2:   convective flux

Horizontal averages and horizontal sums. For better comparison of the different periods horizontal averages of various parameters were considered. These were also interpolated to mass coordinates, and then a time-average over each period was computed. The „average period" in figure 4.2.3 is simply the average off all periods and is plotted against an averaged radius.

(a) period 8

(b) average period
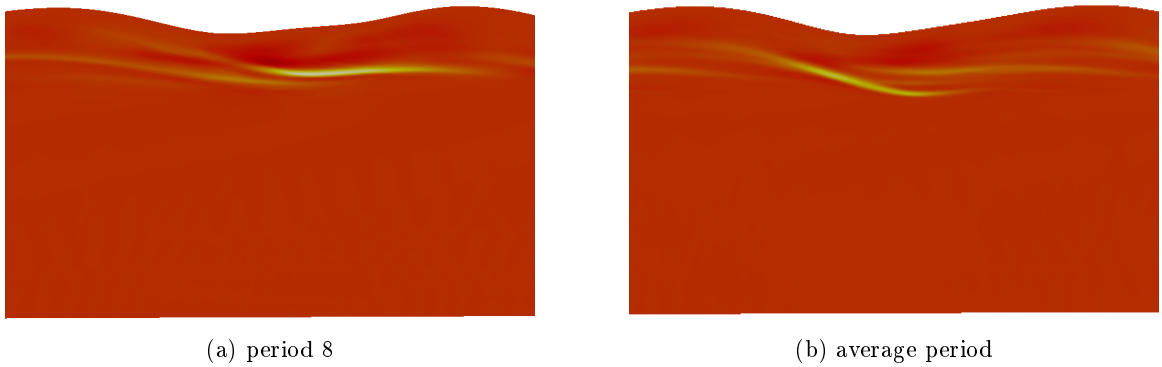
Figure 4.2.3:   horizontal sum of the convective flux F_c'

abscissa: time; ordinate: radius

For the polar grid it is important to distinguish between horizontal sums and averages, since the latter depend on the radius. In the following $\overline{\cdots}$ denotes die horizontal sum of any given quantity, i.e. $\int_{-\varphi_{tot}/2}^{-\varphi_{tot}/2} \ldots d\varphi$, and $\ldots_0$ the horizontal average thereof. Omitting the viscous fluxes the horizontal sum of the total energy equation (2.1.16) on page 29 can be expressed as

$$\frac{\partial}{\partial t}\left(\overline{e}\right) = -\frac{\partial}{\partial r}\left(\overline{F_c} + \overline{F_k} + \overline{F_r}\right) + \overline{E_B} + \overline{ED} \qquad (4.2.1)$$

where

$$F_k = -\frac{I_r}{\rho}\frac{|I|^2}{2\rho} \qquad (4.2.2)$$

is the kinetic flux,

$$F_c = -\frac{I_r}{\rho}\left(\rho h - (\rho h)_0\right) \tag{4.2.3}$$

is the convective flux and F_r is the radiative flux as defined in (2.2); the total flux is

$$F_T = F_c + F_k + F_r \tag{4.2.4}$$

$E_B = -g\left(\rho - \rho_0\right)\frac{I_r}{\rho}$ represents work done by buoyancy and $ED = -\frac{I_r}{\rho}\rho_0 g + \frac{\partial(r^2 I_r/\rho(\rho h)_0)}{r^2 \partial r}$. The relative role of buoyancy and pressure in the dynamics of convection can be clarified by a conservative equation of the mechanical energy in addition to (4.2.1) for the total energy. Such an equation is obtained by forming a scalar product of the momentum equation (2.1.14) on page 29 with the velocity vector. The horizontal sum of that mechanical energy equation is then

$$\frac{\partial}{\partial t}\left(\overline{\frac{I^2}{2\rho}}\right) = -\frac{\partial}{\partial r}\left(\overline{F_k} + \overline{F_p}\right) + \overline{E_B} + \overline{E_P} + \overline{HD} \tag{4.2.5}$$

where $F_p = -\frac{I_r}{\rho_r}\left(p - p_0\right)$ is the acoustic or „pressure" flux, $E_p = -\left(p - p_0\right)\nabla \cdot I$ represents work done by pressure and $HD = -\frac{I_r}{\rho}\left(\frac{\partial p_0}{\partial r} + \rho_0 g\right)$. Each term here is an energy per unit time and volume, on the left hand is the time derivative of the kinetic energy. A similar analysis was done in [HTM 1984]. Here some extra terms e.c. HD and ED appear since because of the pulsation it can never be assumed that $(I_r)_0 = 0$.

Since we want to separate the effects of convection and pulsation we now substitute $\frac{I_r}{\rho_r} - \frac{\bar{I}_r}{\bar{\rho}_r}$ for $\frac{I_r}{\rho_r}$ and look at

$$F_c' = u_{conv}^1 \cdot \left(h - \bar{h}\right) \tag{4.2.6}$$

$$F_k' = u_{conv}^1 \cdot \left(\frac{|u_{conv}|^2}{2}\rho\right) \tag{4.2.7}$$

instead of F_c and F_k where $u_{conv} = \left(u_{conv}^1/u_{conv}^2\right) = \left(\frac{I_r}{\rho} - \frac{(I_r)_0}{\rho_0}, \frac{I_\varphi}{\rho_\varphi}\right)$.

(a) period 6   (b) period 8
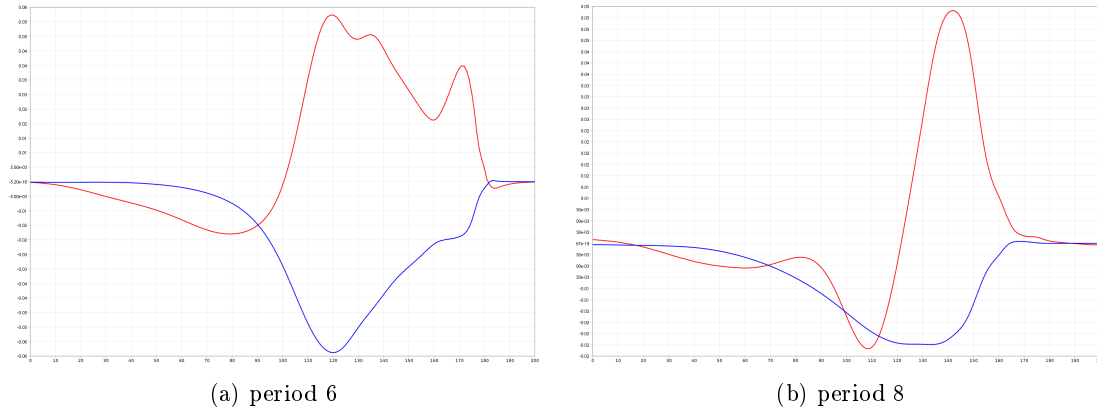
Figure 4.2.4:   flux averaged over one period

red line: convective flux; blue line: kinetic flux; both as fractions of the total flux.

When observing the convective flux in figure 4.2.1 over time one realises that it is at a maximum during full contraction, while during expansion one sees the new convection cells forming at the top and the remnants of the „old" ones, when the star contracts these almost merge into one. In figure 4.2.3 the horizontal sums over one period and over an average period, are depicted. This pattern is repeated in each period, though the extent may vary. There are always two centres of convection (yellow line) visible, sometimes three. The average flux over one period in the He-ionisation zone is depicted in figure 4.2.4.

Work and work-integrals. At each moment we compute

$$PdVu_0^1 = \frac{\partial \frac{(I_r)_0}{\rho_0}}{\partial r} \frac{p}{\rho} \tag{4.2.8}$$

$$PdVu_{conv}^1 = \frac{\partial u_{conv}^1}{\partial r} \frac{p}{\rho} \tag{4.2.9}$$

and

$$PdVu_{conv}^2 = \frac{\partial u_{conv}^2}{\partial r} \frac{p}{\rho} \tag{4.2.10}$$

where the horizontal averages $()_0$ are computed as above.
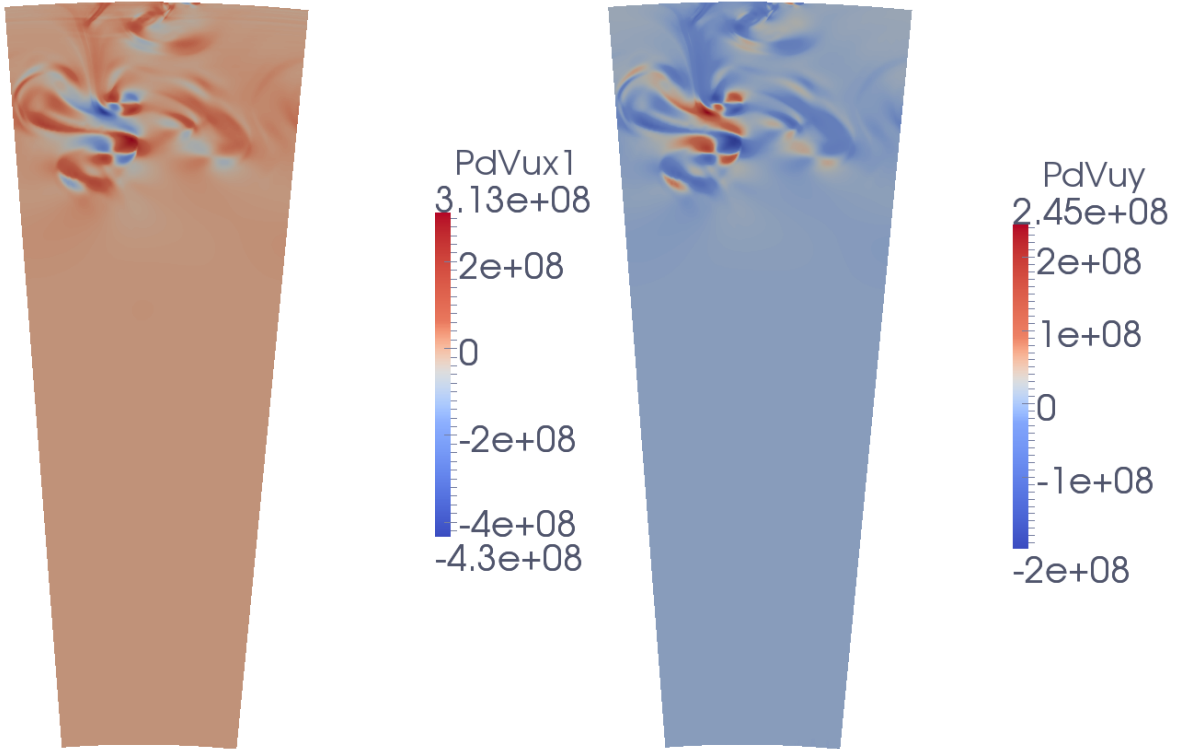
Figure 4.2.5:   work at one moment

The horizontal sums $\overline{PdVu_0^1}$, $\overline{PdVu_{conv}^1}$ and $\overline{PdVu_{conv}^2}$ over the computational domain are the so called work-integrals. When comparing the values of $PdVu_{conv}^1$ and $PdVu_{conv}^2$ at any given moment to the horizontal averages and to $PdVu_0^1 \sim \overline{PdVu_0^1}$ at the same time one realises a striking difference in the magnitudes:

- At any moment the local perturbational parts $PdVu^1_{conv}$ and $PdVu^2_{conv}$ (figure 4.2.5) are larger than the radial part $PdVu^1_0$ (first frame in figure 4.2.6).

- For the work integrals it is just the other way round: $\overline{PdVu^1_0}$ is larger by a factor ~ 10. (figure 4.2.6), in the horizontal averages the perturbational parts cancel each other out.

- the averages over one period are dominated by the convective part $PdVu^1_{conv}$, while the values of $PdVu^2_{conv}$ are smaller. (figure 4.2.7)

- $PdVu^2_0$ is around zero, this it not exactly the case in each period but at least in an average period. (figure 4.2.8)
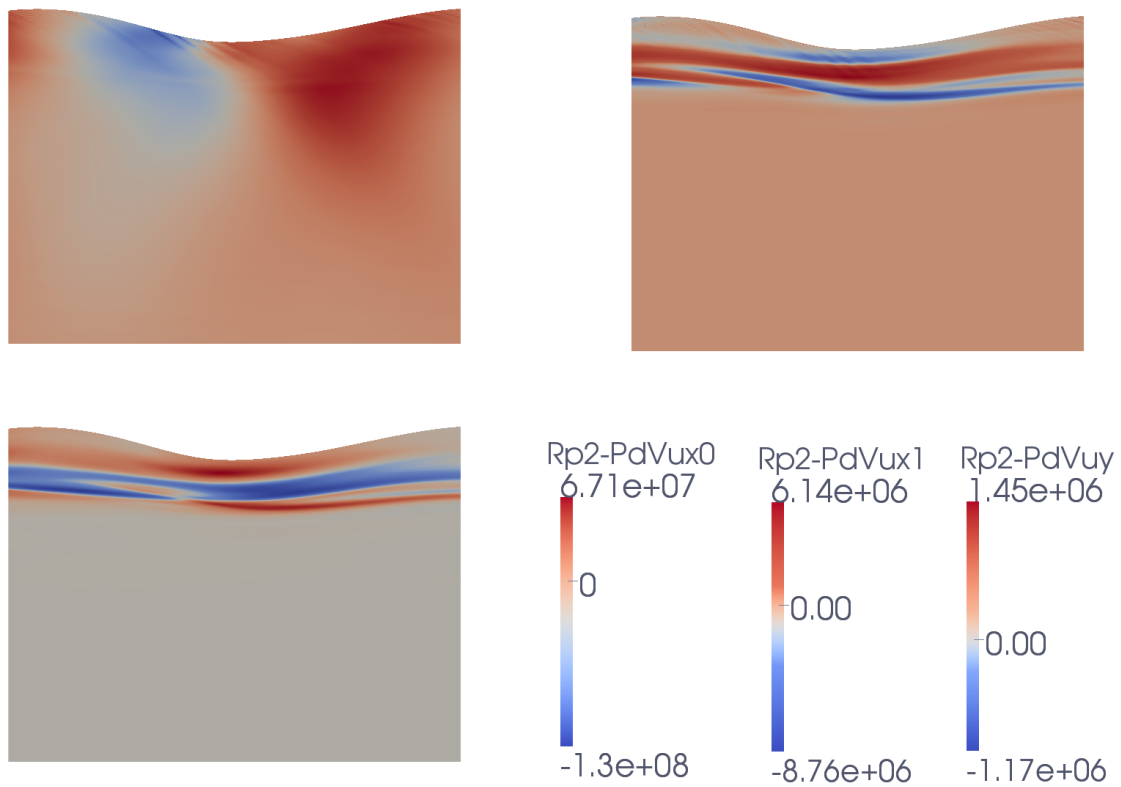
Figure 4.2.6:   work integral

(a) period 2   (b) period 6
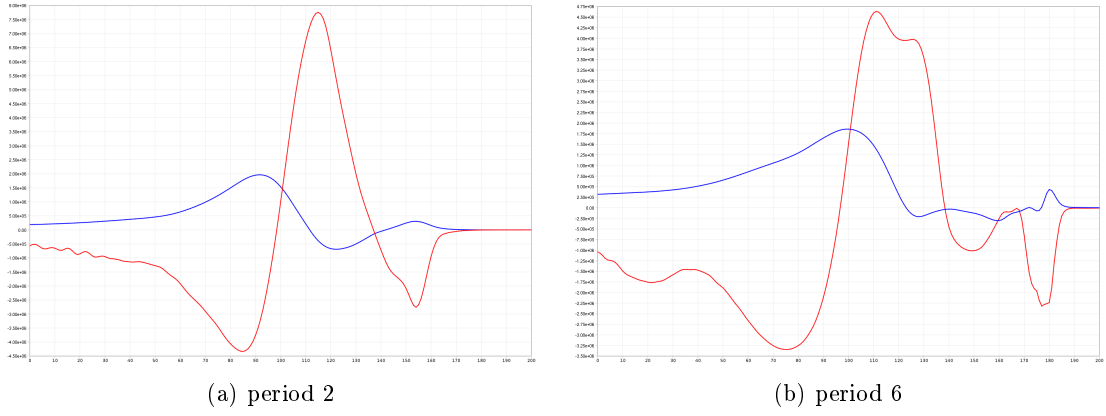
Figure 4.2.7:   average work integrals over one period

in the He-ionisation zone. Red line: $PdV u_{conv}^1$, blue line: $PdV u_{conv}^2$

(a) period 8   (b) average period
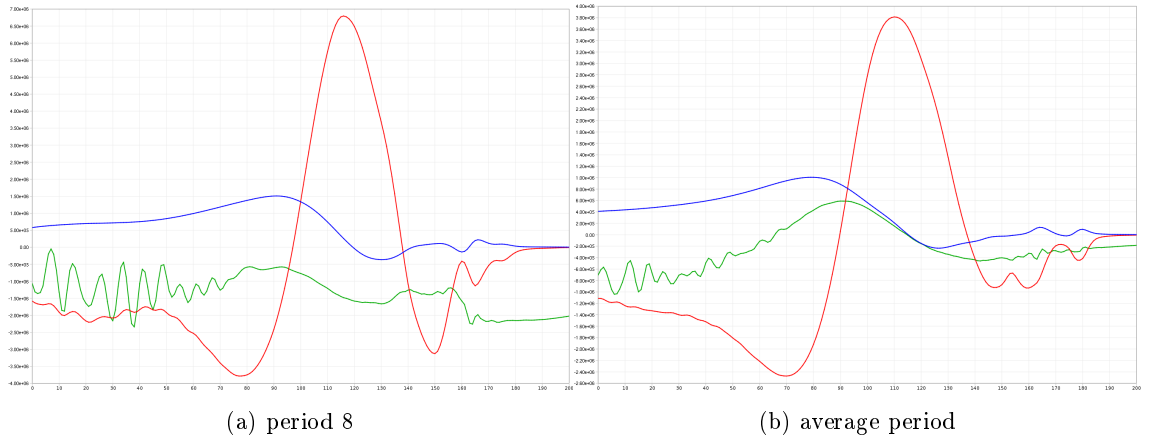
Figure 4.2.8:   average work integrals over one period

in the He-ionisation zone. Red line: $PdV u_{conv}^1$, blue line: $PdV u_{conv}^2$, green line: $PdV u_0^1$

4.2.1   Convectional Stability

The superadiabatic gradient is defined as

$$\nabla_{sa} := \nabla - \nabla_{ad} \tag{4.2.11}$$

where

$$\nabla := \frac{\partial \ln T}{\partial \ln P} = \frac{P \partial T}{T \partial P} = \frac{P}{T} \frac{\partial T / \partial r}{\partial P / \partial r} \tag{4.2.12}$$

is the actual temperature gradient and

$$\nabla_{ad} = \left(\frac{d \ln T}{d \ln P} \right)_{ad} := \frac{\Gamma_2 - 1}{\Gamma_2} = \frac{\Gamma_3 - 1}{\Gamma_1} \tag{4.2.13}$$

is the adiabatic gradient. The Schwarzschild criterion predicts convectional stability for $\nabla_{sa} < 0$ and instability for $\nabla_{sa} > 0$. ∇_{sa} is depicted at the top of figures 4.2.9 and 4.2.10, the black lines indicates $\nabla = \nabla_{ad}$.
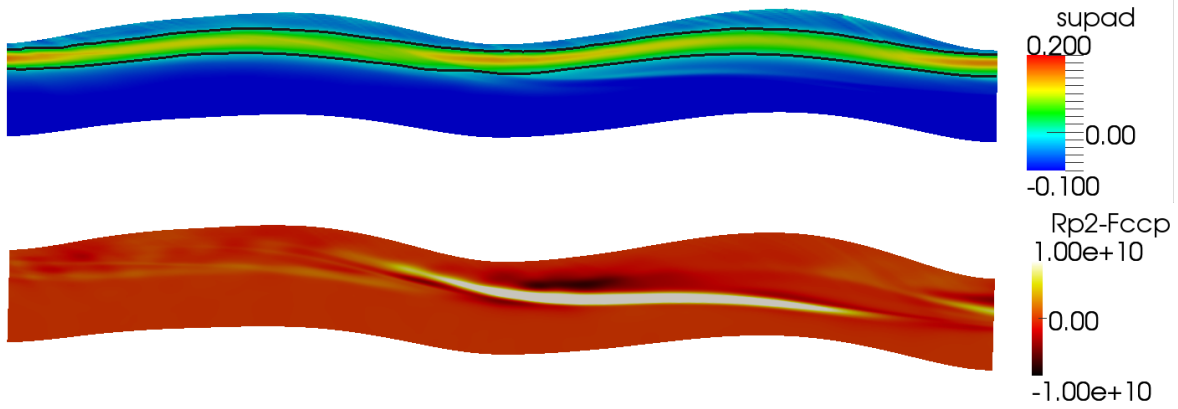
Figure 4.2.9:   He-convection in period 2
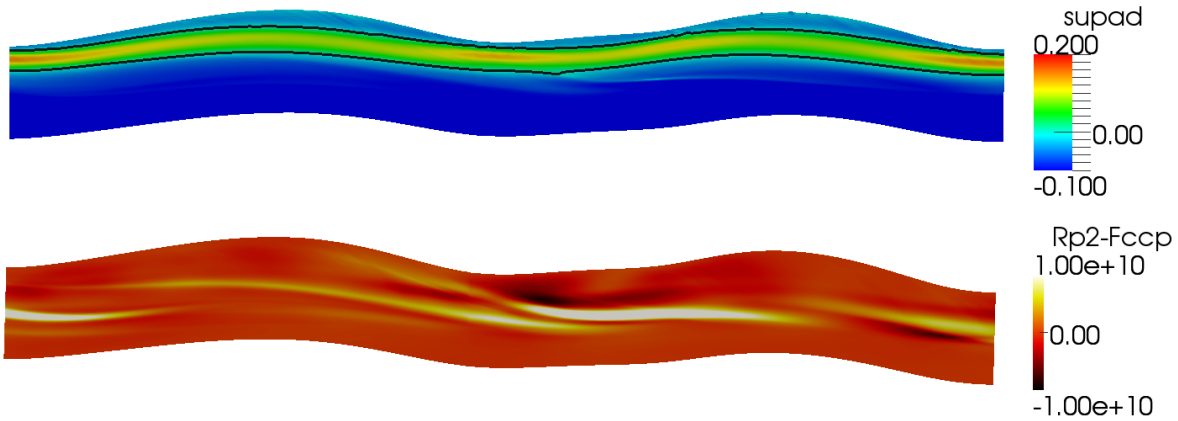
Figure 4.2.10:   He-convection in period 8

Convectional instability is strongest when the star is contracted. New plumes form at the top of the unstable realm, gain force during maximum contraction when $1 < \nabla_{sa} < 2$ and then move further down where the superadiabatic gradient always stays < 0.

4.3   The H-ionisation Zone without Grid Refinement

If only the coarse grid is used convection starts but becomes soon too large on single points as to be properly resolved at original resolution. Therefore grid refinement, subgrid scale modelling and artificial diffusivities were applied.

4.3.1   Artificial Diffusivities

Though they helped to stabilise the code they produced some unphysical effects, e.c. the H-ionisation zone started to drift towards the top when shock treatment ν_k^{shk} of (3.6.7) is used.

4.3.2   Subgrid Modelling

When using only subgrid modelling but no grid refinement the H-ionisation zone cannot be resolved. Compared to section 4.4 the convections starts only slowly and does not stably develop.
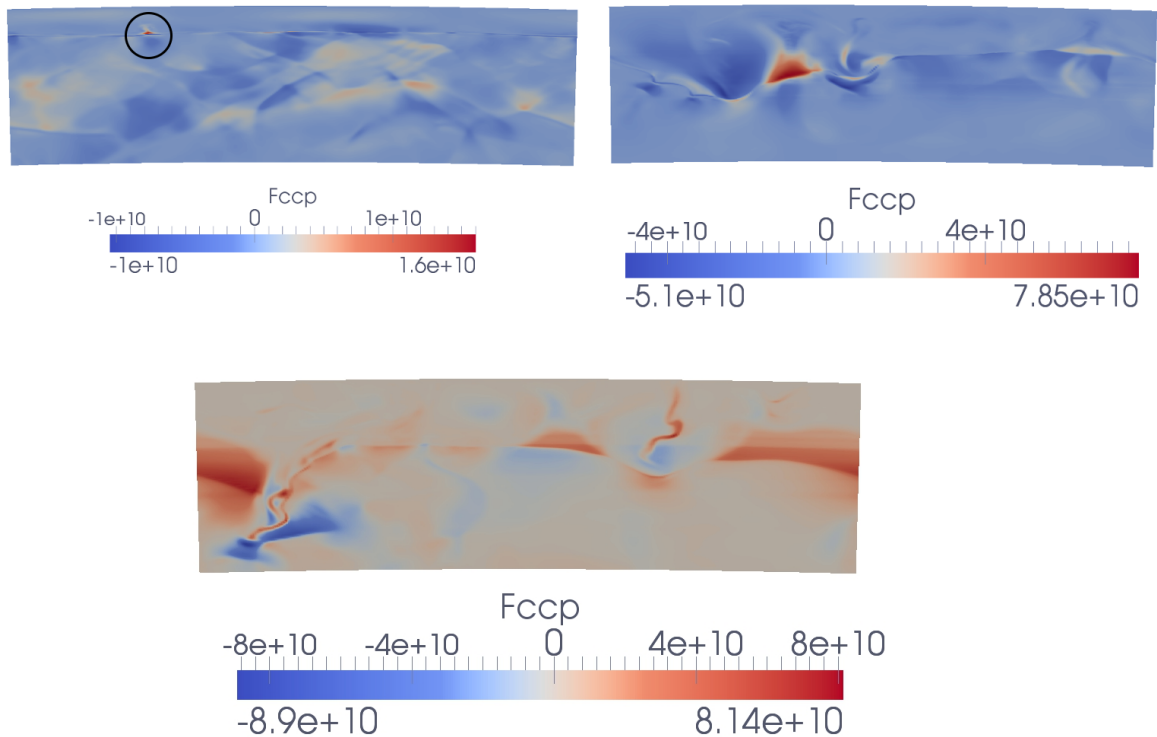
Figure 4.3.1:   subgrid modelling

4.4   High Resolution Simulation of the H-Ionisation Zone

For any study of the upper convection zone grid refinement is essential, as already pointed out in section 3.7.3. To ease the computation time requirements the grid refinement has been modified and been made partly adaptive.
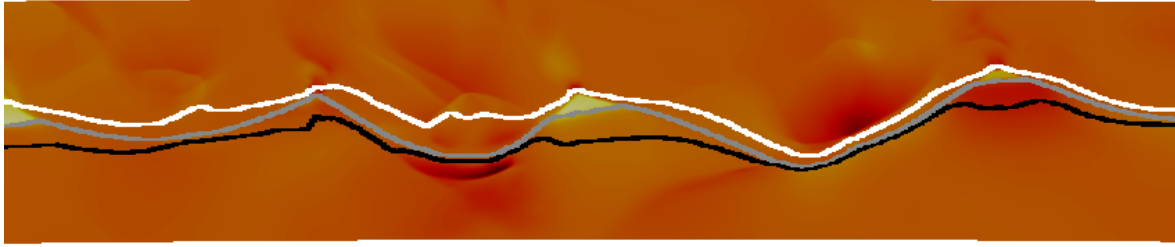
Figure 4.4.1:   opacity in the H ionisation zone

white line: 1; grey line: 10; black line: 100; plotted over the convective flux

The region of interest is at the maximum of the temperature gradient. Since it is possible that a local maximum can be found elsewhere, we also make sure that the local temperature is at least T_{eff} and the optical depth at least 100 at the lower border (black line in figure 4.4.1). First the „maximum region", that is the region where we expect to find the H-ionisation zone, and the grid refinement factors $gf(r)$ and $gf(\varphi)$ for both directions must be specified. In our case this region is always across the total angular direction. If the maximum temperature gradient is outside this region, the region has to be reset. This maximum region is surrounded by ghost cells to allow interpolation and symmetric differentiation near the boundaries. For MPI-purposes the distribution of processors on the coarse grid and the fine grid must be chosen in a different way, since the grid refinement zone is rather slim, there are more processors in angular direction there.

Starting grid refinement.   The values of the physical quantities at the coarse grid are interpolated to the fine grid, including the ghost cells. This yields the starting state for the simulation. For the first step the maximum region is used. For MPI-purposes it is determined which coarse grid data are already on the correct node and which have to be sent. This information is prestored in an array. The same is done for sending the results from the fine grid back to the coarse grid.

Structure of one grid refinement step.

- The time step for the time evolution at both grids is calculated, thus we get the number N of steps on the fine grid during one step on the coarse grid, since the calculations are limited by Δt_{rad} we get $gf(r) \leq N \leq gf(r)^2$. Since the domains are not identical, it is possible that $N < gf(r)$. In this case we still use $N = gf(r)$.

- The inner region is determined. It reaches from the top of the maximum region to n_{bot} points below ∇T_{max}, where n_{bot} is set on the coarse grid. At no time artificial structures along this bottom line could be observed, but to be on the save side it is smoothed out. To choose a top line in a similar manner leads to artifacts, in Figure 4.4.2 on page 91 such a top boundary was still used, and no longer in Figure 4.4.3 on

page 91. Note that in all figures all values outside the inner zone are only interpolated from the coarse grid.
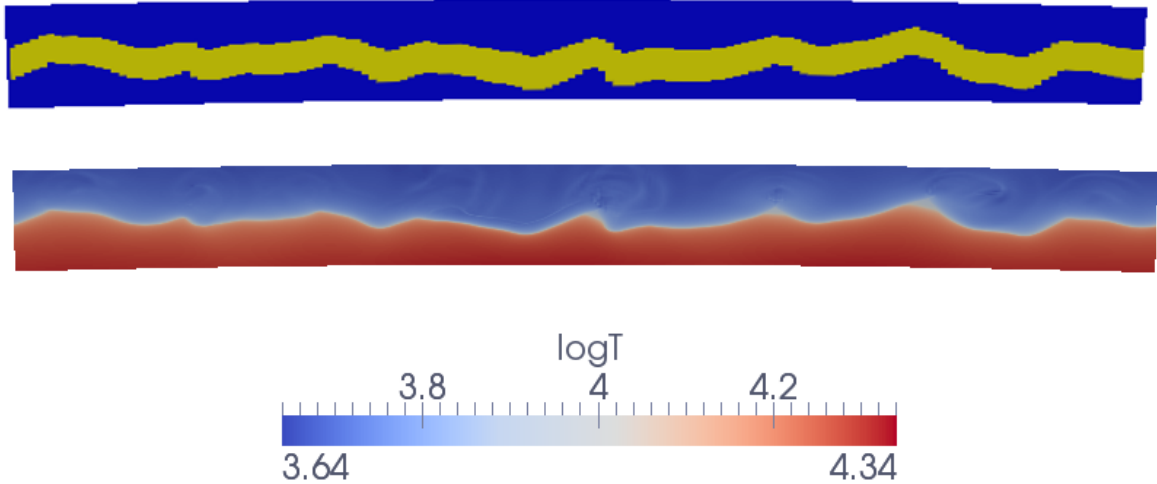
Figure 4.4.2:   grid refinement with upper limit
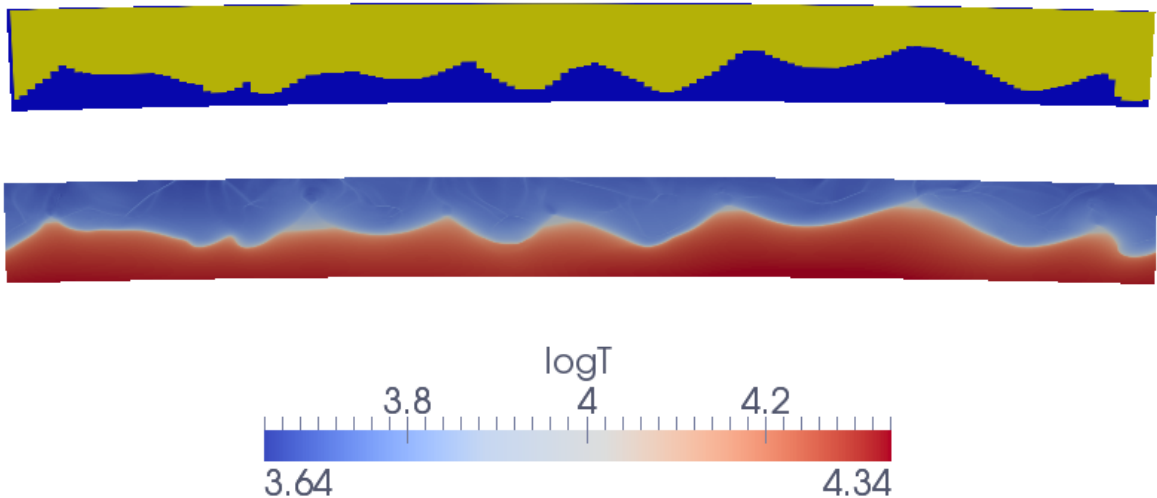
Figure 4.4.3:   grid refinement without upper limit

- The data on the coarse grid from time step n and $n + 1$ are both sent to the proper nodes.

- Now the Runge-Kutta steps on the fine grid can be performed in exactly the same way as on the coarse grid. At the beginning of each step time interpolation yields the values in the ghost cells at the top and bottom (blue region in Figure 4.4.2 on page 91 and Figure 4.4.3 on page 91) of the grid refinement zone. In angular direction they are supplied by periodic continuation.

- After the last grid refinement step the data are projected back to the coarse grid in a conservative way.
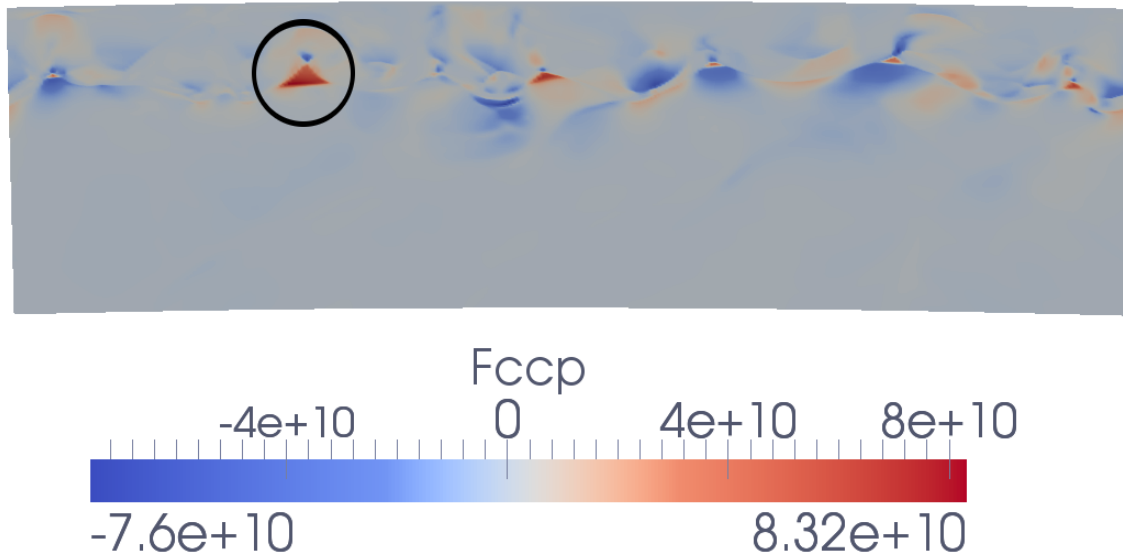
Figure 4.4.4:   convective flux in the H-ionisation zone
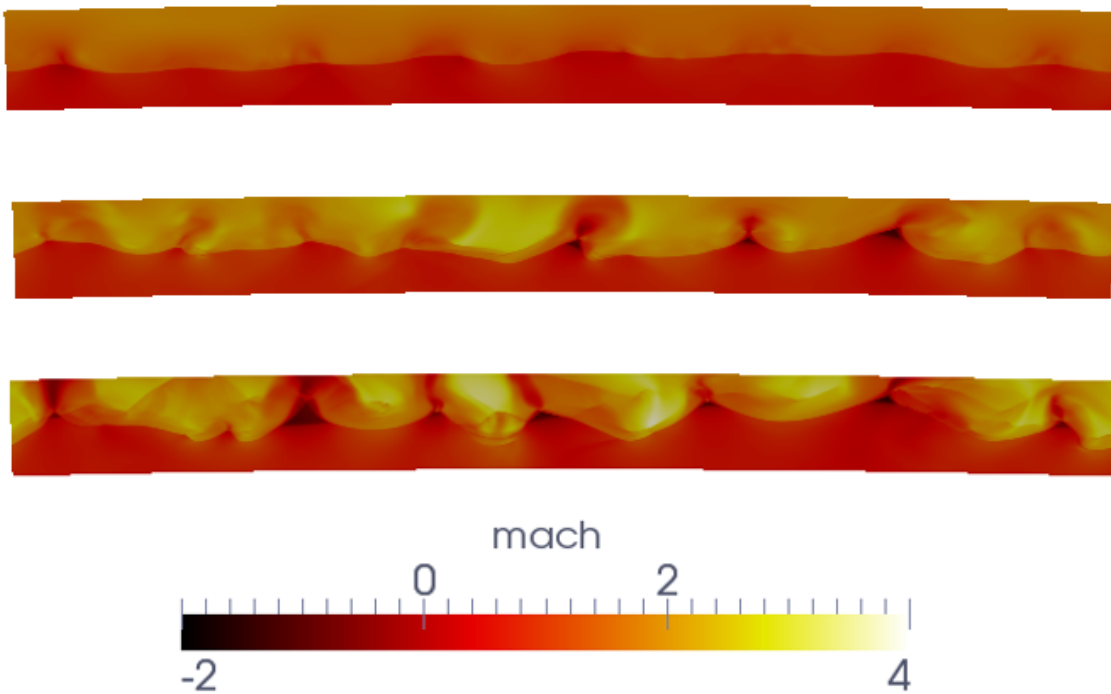
Figure 4.4.5:   Mach numbers in the upper convection zone

Resetting the maximum grid refinement zone. If it becomes necessary or convenient to move

the grid refinement zone, this can be done without dismissing the previous calculations. The old values are then copied and new values are interpolated where needed.

For this two dimensional simulation 3x4 additional grid points on each cell were used in addition to subgrid modelling. The resulting resolution is from $0.32Mm$ to $0.80Mm$ in radial direction, in the critical region it is $0.66Mm$ and $1.16Mm$ in angular direction, leading to an aspect ratio of $1 : 1.8$. But when comparing to figure 3.7.5 one has to admit that there are only 2 to 3 points to resolve the temperature gradient.

Figure 4.4.4 is taken from to coarse grid and depicts the same area as in figure 4.3.1, the simulation is as old as in the first frame figure 4.3.1. In both figures we see the same maximum (marked by a circle), but not only is the convective flux already greater by a factor 5, there are also more convection cells.

In figure 4.4.5 the development of the Mach numbers is depicted. In figure 4.4.6 we see the change in velocity for incoming material. In the frames (b) and (d) the radius is plotted from left to right. Coming from the outside of the star (right) the fluid velocity first drops and then the material is reaccelerated where the H-ionisation takes place. When comparing it to the sound velocity behind the H-ionisation front (d) one realises that difference in fluid velocities is ~ 1 Mach.
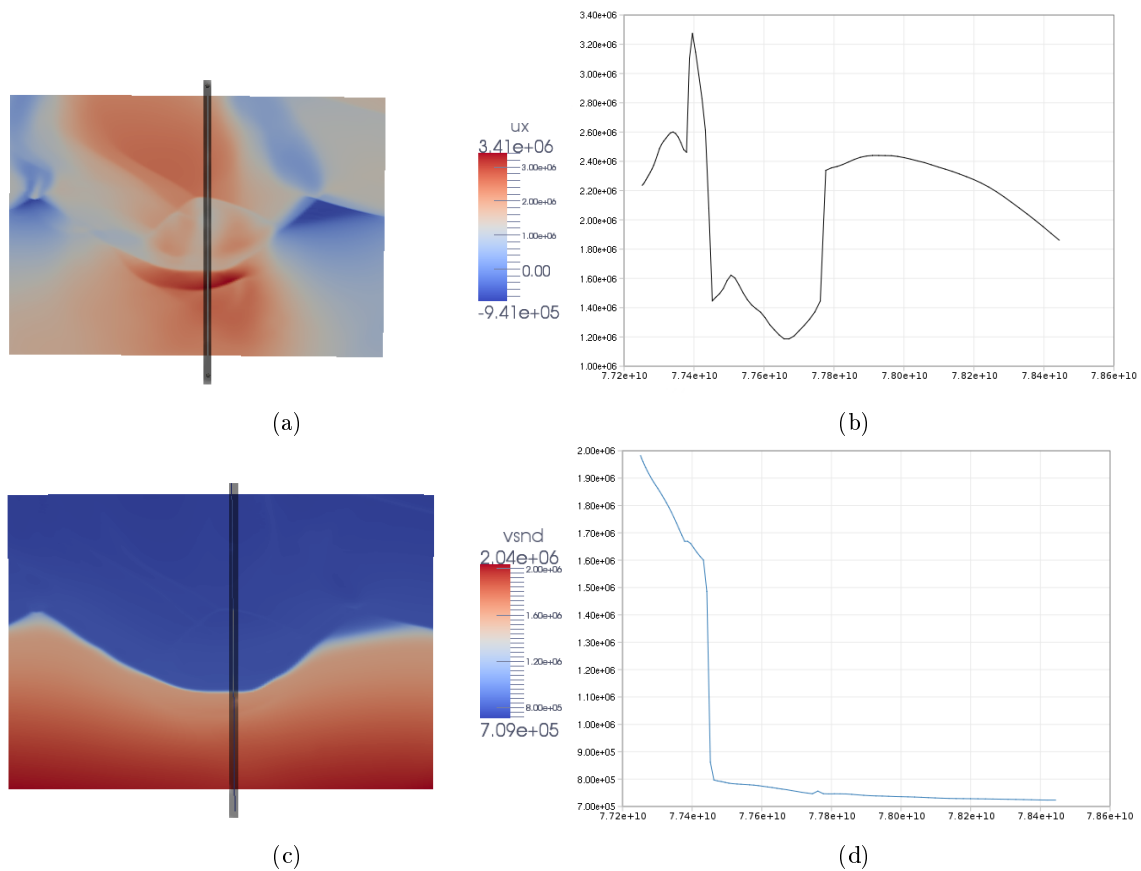
Figure 4.4.6:   acceleration in H-ionisation zone

Chapter 5

Future Work

5.1 Interpolation and Derivatives of Viscous Fluxes

Derivatives are used within ANTARES for the computation of the viscous matrix and the diffusion approximation. Instead of taking the derivatives at the cell centre as in Section 3.6, compute the viscous matrix there and interpolate then to the boundary grid, derivatives can now also be taken at the cell boundary via the function $\frac{\partial_{bound}(u)}{\partial x}$ at least for the equidistant grid. This is done in a way that makes the various derivatives within the code consistent. The coefficients of this function are determined by the relation

$$\Delta_{centre} u = \frac{\partial_{update}}{\partial x}\left(\frac{\partial_{bound}(u)}{\partial x}\right)$$

where Δ_{centre} is the 2nd derivative taken at the cell centre, $\frac{\partial_{bound}(u)}{\partial x}$ gives the derivative on the boundary grid for values u located at the cell centre and $\frac{\partial_{update}(v)}{\partial x}$ the derivative on the centre grid for values v located at the cell boundary.

Thus the 4th order symmetric stencils for an equidistant grid are

$$\frac{1}{r_{i+1}-r_i}\left[\frac{1}{12}u_{i-2}-\frac{15}{12}u_{i-1}+\frac{15}{12}u_i-\frac{1}{12}u_{i+1}\right]$$

and for a stretched grid:

$$\frac{1}{r_{i+1}-r_i}\quad\left[2q^{5.5}\left(-q^2+2\right)u_{i-2}\qquad -2q^{2.5}\left(-q^5+4q^3+5q^2+5q+2\right)u_{i-1}\right.$$
$$2q^{0.5}\left(2q^5+5q^4+5q^3+4q^2-1\right)u_i\qquad \left.-2q^{0.5}\left(2q^2-1\right)u_{i+1}\right]/$$
$$\left[(1+q)^2\left(1+q+2q^2+q^3+q^4\right)\right]$$

At the upper and lower physical boundary the asymmetric stencils are used.

For the polar and moving grid the problem is by far more complicated, for in this derivation the primitive function has been used just as in the derivation of the original ENO coefficients (see section 3.8.1). Without using the primitive function we arrive at the stencil

$$\frac{1}{r_{i+1}-r_i}\quad\left[\frac{q^{3.5}\left(-q^{1.5}+2\right)}{\left(1+q^{0.5}\right)^2\left(1+2q+2q^2+q^3\right)}u_{i-2}\qquad -\frac{q^{0.5}\left(-q^{0.5}+2\right)\left(1+q^{0.5}+q\right)^2}{\left(1+q^{0.5}\right)^2(1+q)}u_{i-1}\right.$$
$$\frac{\left(-1+2q^{0.5}\right)\left(1+q^{0.5}+q\right)^2}{\left(1+q^{0.5}\right)^2 q(1+q)}u_i\qquad \left.\frac{1-2q^{1.5}}{\left(1+q^{0.5}\right)^2 q\left(1+2q+2q^2+q^3\right)}u_{i+1}\right]$$

for the stretched grid. This reduces to

$$\frac{1}{r_{i+1} - r_i} \left[\frac{1}{24} u_{i-2} - \frac{23}{24} u_{i-1} + \frac{23}{24} u_i - \frac{1}{24} u_{i+1} \right]$$

on an equidistant grid.

However this stencil leads to a loss of order during the update at least for the equidistant, not moving grid. Should then accuracy be insufficient we have to consider a stencil of higher order or using the actual cell volumina.

5.2   Time Integration

To save computation time, we consider implicit time integration methods applicable to an entire coupled set of partial differential equations. Optimal methods have been found for this class of problems.

Very successful Runge-Kutta methods, which are cheap to implement, are singly diagonally implicit Runge-Kutta methods (SDIRK) (see [KKLMZ 2010][1]). It can be shown that for SDIRK methods $R = c$ holds, where R is the radius of contractivity and c is the CFL-number. For order $p = 2$ the method with $s = 1, 2, 3$ steps has been proven to be optimal. For $s > 3$ the methods are conjectured to be optimal in the class of SDIRK methods based on numerical optimisation.

Practical aspects of TVD integrators are discussed by L. Ferracina and M. Spijker [2]. The computational advantages of using TVD methods are demonstrated by means of an example, the efficiency of the numerical methods is assessed, where the ratio of step-size coefficient and number of stages per interval of the corresponding length serves as the indicator. It is found that SDIRK with $p = 2$ is optimal in that respect, while this quantity decreases with the order of the method. However a larger number of stages generally leads to more efficient methods. The values are considerably higher than for explicit methods, but of course this will be compensated for to some extent by the cost of the solution of the non-linear algebraic equations.

For the equidistant grid and the initial value problem $y'(t) = F(y(t))$ a general implicit s-stage Runge-Kutta method

$$\begin{aligned} y_i &= y_{old} + \Delta t \sum_{j=1}^{s} a_{i,j} F(y_j) \qquad i = 1, \ldots, s \\ y_{new} &= y_{old} + \Delta t \sum_{j=1}^{s} b_j F(y_j) \end{aligned}$$

---

[1] in addition to more detailed information about the implementation in the ANTARES Code extensive references can also be found in this report

[2] An extension and analysis of the Shu-Osher representation of Runge-Kutta methods. Math. Comp., 74, pp. 201-219, 2004

with for $p = 2$:

$$
\begin{aligned}
a_{ij} &=
\begin{cases}
\frac{1}{2s}, & i = j, 1 \le i \le s \\
\frac{1}{s}, & 1 \le j < i \le s \\
0, & otherwise
\end{cases} \\
b_j &= \frac{1}{s}, \qquad j = 1, \dots, s
\end{aligned}
$$

has already been implemented in ANTARES for $p = 2$ and $p = 3$. Up to now they can only achieve better accuracy, but not higher efficiency regarding computing time. The computation of radiative transfer and diffusion approximation requires an additional Poisson equation. The adjustments for the moving, polar grid must also still be done. It remains to be seen if the stability increases and if at the same time the cost for additional stages and iterations is compensated for by larger time steps.

5.3 Grid Refinement and Three Dimensional Simulations

As demonstrated in 3.7.3 the resolution used in Section 4.4 is still not sufficient. A better resolved model with an aperture angle of only 1°, 800 points in radial direction and 300 grid points in angular direction on the coarse grid and a grid refinement factor of 5 in both directions has been started. The resulting resolution on the fine grid is from $0.16Mm$ to $0.20Mm$ in radial direction. In the critical region it is $0.18Mm$ in radial direction and $0.32Mm$ in angular direction, leading to an aspect ratio of $1 : 1.78$. When comparing this to figure 3.7.5 on page 53 we get approximately $\frac{1.5}{0.18} \approx 8$ grid points to resolve the peak in q_{rad}.
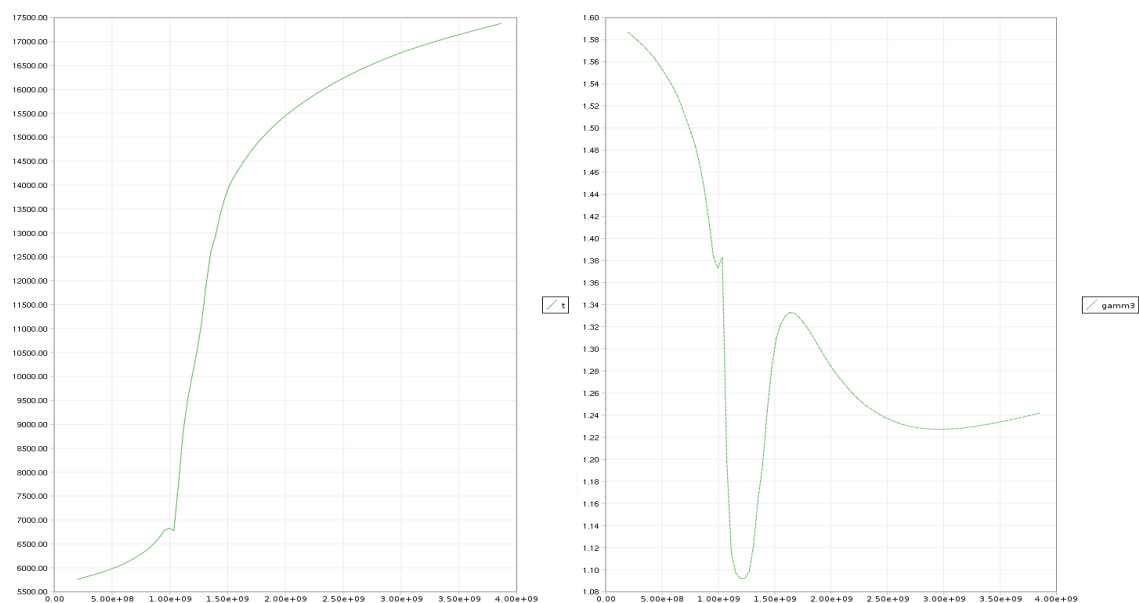
Figure 5.3.1:   temperature and Γ_3 in the grid refinement zone

When convection is fairly established in the hydrogen ionisation zone, it can be enlarged by setting copies side by side. For a proper representation of the He II-ionisation zone the aperture angle needs to be fairly large, in the simulation presented in section 4.2 we used 10°. In order to break up the highly periodic pattern an additional slight perturbation will then be added.

This model will also be used as a starting point for a three dimensional simulation. The conversion from 2D to 3D is similar to the conversion from one to two dimensions (see section 3.1).

Chapter 6

Appendices

6.1 Appendix A

Derivatives and the Navier-Stokes Equations in Spherical Polar Coordinates

The spherical polar coordinates are (r, θ, φ), where φ is the azimuthal angle.[1] A vector can be written as

$$\vec{u} = u_r \vec{e}_r + u_\theta \vec{e}_\theta + u_\varphi \vec{e}_\varphi$$

where the unit vector is related to the Cartesian Coordinates by the matrix

$$\begin{pmatrix} \sin\theta\cos\varphi & \sin\theta\sin\varphi & \cos\theta \\ \cos\theta\cos\varphi & \cos\theta\sin\varphi & -\sin\theta \\ -\sin\varphi & \cos\varphi & 0 \end{pmatrix}$$

Derivatives

Gradient of a scalar a

$$\nabla a = \frac{\partial a}{\partial r} \vec{e}_r + \frac{1}{r}\frac{\partial a}{\partial \varphi} \vec{e}_\varphi + + \frac{1}{r}\frac{\partial a}{\partial \varphi} \vec{e}_\varphi$$

Divergence of a vector $\vec{u}$

$$\nabla \cdot \vec{u} = \frac{1}{r^2}\frac{\partial \left(r^2 u_r \right)}{\partial r} + \frac{1}{r\sin\theta}\frac{\partial \left(\sin\theta u_\theta \right)}{\partial \theta} + \frac{1}{r\sin\theta}\frac{\partial u_\varphi}{\partial \varphi}$$

Laplacian of a scalar

$$\nabla^2 a = \frac{1}{r^2}\frac{\partial \left(r^2 \frac{\partial a}{\partial r} \right)}{\partial r} + \frac{1}{r^2\sin\theta}\frac{\partial \left(\sin\theta \frac{\partial a}{\partial \theta} \right)}{\partial \theta} + \frac{1}{r^2\sin^2\theta}\frac{\partial^2 a}{\partial \varphi^2}$$

Advective derivative of a scalar a

$$\left(\vec{u} \cdot \nabla \right) a = u_r \frac{\partial a}{\partial r} + \frac{u_\theta}{r}\frac{\partial a}{\partial \theta} + \frac{u_\varphi}{r\sin\theta}\frac{\partial a}{\partial \varphi}$$

---

[1]To obtain the 2D formulae set $\theta = \pi/2$

99

Curl of a vector

$$\nabla \times \vec{u} = \frac{1}{r \sin \theta} \left(\frac{\partial \left(\sin \theta u_\varphi \right)}{\partial \theta} - \frac{u_\theta}{\partial \varphi} \right) \vec{e}_r + \frac{1}{r} \left(\frac{1}{\sin \theta} \frac{\partial u_r}{\partial \varphi} - \frac{\partial \left(r u_\varphi \right)}{\partial r} \right) \vec{e}_\theta + \frac{1}{r} \left(\frac{\partial \left(r u_\theta \right)}{\partial r} - \frac{\partial u_r}{\partial \theta} \right) \vec{e}_\varphi$$

Compressible Navier Stokes Equations without body force

$$\partial_t u_r = -\left[\partial_r \left(u_r^2 + \frac{p}{\rho} \right) + \frac{1}{r} \partial_\theta \left(u_r u_\theta \right) + \frac{1}{r \sin \theta} \partial_\varphi \left(u_r u_\varphi \right) \right. \tag{6.1.1}$$
$$\left. + \frac{1}{r} \left(2u_r^2 - u_\theta^2 - u_\varphi^2 + u_r u_\theta \cot \theta \right) \right]$$

$$\partial_t u_\theta = -\left[\partial_r \left(u_r u_\theta \right) + \frac{1}{r} \partial_\theta \left(u_\theta^2 + \frac{p}{\rho} \right) + \frac{1}{r \sin \theta} \partial_\varphi \left(u_\theta u_\varphi \right) \right. \tag{6.1.2}$$
$$\left. + \frac{1}{r} \left(3u_r u_\theta + u_\theta^2 \cot \theta - u_\varphi^2 \cot \theta \right) \right]$$

$$\partial_t u_\varphi = -\left[\partial_r \left(u_r u_\theta \right) + \frac{1}{r} \partial_\theta \left(u_\theta u_\varphi \right) + \frac{1}{r \sin \theta} \partial_\varphi \left(u_\varphi^2 + \frac{p}{\rho} \right) \right. \tag{6.1.3}$$
$$\left. + \frac{1}{r} \left(3u_r u_\theta + 2u_\theta u_\varphi \cot \theta \right) \right]$$

$$\partial_t e = -\left[\partial_r \left(u_r \left(e + p \right) \right) + \frac{1}{r} \partial_\theta \left(u_\theta \left(e + p \right) \right) + \frac{1}{r \sin \theta} \partial_\varphi \left(u_\varphi \left(e + p \right) \right) \right. \tag{6.1.4}$$
$$\left. + \frac{1}{r} \left(2u_r \left(e + p \right) + u_\theta \left(e + p \right) \cot \theta \right) \right]$$

Incompressible Navier Stokes Equations with grid velocity but without body force and viscosities

$$\partial_t \rho = -\left[\partial_r \left(I_r - \rho u_g \right) + \frac{1}{r} \partial_\theta \left(I_\theta \right) + \frac{1}{r \sin \theta} \partial_\varphi \left(I_\varphi \right) \right. \tag{6.1.5}$$
$$\left. + \frac{1}{r} \left(2 \left(I_r - \rho u_g \right) + I_\theta \cot \theta \right) \right]$$

$$\partial_t I_r = -\left[\partial_r \left(\frac{I_r^2}{\rho} - I_r u_g + p \right) + \frac{1}{r} \partial_\theta \left(\frac{I_r I_\theta}{\rho} \right) + \frac{1}{r \sin \theta} \partial_\varphi \left(\frac{I_r I_\varphi}{\rho} \right) \right. \tag{6.1.6}$$
$$\left. + \frac{1}{r} \left(2\frac{I_r^2}{\rho} - 2I_r u_g - \frac{I_\theta^2}{\rho} - \frac{I_\varphi^2}{\rho} + \frac{I_r I_\theta}{\rho} \cot \theta \right) \right]$$

$$\partial_t I_\theta = -\left[\partial_r \left(\frac{I_r I_\theta}{\rho} - I_\theta u_g \right) + \frac{1}{r} \partial_\theta \left(\frac{I_\theta^2}{\rho} + p \right) + \frac{1}{r \sin \theta} \partial_\varphi \left(\frac{I_\theta I_\varphi}{\rho} \right) \right. \tag{6.1.7}$$
$$\left. + \frac{1}{r} \left(3\frac{I_r I_\theta}{\rho} - 2I_\theta u_g + \frac{I_\theta^2}{\rho} \cot \theta - \frac{I_\varphi^2}{\rho} \cot \theta \right) \right]$$

$$\partial_t I_\varphi = -\left[\partial_r \left(\frac{I_r I_\varphi}{\rho} I_\varphi u_g \right) + \frac{1}{r} \partial_\theta \left(\frac{I_\theta I_\varphi}{\rho} \right) + \frac{1}{r \sin \theta} \partial_\varphi \left(\frac{I_\varphi^2}{\rho} + p \right) \right. \tag{6.1.8}$$
$$\left. + \frac{1}{r} \left(3 \frac{I_r I_\varphi}{\rho} - 2 I_\varphi u_g + 2 \frac{I_\theta I_\varphi}{\rho} \cot \theta \right) \right]$$

$$\partial_t e = -\left[\partial_r \left(\frac{I_r}{\rho} (e+p) - e u_g \right) + \frac{1}{r} \partial_\theta \left(\frac{I_\theta}{\rho} (e+p) \right) + \frac{1}{r \sin \theta} \partial_\varphi \left(\frac{I_\varphi}{\rho} (e+p) \right) \right. \tag{6.1.9}$$
$$\left. + \frac{1}{r} \left(2 \frac{I_r}{\rho} (e+p) - 2 e u_g + \frac{I_\theta}{\rho} (e+p) \cot \theta \right) \right]$$

Danksagung

Nomenclature

L luminosity

ε internal energy

κ termal conductivity

Π_d period length in days

$\odot$ of the sun

$\vec{r} = (r, \varphi)^T$ position of a definite point

e total energy density, the sum of internal and kinetic energy (without potential energy)

$\vec{g}$ gravity

$\vec{I}$ momentum density

p pressure

Q_{rad} radiative heating term

ρ density

$\overline{\sigma}$ viscous stress tensor

t time

$\vec{u} = (u_r, u_\varphi)^T$ fluid velocity

$\vec{u_g}$ grid velocity

c_p specific heat at constant pressure

d_{fac} dilation factor of the grid from time n to n+1

$\rho\varepsilon$ specific internal energy

Γ_i adiabatic exponents

I_ν Intensity at frequency ν

$I_\nu\left(r\right)$ specific intensity in direction r at frequency ν

J_ν mean Intensity at frequency ν

T Temperature

List of Figures

List of Tables

Bibliography

[AF 1994]   Alexander, D.R., and Ferguson, J.W., *Low-temperature Rosseland opacities*, The Astrophysical Journal 437, pp. 879-891, 1994

[BK 1962]   Baker N., Kippenhahn R., *The Pulsations of Model of δ Cephei Stars*, Zeitschrift für Astrophysik 54, pp. 114-151, 1961

[BV 1958]   Böhm-Vitense, E., *Über die Wasserstoffkonvektionszone in Sternen verschiedener Effektivtemperaturen und Leuchtkräfte*, Zeitschrift für Astrophysik 46, pp. 108-143, 1958

[BMS 1995] Bona, C., Masso, J., and Stela, J., *Numerical Black Holes: A Moving Grid Approach*, Physical Review D 51, pp. 1639–1645, 1995

[BMS 1999] Bono, G., Marconi, M., and Stellingwerf, R.F., *Classical Cepheid Pulsation Models. I. Physical Structure*, The Astrophysical Journal Supplement Series 122, pp. 167-205, 1999

[BS 1994]   Bono, G., and Stellingwerf, R.F., *Pulsation and stability of RR Lyrae stars. 1: Instability Strip*, ApJS 93, pp. 223-269, 1994

[BVS 1999] Bruls, J.H.M.J., Vollmöller, P. and Schüssler, M., *Computing radiative heating on unstructured spatial grids*, Astronomy and Astrophysics 348 , pp. 233–248, 1999

[BKM 1997] Buchler, R.L., Kollath, Z. and Marom, A., *An adaptive Code for radial stellar model pulsations*, Astrophysics and Space Science, Volume 253, Issue 1, pp. 139-160, 1997

[Buc 2009] Buchler, R.J., *The State of Cepheid Pulsation Theory*, AIP Conference Proceedings, American Institute of Physics Conference Series, vol. 1170, pp. 51–58, 2009, arXiv:0907.1766.

[Car 1963] Carlson, B.G., *The numerical theory of neutron transport*, in Alder, B., Fernbach, S. (eds.), Methods in Computational Physics, pp. 1–42, 1963

[Chr 1964] Christy, R.F., *The Calculation of Stellar Pulsation,* Rev. Mod. Phys. 36, pp. 555–571, 1964

[Chr 1966a] Christy, R.F., *A Study of Pulsation in RR Lyrae Models*, Astrophysical Journal, vol. 144, p. 108, 1966

[Chr 1966b] Christy, R.F., *Pulsation Theory*, Annual Review of Astronomy and Astrophysics, vol. 4, pp. 353-392, 1966

[CM 1990] Chorin A., Marsden J.E., *Mathematical introduction to fluid mechanics*, Springer-Verlag, 1990

[Cox 1980] Cox, J.P., *Theory of Stellar Pulsation*, Princeton University Press, 1980

[Cox 1963] Cox, J.P., *On Second Helium Ionization as a Cause of Pulsational Instability in Stars*, Astrophys. J. 138, p. 487, 1963

[CBE 1966] Cox, A.N., Brownlee, R.R. and Eilers, D.D., *Time-dependent Method for Computation of Radiation Diffusion and Hydrodynamics*, Astrophysical Journal, vol. 144, p. 1024, 1966

[CCOKE 1966] Cox, J.P., Cox, A.N., Olsen K.H., King, D.S., Eilers, D.D., *Self-excited Radial Oscillations in Thin Stellar Envelopes I.* Astrophysical Journal, vol. 144, p. 1038, 1966

[DM 1996] Donat, R., and Marquina, A., *Capturing shock reflactions: An improved flux formula,* Journal of Computational Physics 25, pp. 42-58, 1996

[Edd 1917] Eddington, A. S., *The pulsation theory of Cepheid variables*, The Observatory 40, pp. 290–293, 1917

[FMDO 1998] Fedkiw, R.P., Merriman, B., Donat, R., and Osher, S., *The Penultimate Scheme for Systems of Conservation Laws: Finite Difference ENO with Marquina's Flux Splitting*, Progress in Numerical Solutions of Partial Difference Equations, Arachon, France (M. Hafez, ed.), July 1998

[FBK 2000] Feuchtinger, M.U., Buchler, J.R. and Kolláth, Z., *Hydrodynamical survey of first-overtone Cepheids.*, ApJ 544, pp. 1056-1066, 2000, arXiv:astro-ph/0005230

[HEOC 1987] Harten, A., Enquist, B., Osher, S. and Chakravarthy, S.R., *Uniformly high order accurate essentially non-oscillatory schemes, iii.* Journal of Computational Physics 71, pp. 231-303, 1987

[HKT 1994] Hansen, C.J., Kawaler, S.D. and Trimble, V., *Stellar Interiors. Physical Principles, Structure and Evolution*, Springer, 1994

[HTM 1984] Hurlburt, N.E., Toomre, J. and Massaguer, J.M., *Two-dimensional compressible convection extending over multiple scale heights*, The Astrophysical Journal 282, pp. 557-573, 1984

[JS 1996]   Jiang, G.S. and Shu, C.-W. *Efficient implementation of weighted ENO schemes*, Journal of Computational Physics 126, pp. 202-228, 1996

[KW 1990] Kippenhahn, R., Weigert, A., *Stellar Structure and Evolution*, Springer-Verlag, 1990

[KKLMZ 2010] Koch, O., Kupka, F., Löw-Baselli, B., Mayrhofer, A., Zaussinger, F., *SDIRK Methods for the ANTARES Code*, ASC Report 32/2010, Vienna University of Technology, Wien, 2010

[KA 1988]   Kunasz, G.L. and Auer, L.H. *Short characteristic integration of radiative transfer problems: Formal solution in two-dimensional slabs*, Journal of Quantitative Spectroscopy and Radiative Transfer 39, pp. 67–79, 1988

[Lea 1912] Leavitt, H.S., *Periods of 25 variable stars in the small magellanic cloud*, Harvard College Observatory, Circular 173, 1912

[LOC 1994] Liu, X., Osher, S., Chan, T., *Weighted essentially non-oscillatory schemes*, Journal of Computational Physics 115, pp. 200-212, 1994

[LD 1982]   de Loore, C.W.N., Doom, C., *Structure and evolution of single and binary stars*, Springer 1982

[Mih 1978] Mihalas, D., *Stellar Atmospheres*, second ed., W.H. Fremann and Company, 1978

[MM 1984] Mihalas, D. and Weibel Mihalas, B., *Foundations of radiation hydrodynamics*, New York, Oxford University Press, 1984

[MWN 1984] Mihalas, D., Winkler K.-H.A. and Norman, M.L., *Adaptive-mesh radiation hydrodynamics II. The radiation and fluid equations in relativistic flows*, J. Quant. Spectrosc. Radiat. Transfer vol. 31, No 6, pp. 479-489, 1984

[Mut et al 2007] Muthsam, H.J., Löw-Baselli, B., Obertscheider C., Langer, M., Lenz, P., Kupka, F., *High-resolution models of solar granulation: the two-dimensional case,* Mon. Not. R. Astron. Soc. 380, pp. 1335–1340, 2007

[Mut et al 2010b] Muthsam, H.J., Kupka, F., Mundprecht, E., Zaussinger, F., Grimm-Strele, H., Happenhofer, N., *Simulations of stellar convection, pulsation and semiconvection*, Proceedings IAU Symposium No. 271, 2010

[Mut et al 2010a] Muthsam, H.J., Kupka, F., Löw-Baselli, B., Obertscheider C., Langer, M., Lenz, P., *ANTARES – A Numerical Tool for Astrophysical RESearch with applications to solar granulation,* New Astronomy 15, pp. 460–475, 2010

[NS 1999]   Nordlund, A., Stein, R.F., *3-D Convection Models are they Compatible with 1-D Models?*, IAU Colloquium 176, Conference Series, 1999

[Obe 2007] Obertscheider, C., *Modelling of solar granulation - Implementation and comparison of numerical schemes*, Thesis University of Vienna, Faculty of Mathematics, 2007

[Pet 2002] Petterson, O.K.L., *A spectroscopic and dynamical study of binary and other Cepheids*, Thesis, University of Canterbury, New Zealand, 2002

[RSI 1996] Rogers, F.J., Swenson, F.J. and Iglesias, C.A., *OPAL Equation-of-State Tables for Astrophysical Applications*, The Astrophysical Journal 456, pp. 902-908, 1996

[Schw 1900] Schwarzschild, K., *Beiträge zur photographischen Photometrie der Gestirne*, Publ. d. v. Kuffner'schen Sternw. Wien V, C3-C135, 1900

[SO 1988] Shu, C.-W., Osher, S., *Efficient Implementation of Essentially Non-oscillatory Shock-Capturing Schemes*, Journal of Computational Physics 77, pp. 439-371, 1988

[Shu 1997] Shu, C.-W., *Essentially non-oszillatory and weighted essentially non-oszillatory schemes for hyperbolic conservation laws,* Technical report NASA CR-97-206253 ICASE Report No. 97-65, Institute for Computer Applications in Science and Engineering, 1997

[Spi 1957] Spiegel, E.A., *The Smoothing of Temperature Fluctuations by Radiative Transfer*, ApJ 126, 1957

[SN 1998] Stein, R.F., Nordlund, A., *Simulations of Solar Granulation. I. General Properties*, The Astrophysical Journal 499, pp. 914-133, 1998

[Ste 1974] Stellingwerf, R.F., *The calculation of periodic pulsations of stellar models*, The Astrophysical Journal 192, pp. 139-144, 1974

[Ste 1975] Stellingwerf, R.F., *Modal stability of lyrae stars*, The Astrophysical Journal 195, pp. 441-446, 1975

[Ste 1982a] Stellingwerf, R.F., *Convection in Pulsating Stars - Part Two - Rr-Lyrae Convection and Stability*, ApJ 262, pp. 339–343, 1982a

[Ste 1082b] Stellingwerf, R.F., *Convection in pulsating stars. I - Nonlinear hydrodynamics. II - RR Lyrae convection and stability*, ApJ 262, pp. 330–338, 1982b

[Ste 1984] Stellingwerf, R.F., *Convection in pulsation stars IV. Nonlinear effects*, ApJ 277, pp. 327-332, 1984

[Sti 2002] Stix, M., *The Sun*, Springer Verlag, Second Edition 2002

[Vit 1953] Vitense, E., *Die Wasserstoffkonvektionszone der Sonne*, Zeitschrift für Astrophysik 32, pp. 135–164, 1953

[Vög 2003] Vögler, A., *Three-dimensional simulations of magneto-convection in the solar photosphere*, PhD thesis, Universität Göttingen, 2003

[WNM 1984] Winkler, K.-H.A., Norman, M.L. and Mihalas, D., *Adaptive-mesh radiation hydrodynamics I. The radiative transport equation in a completely adaptive coordinate system*, J. Quant. Spectrosc. Radiat. Transfer vol. 31, No. 6, pp. 473-478, 1984

[YKB 1998] Yecko, P.A., Kolláth, Z. and Buchler, J.R., *Turbulent convective Cepheid models: Linear Properties*, A&A 336, pp. 553-564, 1998, arXiv:astro-ph/9804124.

[Zhe 1963] Zhevakin, S.A., *Physical Basis of the Pulsation Theory of Variable Stars*, ARA&A 1, pp. 367–400, 1963

Erklärung: „Ich habe mich bemüht, sämtliche Inhaber der Bildrechte ausfindig zu machen und ihre Zustimmung zur Verwendung der Bilder in dieser Arbeit eingeholt. Sollte dennoch eine Urheberrechtsverletzung bekannt werden, ersuche ich um Meldung bei mir."

Curriculum Vitae

Name	Eva Mundprecht
Geboren	4. April 1965 Eggenburg/Niederösterreich
Nationalität	Österreich

September 1971-Juni 1975	Volksschule Eggenburg
September 1975-Juni 1977	BG u. BRG für Mädchen Billrothstraße, Wien XIX
September 1977-Juni 1983	BRG Schottenbastei, Wien I
Oktober 1983-Juni 1984	Studium an der TU Wien
Oktober 1984-Juni 1987	Mathematik Studium an der Universität Wien
Oktober 1987-Juni 1991	Studium an der Veterinärmedizinischen UniversitätWien
Oktober 1993-November 2000	Mathematik Studium an der Universität Wien
16. November 2000	2. Diplomprüfung mit Auszeichnung bestanden
September 2001-Juni 2007	Unterrichtstätigkeit an der Rudolf Steiner - Schule Pötzleinsdorf
seit Oktober 2005	Doktoratsstudium der Mathemaik
Oktober 2007 - Juni 2008	Lehrauftrag an der Fachhochschule St. Pölten
seit Oktober 2007	beschäftigt an der Universität Wien im Rahmen der FWF Projekte: P18224 *Dynamische Sternatmosphären: Konvektion und Pulsation*, P20762 *Dynamik solarer und stellarer Granulation*, P20973 *Numerische Modellierung der Semikonvektion (Stellarphysik)*

27. April 1990	Hochzeit mit Robert Herzner
2. November 1991	Geburt unseres Sohnes Alarich Herzner
4. April 1995	Geburt unserer Tochter Isabella Herzner